Volume 17, Issue 4 2010

JOURNAL OF FLOW VISUALIZATION AND IMAGE PROCESSING

begell house, inc.
publishers

AIMS AND SCOPE

The *Journal of Flow Visualization and Image Processing* is a quarterly refereed journal that publishes original papers to disseminate and exchange the knowledge and information obtained through research on the principles and applications of flow visualization techniques, including flow image processing. Its purpose is to promote academic and industrial advancement and improvement of the techniques internationally. This journal presents a wealth of practical information covering all areas in science, technology, and medicine for engineers, scientists, and researchers in industry, academia, and government.

JOURNAL OF FLOW VISUALIZATION & IMAGE PROCESSING
VOLUME 17 / ISSUE 4 2010

Journal of Flow Visualization & Image Processing 17(4), 281–296 (2010)

VISUALIZATION AND CHARACTERIZATION OF A LATERAL SWIRL FLOW STRUCTURE IN SINUSOIDAL CORRUGATED-PLATE CHANNELS

S. Vyas,[1] R. M. Manglik,[2] & M. A. Jog[2]*

[1]*Gas Turbine Accessories Engineering, GE Energy, Greenville, SC 29615, USA*

[2]*Thermal-Fluids & Thermal Processing Laboratory, University of Cincinnati, Cincinnati, OH 45221-0072, USA*

[*]Address all correspondence to R. M. Manglik E-mail: raj.manglik@uc.edu

Curved surfaces interacting with fluid flow tend to produce swirl or secondary circulation, and such mechanisms in wavy-plate-fin channels have been investigated. The fluid recirculation or vortex structure in low Reynolds number flows in plate channels with sinusoidal corrugations is characterized by experimental flow visualization and Laser Doppler Velocimetry (LDV) measurements. The parametric effects of the wavy-plate geometry, described by its waviness aspect ratio γ *(= 2 × amplitude/wavelength) and inter-plate spacing ratio* ε *(= spacing/2 × amplitude), are delineated. Wall-curvature-induced swirl is produced by fluid separation downstream of the wavy-surface peak, its reattachment upstream of the subsequent peak, and the consequent encapsulation of lateral recirculating cells in the channel-wall concavities. The characteristic signature of these trough-region vortices is significantly altered with increasing flow rate, inter-plate spacing* ε*, and severity of wall waviness* γ*, when the swirl tends to grow spatially and envelop much of the core-flow region.*

KEY WORDS: *wavy-plate fin, flow visualization, velocity imaging, swirl flow, lateral vortex*

1. INTRODUCTION

Extended or finned surfaces are widely used in compact heat exchangers to enhance heat transfer as well as to reduce their size and volume, as they provide substantially higher surface-area-to-volume ratios (Kays and London, 1984; Manglik, 2003; Shah and Sekulic, 2003). This feature is further augmented by employing geometrically modified fins, which not only increase the surface-area density of the exchanger but also improve the convective heat transfer coefficient by significantly altering the convective flow field. Some examples of such enhanced surfaces include offset-strip fins, louvered fins, perorated fins, and corrugated or wavy

1065-3090/10/$35.00

NOMENCLATURE

A	amplitude of sinusoidal waviness of plate-fin wall, Fig. 1c, mm	u_m	mean or average axial velocity, m/s
d_h	hydraulic diameter ($\approx 2S$), mm	x, y	axial and lateral Cartesian coordinates, respectively, m
H	plate-fin height, Fig. 1c, mm	**Greek symbols**	
L	wavelength of sinusoidal plate-fin corrugation, Fig. 1c, mm	α	wavy-fin channel flow cross-section aspect ratio ($=S/H$) [–]
Pr	Prandtl number ($\mu c_p/k$) [–]		
Re	hydraulic diameter-based Reynolds number ($= \rho u_m d_h/\mu$) [–]	ε	inter-fin spacing to wavy-plate amplitude ratio ($=S/2A$) [-]
S	fin-plate spacing, Fig. 1c, mm	γ	wavy-fin wall corrugation aspect ratio ($=2A/L$) [-]
u, v	axial and lateral velocity components, respectively, m/s		

fins (Kays and London, 1984; Manglik and Bergles, 1995; Wang, 2000; Manglik, 2003; Shah and Sekulic, 2003; Zhang and Tafti, 2003; Metwally and Manglik, 2004; Zhang et al., 2004; Webb and Kim, 2005). Of these, wavy fins are particularly attractive for numerous heat-exchange applications because of their simplicity of manufacture, potential for enhanced thermal-hydraulic performance, and ease of usage in both plate-fin and tube-fin type exchangers. Enhanced fin geometries continue to attract considerable research attention (Comini et al., 2003; Zhang and Tafti, 2003; Manglik and Bergles, 2004; Ngo et al., 2006), and more so with growing present-day concerns for energy conservation, efficiency of conversion, and the consequent environmental impact.

A typical sinusoidal wavy-plate-fin core and its usage in a compact heat exchanger are illustrated in Figs. 1a and 1b, and the primary geometrical attributes of the inter-fin flow channel are schematically depicted in Fig. 1c. The corrugated-plate channel is essentially described by the fin height H, inter-fin spacing S, amplitude of waviness A, and wavelength or pitch of waviness L. The dimensionless representations of these variables can be expressed in terms of a flow-cross-section aspect ratio ($\alpha = S/H$), inter-fin-spacing ratio ($\varepsilon = S/2A$), and plate/fin-wall corrugation or waviness aspect ratio ($\gamma = 2A/L$). For a given fin height and waviness, α and ε also represent the fin density, as both α and ε decrease with increasing fin density (or reduced inter-fin spacing S) but fixed A and H; the waviness aspect ratio γ represents the severity of wall corrugation.

Perhaps the oldest and most frequently referenced repository of experimental data on enhanced fin cores is the classical monograph by Kays and London (1984). The listings therein are somewhat dated and limited in scope, as it only gives f and j

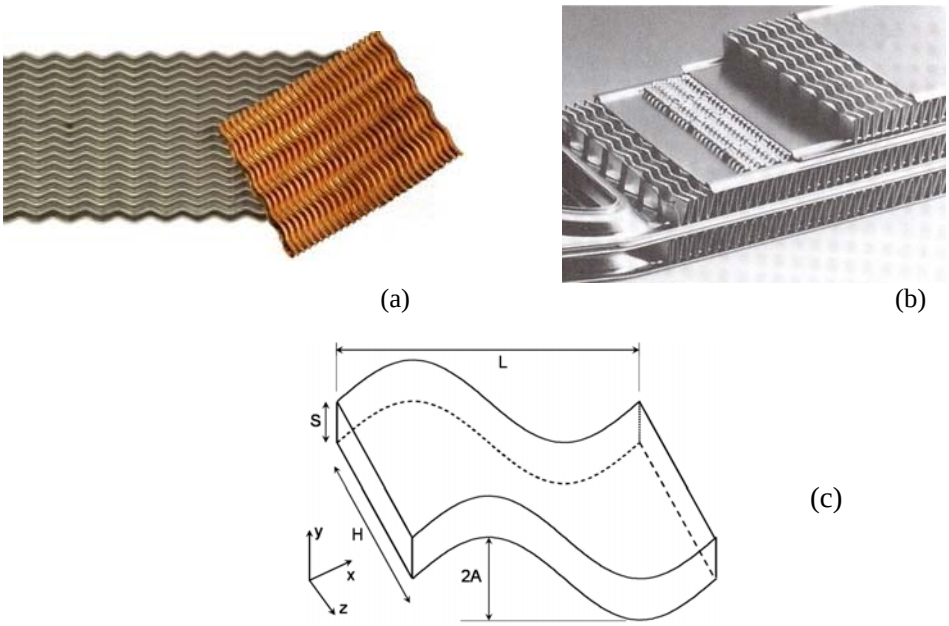

FIG. 1: Compact heat-exchange cores with corrugated-plate fins: (a) fins with sinusoidal wall corrugations, (b) typical compact heat exchanger with wavy-plate fins, and (c) geometrical description of sinusoidal wavy-plate-fin channel

data, with no exposition of the concomitant flow structure. This is particularly limiting in the case of corrugated or wavy fins, where data for only three wavy-plate-fin geometries are given ($0.136 \le \alpha \le 0.232$, $0.725 \le \varepsilon \le 1.128$, and $\gamma = 0.208$). Many early attempts at characterizing the convective heat and mass transfer enhancement behavior were restricted to turbulent flows (Beloborodov and Volgin, 1971; Goldstein and Sparrow, 1977; Vajravelu, 1980; O'Brien and Sparrow, 1982; Sparrow and Comb, 1983; Sparrow and Hossfeld, 1984; Amano 1985). Sparrow and co-workers (Goldstein and Sparrow, 1977; O'Brien and Sparrow, 1982; Sparrow and Comb, 1983; Sparrow and Hossfeld, 1984) considered plate channels with sharp triangular corrugations, and evaluated mass transfer enhancement using naphthalene sublimation techniques. Gradeck and Lebouché (1998) have measured wall shear stress by an electrochemical method, which has also been applied to non-Newtonian flows (Béreiziat et al., 1995). In some studies, the onset of flow unsteadiness and determining Re_{cr} for laminar-turbulent transition has been addressed (Nishimura et al., 1987, 1990; Gschwind et al., 1995; Rush et al., 1999; Selvarajan et al., 1999; Zimmerer et al., 2002). It has been suggested by some investigators (Nishimura et al., 1990; Rush et al., 1999) that wall waviness may initiate turbulent instabilities at lower flow rates as $Re \rightarrow 1000$, but many other studies (Stasiek et al., 1996; Sawyers et al., 1998; Muley et al., 1999; Selvarajan et al., 1999;

Zimmerer et al., 2002; Metwally and Manglik, 2004; Hwang et al., 2006) have indicated a steady flow field with recirculation zones near the wall furrows and a smooth laminar-turbulent transition that does not display the characteristic sharp change in friction losses or heat transfer coefficients.

Much of the laminar or low Reynolds number flow (Re < 2000) work has been theoretical (Asako and Faghri, 1987; Motamed Ektesabi et al., 1987; Asako et al., 1988; Garg and Maji, 1988; Yang et al., 1997; Comini et al., 2003; Metwally and Manglik, 2004; Zhang et al., 2004; Manglik et al., 2005; Castellões et al., 2010). Computational simulations of flow and heat transfer in channels with sinusoidal wall waviness (Asako and Faghri, 1987; Motamed Ektesabi et al., 1987; Garg and Maji, 1988; Metwally and Manglik, 2004; Zhang et al., 2004; Manglik et al., 2005) as well as sharp and rounded-edged triangular profiles (Asako and Faghri, 1987; Asako et al., 1988; Yang et al., 1997; Comini et al., 2003) have been carried out. It has generally been observed that wall corrugations induce steady recirculation or lateral vortices in the concavities of the corrugated-plate channel in low Reynolds number flows. There is a consequent disruption and thinning of the boundary layer, and the combined effects significantly enhance the convective heat and mass transfer. The majority of computational models have considered a two-dimensional flow geometry that is valid only when $H >> S$ or $\alpha \rightarrow 0$. In a previous three-dimensional analysis (Manglik et al., 2005), steady and spatially periodic growth and disruption of pairs of symmetric helical swirl in the wall-trough regions of the flow cross section has been suggested. All these simulated numerical solutions, however, lack extended experimental verification, and this is addressed in the present study.

In one of the few, though limited in scope, flow visualization studies, Focke and Knibbe (1986) observed a lateral recirculation behavior sketched in Fig. 2a (actual clear photo-images for this case are not reported in the paper). By using an electrode-activated pH indicator method (Merzkirch, 1987) it was found that flow separation occurs downstream of wall crest at Re ~ 200, and the separated region increases in size with Re until the reattachment point almost coincides with the top of the next wall waviness crest. Nishimura et al. (1986, 1990) employed hydrogen-bubble-generation and dye-injection methods to observe a similar flow separation and recirculation behavior in the troughs of a sinusoidal wavy channel as shown in Fig 2b. Above a critical Re value (<1000) shear-layer instability was seen to set in where recirculation zones interacted with the core fluid to yield macroscopic mixing. Rush et al. (1999) also used dye-injection technique to investigate laminar–turbulent transition flow behavior in sinusoidal wavy passages (α = 0.1; $1.064 \leq \varepsilon \leq 2.0$; $0.172 \leq \gamma \leq 0.208$). They found transition with onset of macro-mixing at relatively low Re (~200–300), which is perhaps due to the relatively large inter-plate spacing ε in their experimental channels. This tends to attenuate wall-viscous effects and allow the vortices to expand into the core flow field (Zhang et al., 2004) that could further promote instabilities.

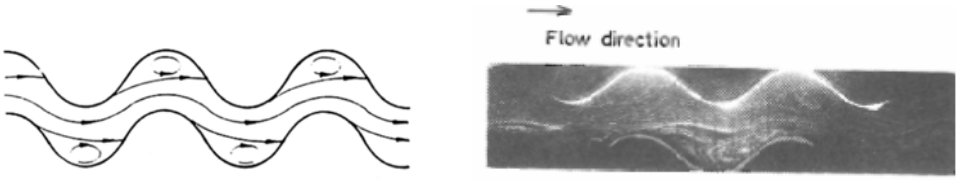

(a) (b)

FIG. 2: Flow behavior in sinusoidal wavy-plate channels: (a) sketch of streak lines for flow with Re ~ 200, $\alpha = 0.1$, $\varepsilon = 2.0$, and $\gamma = 0.5$ (Focke, 1986), and (b) photo of dye streak lines in flow with Re = 350, $\alpha = 0.065$, $\varepsilon = 1.857$, and $\gamma = 0.25$ (Nishimura, 1986)

Given the importance of wavy-plate channels to numerous engineering applications (Bergles, 1998; Manglik, 2003; Shah and Sekulic, 2003; Webb and Kim, 2005), and the rather sparse and inconclusive literature on their confined flow behavior, this study presents flow visualization results to characterize the wall-corrugation induced swirl behavior. The recirculation cell and local vortex structure in the flow field is captured by photographically recording the patterns displayed by illuminated micro-particles seeded in water flows through the test section. The velocity field is further characterized by LDV measurements of the spatial variations in different lateral planes of the sinusoidal wavy channels. Sinusoidal-wavy-plate channels of rectangular cross sections ($0.067 \le \alpha \le 0.267$; which, in effect, represents $\alpha \to 0$), with a fixed amplitude but different corrugation wavelengths ($\gamma = 0.25$ and 0.5) and inter-plate spacings ($\varepsilon = 0.5$, 1.0, 1.5 and 2.0) are considered in an effort to highlight the parametric effects of the wavy-wall geometry. These findings extend our understanding of swirl-flow behavior in the corrugated channels, and provide new insights into the consequent forced convective enhancement mechanisms.

2. EXPERIMENTAL APPARATUS AND METHODOLOGY

A closed-loop recirculating water-channel apparatus, as schematically depicted in Fig. 3a, was used in this study for the flow-visualization experiments and LDV measurements. The water channel is constructed of clear acrylic (Plexiglass) so as to provide visual access to the flow field as well as allow optical-interference-free LDV measurements. It consists of the requisite corrugated-channel test section, preceded by a flow-development section (straight channel), a centrifugal pump, volumetric rate rotameter, differential pressure transducer, digital high-resolution camera, light-absorbing back screen, aluminum dust (micro-particle) injector, water tank, and flow control valves. Upstream of the test section, the flow is conditioned by a honeycomb section so as to suppress any external disturbances and render it with a fully developed velocity profile in the flow-development (straight channel) entrance region prior to the inlet of the test section. This condition with its char-

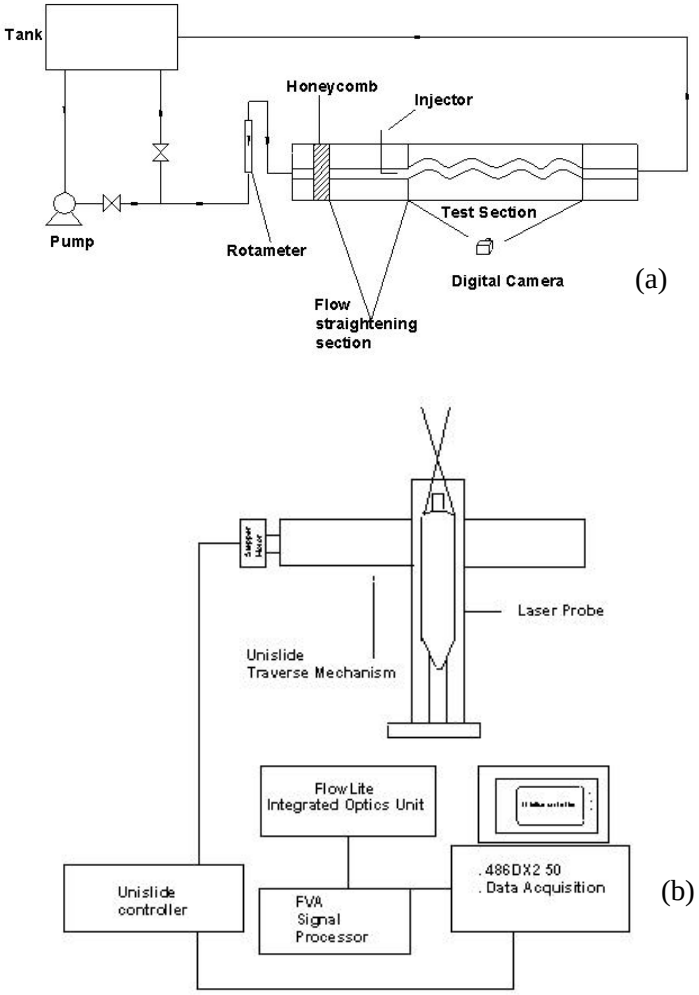

FIG. 3: Experimental set up and test apparatus: (a) closed-loop water channel with corrugated-plate-fin channel test section, and (b) LDV system optics and data acquisition

acteristic Poiseuille (parabolic) velocity profile was ascertained and established by LDV measurements (Vyas and Manglik, 2005). Besides the pump controls and a throttling valve, a bypass line with valves provides the requisite control of volumetric flow rate through the test section, which in turn is measured by a precision calibrated (±2% full-scale accuracy; ±1% repeatability) inline rotameter (Omega FL-115). The pressure drop across the test section is measured by a low-pressure high-resolution differential pressure transducer (Setra C230; ±0.25% full-scale precision). Wavy- or corrugated-plate rectangular-channel test sections that have two opposite walls with in-phase sinusoidal waviness and four different geometry fea-

TABLE 1: Geometrical listing of sinusoidal wall corrugated-plate channel test sections for flow visualization experiments and LDV measurements

	$\alpha = S/H$	$\gamma = 2A/L$	$\varepsilon = S/2A$
TS – 1	0.067	0.25	1.0
TS – 1a	0.133	0.25	0.5
TS – 2	0.10	0.25	1.5
TS – 3	0.133	0.50	1.0
TS – 4	0.20	0.50	1.5
TS – 4a	0.267	0.50	2.0

tures were used in the experiments, and their parametric descriptions are listed in Table 1.

In the visualization experiments, fluid flow patterns were photographically recording their contrasted and illuminated display. This was achieved by injecting low concentrations of micron-sized (63 μm) aluminum dust (specific gravity ~1) in the flow field and illuminating it longitudinally over a two-wavelength corrugation length with a high-luminosity light sheet. The images of observed flow patterns (recirculating cells in the axial flow field) were then captured in real time via a high-resolution digital camera with a shutter speed of 1/8th second.

To measure the spatial variations in the velocity field in different planes of axial flow through the wavy-channel test sections, a 10-mW He–Ne LDV system schematically shown in Fig. 3b was used. The probe has two different front lenses with focal lengths of 160 and 310 mm, with a 0.18-mm aperture in the latter case. For the LDV measurements, the flow field was seeded with ultra-fine particles (Dantec Dynamics: silver-coated hollow glass spheres, 13-μm diameter, 1.6-g/cc density).

The velocity measurements and fully-developed laminar flow conditions were validated by the signature parabolic velocity profile obtained for flow in a straight parallel-plate channel, for which more details are given in (Vyas and Manglik, 2005). Furthermore, and as shown in the subsequent section, there is good agreement of the axial flow field with recirculation in the wavy-plate channel troughs with limited computational results (Zhang et al., 2004; Manglik et al., 2005) for the same conditions. The maximum errors or uncertainties in the experimental determination of axial velocity u and flow Re, estimated by the single-sample error-propagation method (Moffat, 1988), were determined to be ±1% and ±3%, respectively.

3. RESULTS AND DISCUSSION

That the sinusoidal corrugated two opposite walls of the plate-fin rectangular channel induce and promote fluid recirculation in the trough regions is evident from the

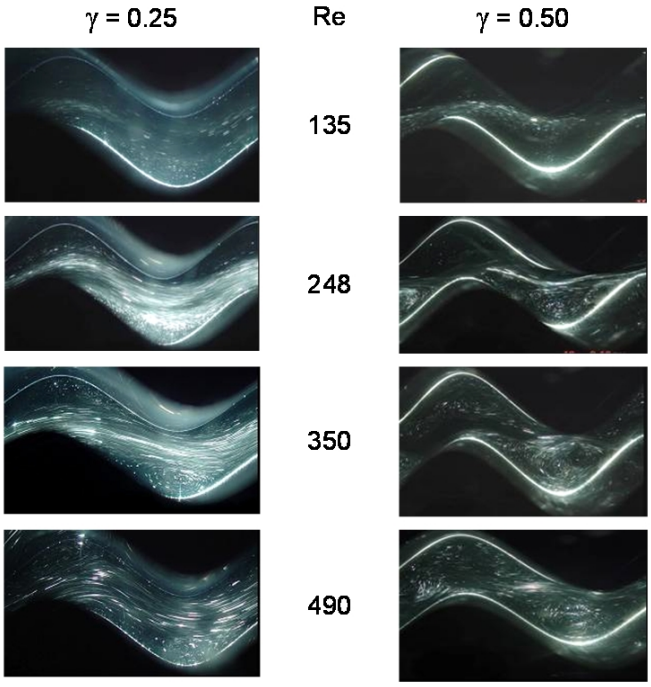

FIG. 4: Effect of the Reynolds number 135 ≤ Re ≤ 490) and severity of wall waviness (γ = 0.25 and 0.50, ε = 1.0) on the fluid recirculation or lateral vortex flow patterns in the troughs of the corrugated walls of wavy-plate channels

experimental results presented in this study from both flow visualization and LDV measurements. The steady-state swirl-flow structure is essentially two-dimensional because of the low cross-section aspect ratio (0.067 ≤ α ≤ 0.267) of the rectangular duct test sections in this study, which obviates end-wall effects that would lend to three dimensionality (Manglik et al., 2005). The initiation of fluid recirculation cells or swirl, in steady low Re flows, is shown to be effected by virtue of flow separation at discrete locations on the corrugated surface, and their spatial evolution is essentially predicated on the channel geometry and flow condition. The strength of these lateral vortices in the steady-state axial flow field are further seen to be strongly influenced by the severity of the wall-corrugation geometry (0.25 ≤ γ ≤ 0.5), the inter-wavy-plate spacing (1.0 ≤ γ ≤ 1.5), and flow Reynolds number (135 ≤ Re ≤ 700).

Figure 4 depicts the spatial development and growth of a steady lateral vortex in the concavities of wavy-plate channels with changing flow rates and wall-waviness aspect ratio. Recirculation patterns in channels with corrugated-plate spacing of ε = 1.0 and two different wall-waviness severity ratios, γ = 0.25 and 0.5, for flows with Re = 135, 248, 350, and 490 are presented in the photographic records,

which clearly show the strong influences of Re and γ on the swirl behavior. At relatively lower flow rates (Re ~ 135), viscous forces dominate to produce undisturbed streamline flows and swirl is not developed, irrespective of the wall-corrugation severity (γ = 0.25 or 0.5). The fluid essentially meanders through the channel and follows or adopts its wavy path; as a consequence, the residence time and shear loss of the flow increases. With increasing flow rates or Reynolds number, wall-curvature-induced effects manifest themselves in fluid separation downstream of the wavy-surface peak, its reattachment upstream of the subsequent peak, and the consequent development and encompassing of fluid recirculation cells (lateral swirl) in the wall-valley regions. The higher fluid inertia causes the flow to overcome viscous retardation near the wall as the latter surface curves downwards (downstream of corrugation peak), separate from it and impinge at the subsequent upward curving surface. As a result, a recirculating fluid bubble is created that is fed by a portion of the oblique spreading fluid around the impingement zone that flows backwards (or upstream of main flow or reverse flow) to form a lateral vortex cell, which is encapsulated by the core axial flow and wall trough.

Formation of a lateral vortex or swirl in the trough-region is further found to be triggered at a much lower flow rate in channels with relatively more severe wall waviness. This is evident from the flow-structure visuals in Fig. 4 for the case with wall-waviness aspect ratio of γ = 0.5. The recirculating structure is rather well established at Re ~ 248, as compared to the higher flow inertia or Re ~ 350 needed for the comparable condition to be attained in the channel with γ = 0.25. Note that the wavy-plate separation in both cases, corresponding to their different γ (= $2A/L$) values, is such that the effective inter-plate spacing is the same with ε = ($S/2A$) = 1.0. The extent of the spatial flow-area coverage of the lateral vortex and its expansion into the core axial flow increases with fluid inertia, or Re, as well as with the severity of wall corrugation, or γ. This is particularly evident in the swirl-flow patterns with Re = 490 in Fig. 4. It is seen that with γ = 0.5 the vortex cell encompasses almost the entire wall-trough region, and substantially encroaches into the axial core-flow section of the channel.

The spatial evolution (onset, growth, and expansion) of the recirculation behavior in the valleys of the corrugated wall is also seen in the computational simulations of Zhang et al. (2004), as depicted in Fig. 5. The numerical results, obtained by second-order accurate finite-volume techniques with a non-orthogonal nonstaggered grid in the channel with γ = 0.25, ε = 1.0, and α = 0.067, indicate that at low flow rates (Re < 200) the fluid simply follows an undisturbed streamline path that contours the wall waviness or periodic curvature modulations. This, however, increases the flow residence time, which manifests in higher period-averaged wall-shear or friction loss (Metwally and Manglik, 2004; Zhang et al., 2004). With increasing Re (>200), lateral recirculation is induced by the wall-corrugation curvature in the trough regions. The lateral swirl cell, although encapsulated by the core axial flow that undulates along the sinusoidal wall profile of the channel, expands and grows spatially with higher flow rate or Reynolds number. This computation-

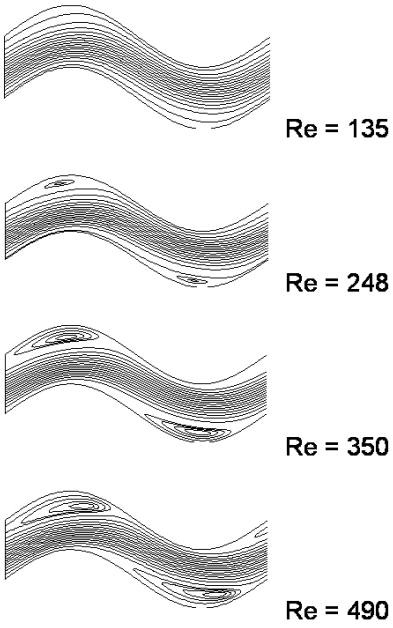

FIG. 5: Computational simulation of spatial growth of lateral recirculation in troughs of sinusoidal wavy-plate channel with $\gamma = 0.25$, $\varepsilon = 1.0$, and $\alpha = 0.067$ (Zhang et al., 2004)

ally simulated flow structure, depicted in Fig. 5 and described by the spatial variation and expansion of secondary circulation as a function of Re and γ, is essentially the same as that depicted in the flow visualization images of Fig. 4, thereby supplementing the primary characterization given by the experimental observations.

The influence of wavy-plate or inter-fin spacing, represented by the dimensionless ratio ε ($S/2A$), on the development and distribution of flow recirculation in the wavy-wall valleys is further delineated in Fig. 6. Photographic records of visualized streamlines for flows with Re = 135 and 490, $\gamma = 0.5$ and 0.25, and $\varepsilon = 1.5$ are presented in this figure. A comparison of these swirl-flow structure results with similar patterns in corrugated channels with $\varepsilon = 1.0$ shown in Fig. 4 is revealing. With increasing Re and/or inter-plate-spacing ratio ε, the lateral vortex in the trough tends to grow and expand into much of the core-flow region thereby promoting increased momentum transport. A portion of the core region tends to, nevertheless, exhibit undisturbed axial flow that simply undulates with the periodic wall waviness and follows a path of least resistance. The decreased inter-plate separation ($\varepsilon = 1.5 \rightarrow 1.0$) contrarily suppresses swirl, as wall-viscous effects become significant, and undisturbed streamline flow prevails that once again generally follows the channel-wall contours. Opening up of the plate spacing (or larger ε; which directly corresponds to fin density in compact heat exchange cores) reduces viscous dampening of the flow and helps produce the later fluid swirl in the

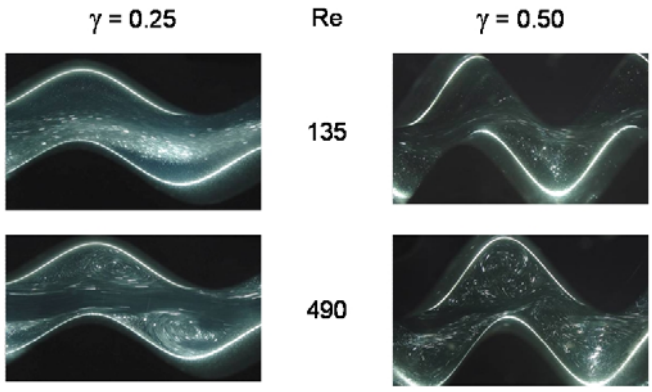

FIG. 6: Flow patterns in sinusoidal corrugated-plate channels (ε = 1.5, γ = 0.25 and 0.5) and their variation with Reynolds number

trough regions of wall corrugations. This behavior, of course, depends on the composite interaction between the channel geometry and flow variables that are represented by γ, ε, and Re.

The characteristic signature of the lateral vortex or swirl-flow behavior is further rendered in the LDV measurements of this study that are presented in Figs. 7 and 8, respectively, for ε = 1.0 and 1.5; γ = 0.25 in both cases. The LDV measurements map the lateral distribution of the axial velocity fields in the mid-plane of

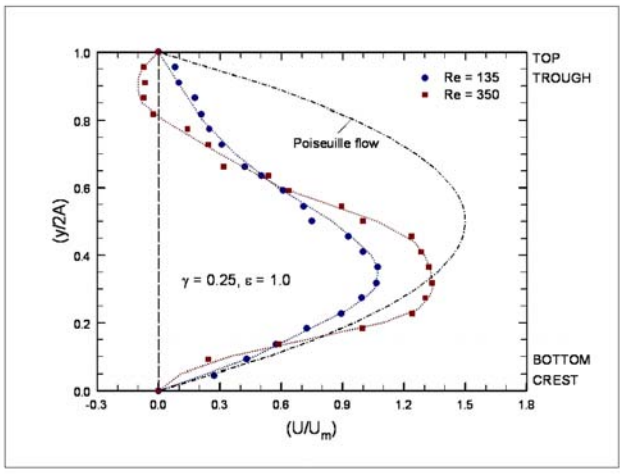

FIG. 7: LDV measurements of axial velocity distribution in the transverse peak-to-trough mid-plane of the wavy-plate channels with γ = 0.25 and ε = 1.0, and their comparison with Poiseuille flow in an equivalent plain parallel-plate channel

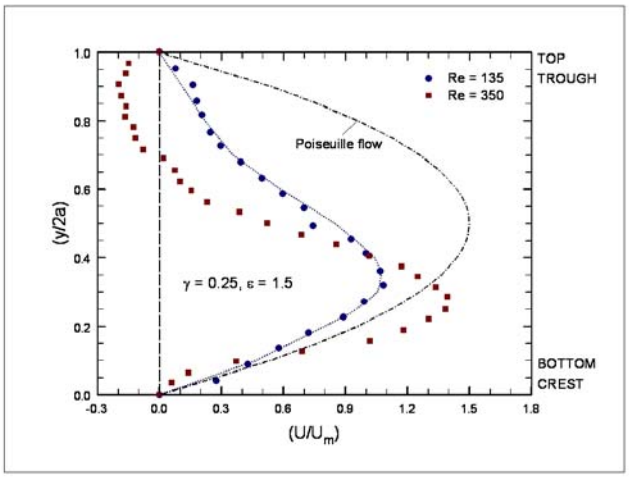

FIG. 8: LDV measurements of axial velocity distribution in the transverse mid-plane in the trough of the wavy-plate channels with $\gamma = 0.25$ and $\varepsilon = 1.5$, and their comparison with Poiseuille flow in an equivalent plain parallel-plate channel

the flow channel (bottom corrugation peak-to-trough of top corrugation along the *y*-axis). In Fig. 7, the reversed or negative flow velocity in the wavy-wall concavity ($0.8 \le y/2A \le 1.0$) seen in the Re = 350 data essentially encapsulates the lateral swirl. With a lower flow rate (Re = 135), however, there is no recirculation and the wall curvature of the plates only tends to non-symmetrically displace the axial peak velocity location away from the trough region. Relative to the Poiseuille flow distribution in an equivalent parallel-plate channel, the maximum velocity location gets skewed towards $(y/2A) \sim 0.35$ in the wavy-plate channel. When the inter-plate separation increases ($\varepsilon = 1.0 \rightarrow 1.5$), again as seen in Fig. 8 with Re = 350, the spatial coverage ($0.675 \le y/2A \le 1.0$) and magnitude of the reverse flow (peak reverse-flow $u/u_m \approx -0.225$) increases, when compared to that with $\varepsilon = 1.0$. The relative magnitude of the positive peak velocity also increases, but gets skewed further towards the opposite plate-wall crest or $(y/2A) \sim 0.25$.

An important scaling measure of combined effects of the wall-waviness aspect ratio γ and inter-fin or plate-spacing ratio ε on the production of lateral swirl in the troughs of the corrugated-plate duct at a given flow rate is the relative size of the recirculation cell. One way to ascertain this is by tracking the location of the axial flow reattachment point downstream of the vortex cell. This, in effect, demarcates the wall-trough region occupied by the steady lateral swirl that, in turn, is separated from and enveloped by the core axial flow. The compound interaction of γ and ε on the spatial coverage or size of the trough-region swirl at a fixed flow rate (Re = 600) can be deduced from Fig. 9. With increasing wall-waviness ratio γ and/or plate-spacing ratio ε, represented by the product $(\gamma \times \varepsilon)$, the lateral

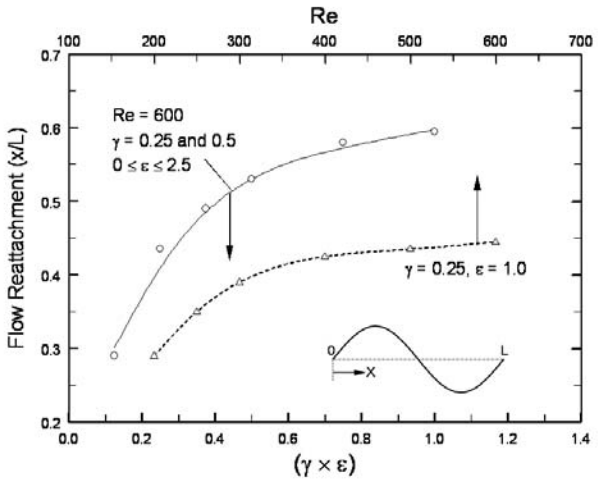

FIG. 9: Variation in position of reattachment of axial flow that envelopes the lateral recirculation or vortex cell with changes in severity of wall waviness ratio γ, wavy-plate separation ratio ε, and Reynolds number

vortex in the trough tends to grow and enlarge into much of the core-flow region. This results in the axially rightward movement of the axial-flow reattachment points, as seen in Fig. 9 and given by the (x/L) locations, with increasing ($\gamma \times \varepsilon$), thereby indicating growth of the separated region. There is nevertheless an upper limit to the wall/duct geometry's swirl promoting influence, as the reattachment position is seen to attain an asymptotically constant value, i.e., the size of the separated region remains constant and is unaffected by further increase in ($\gamma \times \varepsilon$). Such behavior is also evident in the variation of reattachment location with increasing Re in Fig. 9 for a wavy-plate channel with $\gamma = 0.25$ and $\varepsilon = 1.0$. As the plate separation decreases ($\varepsilon \rightarrow 0.5$), however, viscous effects tend to suppress swirl and the decreasing reattachment location indicates this. In the limit, with very small ε or low Re, undisturbed streamline flow prevails that follows channel-wall contours.

4. CONCLUSIONS

Swirl or fluid recirculation in wavy-fin plate channels have been analyzed using flow visualization and LDV measurements. These experiments reveal the complex interactions of flow Reynolds number and channel geometry (characterized by waviness aspect ratio γ, and inter-plate spacing ratio ε), that govern the onset, size and strength of the recirculation or lateral vortex structures in the wavy-plate troughs. At low flow rates (Re ~ 10), viscous forces dominate and the flow tends to meander along the wavy-wall-channel path without triggering flow separation.

With increasing flow rates, however, wall-curvature-induced effects cause the flow to separate downstream of the wavy surface peak forming a vortex in the wall-valley region. The onset of this lateral vortex occurs at a much lower flow rate in channels with more severe wall waviness (Re ~ 50 with $\gamma = 0.5$, as compared to Re > 100 with $\gamma = 0.25$; $\varepsilon = 1.0$ in both cases), and the extent of the lateral swirl flow area coverage increases with Re and γ. Also, when the inter-plate separation increases ($\varepsilon = 0.5 \rightarrow 1.5$), the spatial coverage and the magnitude of the reverse flow increases and the recirculating flow cell gets skewed towards the opposite plate-wall crest. The compound interaction of γ and ε, represented by the product ($\gamma \times \varepsilon$), manifests in the growth of the flow separation region until attaining an asymptotically constant value with increasing ($\gamma \times \varepsilon$). The experimental results agree well with computational predictions, and they essentially characterize the structure of swirl or lateral flow recirculation in the wall concavities of wavy-fin plate channels, and the governing effects of flow conditions and channel geometry.

ACKNOWLEDGMENTS

This study was supported in part by the Procter & Gamble Co., the Thermal-Fluids & Thermal Processing Laboratory, and the Graduate School, University of Cincinnati. Also, the advice and assistance of Craig Goulbourne, Dantec Dynamics, and Doug Hurd and Bo Westheider, College of Engineering and Applied Science, with different aspects of the experiments, are gratefully acknowledged.

REFERENCES

Amano, R. S., A numerical study of laminar and turbulent heat transfer in a periodically corrugated wall channel, *J. Heat Transfer*, vol. 107, no. 3, pp. 564–569, 1985.

Asako, Y. and Faghri, M., Finite-volume solutions for laminar flow and heat transfer in a corrugated duct, *J. Heat Transfer*, vol. 109, no. 3, pp. 627–634, 1987.

Asako, Y., Nakamura, H., and Faghri, M., Heat transfer and pressure drop characteristics in a corrugated duct with rounded corners, *Int. J. Heat Mass Transfer*, vol. 31, pp. 1237–1245, 1988.

Beloborodov, V. G. and Volgin, B. P., Heat transfer and pressure drop in heat transfer equipment with slot channels of varying cross-section, *Int. Chem. Eng*., vol. 11, no. 2, pp. 229–233, 1971.

Béreiziat, D., Devienne, R., and Lebouché, M., Local flow structure for non-Newtonian fluids in a periodically corrugated wall channel, *J. Enhanced Heat Transfer*, vol. 2, nos. 1–2, pp. 71–77, 1995.

Bergles, A. E., Techniques to enhance heat transfer, in W. M. Rohsenow, J. P. Hartnett, and Y. I. Cho (Eds.), *Handbook of Heat Transfer*, New York, NY: McGraw-Hill, pp. 11.1–11.76, 1998.

Castellões, F. V., Quaresma, J. N. N., and Cotta, R. M., Convective heat transfer enhancement in low Reynolds number flows with wavy walls, *Int. J. Heat Mass Transfer*, vol. 53, nos. 9–10, pp. 2022–2034, 2010.

Comini, G., Nonino, C., and Savino, S., Effect of space ratio and corrugation angle on convection enhancement in wavy channels, *Int. J. Numer. Meth. Heat Fluid Flow*, vol. 13, no. 4, pp. 500–519, 2003.

Focke, W. W. and Knibbe, P. G., Flow visualization in parallel-plate ducts with corrugated walls, *J. Fluid Mech*., vol. 165, pp. 73–77, 1986.

Garg, V. K. and Maji, P. K., Flow and heat transfer in a sinusoidally corrugated channel, *Int. J. Eng. Fluid Mech*., vol. 1, no. 3, pp. 293–319, 1988.

Goldstein, R. L. and Sparrow, E. M., Heat/mass transfer characteristics for flow in a corrugated wall channel, *J. Heat Transfer*, vol. 99, no. 2, pp. 187–195, 1977.

Gradeck, M., and Lebouché, M., Wall shear measurement inside corrugated channels using the electrochemical technique, *Exp. Fluids*, vol. 24, no. 1, pp. 17–26, 1998.

Gschwind, P., Regele, A., and Kottke, V., Sinusoidal wavy channels with Taylor–Goertler vortices, *Exp. Thermal Fluid Sci*., vol. 11, pp. 270–275, 1995.

Hwang, S. D., Jang, I. H., and Cho, H. H., Experimental study on flow and local heat/mass transfer characteristics inside corrugated duct, *Int. J. Heat Fluid Flow*, vol. 27, no. 1, pp. 21–32, 2006.

Kays, W. M. and London, A. L., *Compact Heat Exchangers*, New York, NY: McGraw-Hill, 1984.

Manglik, R. M., Heat transfer enhancement, in A. Bejan, and A. D. Kraus (Eds.), *Heat Transfer Handbook*, Hoboken, NJ: Wiley, Ch. 14, 2003.

Manglik, R. M. and Bergles, A. E., Heat transfer and pressure drop correlations for the rectangular offset-strip-fin compact heat exchanger, *Exp. Thermal Fluid Sci*., vol. 10, no. 2, pp. 171–180, 1995.

Manglik, R. M. and Bergles, A. E., Enhanced heat and mass transfer in the new millennium: A review of the 2001 literature, *J. Enhanced Heat Transfer*, vol. 11, no. 2, pp. 87–118, 2004.

Manglik, R. M., Zhang, J., and Muley, A., Low Reynolds number forced convection in three-dimensional wavy-plate-fin compact channels: Fin density effects, *Int. J. Heat Mass Transfer*, vol. 48, no. 8, pp. 1439–1449, 2005.

Merzkirch, W., *Flow Visualization*, Orlando, FL: Academic Press, 1987.

Metwally, H. M. and Manglik, R. M., Enhanced heat transfer due to curvature-induced lateral vortices in laminar flows in sinusoidal corrugated-plate channels, *Int. J. Heat Mass Transfer*, vol. 47, no. 10–11, pp. 2283–2292, 2004.

Moffat, R. J., Describing the uncertainties in experimental results, *Exp. Thermal Fluid Sci*., vol. 1, no. 1, pp. 3–17, 1988.

Motamed Ektesabi, M. R., Sako, M., and Chiba, T., Fluid flow and heat transfer in wavy sinusoidal channels (1st Report, Numerical Analysis of Two-Dimensional Laminar Flow Field), *Nippon Kikai Gakkai Ronbunshu*, vol. 53, no. 487, pp. 722–730, 1987.

Muley, A., Manglik, R. M., and Metwally, H. M., Enhanced heat transfer characteristics of viscous liquid low Reynolds number flows in a chevron plate heat exchanger, *J. Heat Transfer*, vol. 121, no. 4, pp. 1011–1017, 1999.

Ngo, T. L., Kato, Y., Nikitin, K., and Tsuzuki, N., New printed circuit heat exchanger with S-shaped fins for hot water supplier, *Exp. Thermal Fluid Sci*., vol. 30, no. 8, pp. 811–819, 2006.

Nishimura, T., Kajimoto, Y., and Kawamura, Y., Mass transfer enhancement in channels with a wavy wall, *J. Chem. Eng. Japan*, vol. 19, no. 2, pp. 142–144, 1986.

Nishimura, T., Yano, K., Yoshino, T., and Kawamura, Y., Occurrence and structure of Taylor–Goertler vortices induced in two-dimensional wavy channels for steady flow, *J. Chem. Eng. Japan*, vol. 23, no. 6, pp. 697–703, 1990.

Nishimura, T., Yoshino, T., and Kawamura, Y., Instability of flow in a sinusoidal wavy channel with narrow spacing, *J. Chem. Eng. Japan*, vol. 20, no. 1, pp. 102–103, 1987.

O'Brien, J. E. and Sparrow, E. M., Corrugated-duct heat transfer, pressure drop, and flow visualization, *J. Heat Transfer*, vol. 104, no. 3, pp. 410–416, 1982.

Rush, T. A., Newell, T. A., and Jacobi, A. M., An experimental study of flow and heat transfer in sinusoidal wavy passages, *Int. J. Heat Mass Transfer*, vol. 42, pp. 1541–1553, 1999.

Sawyers, D. R., Sen, M., and Chang, H.-C., Heat transfer enhancement in three-dimensional corrugated channel flow, *Int. J. Heat Mass Transfer*, vol. 41, pp. 3559–3573, 1998.

Selvarajan, S., Tulapurkara, E. G., and Vasanta Ram, V., Stability characteristics of wavy walled channel flows, *Phys. Fluids*, vol. 11, no. 3, pp. 579–589, 1999.

Shah, R. K. and Sekulic, D. P., *Fundamentals of Heat Exchanger Design*, New York, NY: Wiley, 2003.

Sparrow, E. M. and Comb, J. W., Effect of interwall spacing and fluid flow inlet conditions on a corrugated-wall heat exchanger, *Int. J. Heat Mass Transfer*, vol. 26, no. 7, pp. 993–1005, 1983.

Sparrow, E. M. and Hossfeld, L. M., Effect of rounding of protruding edges on heat transfer and pressure drop in a duct, *Int. J. Heat Mass Transfer*, vol. 27, no. 10, pp. 1715–1723, 1984.

Stasiek, J., Collins, M. W., Ciofalo, M., and Chew, P. E., Investigation of flow and heat transfer in corrugated passages — I. Experimental results, *Int. J. Heat Mass Transfer*, vol. 39, no. 1, pp. 149–164, 1996.

Vajravelu, K., Fluid flow and heat transfer in horizontal wavy channels, Acta Mechanica, vol. 35, pp. 245–258, 1980.

Vyas, S. and Manglik, R. M., Experimental Characterization of Vortex Structure in Sinusoidal Wavy Channels and a Case Study for Fuel Cell Applications, Report No. TFTPL-12, Thermal-Fluids & Thermal Processing Laboratory, University of Cincinnati, Cincinnati, OH, 2005.

Wang, C.-C., Technology review — A survey of recent patents of fin-and-tube heat exchangers, *J. Enhanced Heat Transfer*, vol. 7, no. 5, pp. 333–345, 2000.

Webb, R. L. and Kim, N.-H., *Principles of Enhanced Heat Transfer*, Boca Raton, FL: Taylor & Francis, 2005.

Yang, L. C., Asako, Y., Yamaguchi, Y., and Faghri, M., Numerical prediction of transitional characteristics of flow and heat transfer in a corrugated duct, *J. Heat Transfer*, vol. 119, no. 1, pp. 62–69, 1997.

Zhang, J., Kundu, J., and Manglik, R. M., Effect of fin waviness and spacing on the lateral vortex structure and laminar heat transfer in wavy-plate-fin cores, *Int. J. Heat Mass Transfer*, vol. 47, nos. 8–9, pp. 1719–1730, 2004.

Zhang, X. and Tafti, D. K., Flow efficiency in multi-louvered fins, *Int. J. Heat Mass Transfer*, vol. 46, no. 10, pp. 1737–1750, 2003.

Zimmerer, C., Gschwind, P., Gaiser, G., and Kottke, V., Comparison of heat and mass transfer in different heat exchanger geometries with corrugated walls, *Exp. Thermal Fluid Sci.*, vol. 26, pp. 269–273, 2002.

Journal of Flow Visualization & Image Processing 17(4), 297–307 (2010)

BUBBLE DEPARTURE FROM METAL-GRAPHITE COMPOSITE SURFACES AND ITS EFFECTS ON POOL BOILING HEAT TRANSFER

David F. Chao,[1] John M. Sankovic,[1] Brian J. Motil,[1] W-J. Yang,[2] & Nengli Zhang[3]*

[1]*NASA Glenn Research Center, Cleveland, OH 44135*

[2]*The University of Michigan, Ann Arbor, MI 48109*

[3]*Ohio Aerospace Institute at NASA Glenn Research Center, Cleveland, OH 44135*

[*]Address all correspondence to Nengli Zhang E-mail: nzhang@grc.nasa.gov

The formation and growth processes of a bubble in the vicinity of graphite micro-fiber tips on metal-graphite composite boiling surfaces and their effects on boiling behavior are investigated. It is discovered that a large number of micro bubbles are formed first at the micro scratches and cavities on the metal matrix in pool boiling. By virtue of the non-wetting property of graphite, once the growing micro bubbles touch the graphite tips, the micro bubbles are sucked by the tips and merged into larger micro bubbles sitting on the end of the tips. The micro bubbles grow rapidly and coalesce to form macro bubbles, each spanning several tips. The necking process of a detaching macro bubble is analyzed. It is revealed that a liquid jet is produced by sudden break-off of the bubble throat. The composite surfaces not only have higher temperatures in micro- and macrolayers but also make higher frequency of the bubble departure, which increase the average heat fluxes in both the bubble growth stage and in the bubble departure period. Based on these analyses, the enhancement mechanism of pool boiling heat transfer on composite surfaces is clearly revealed.

KEY WORDS: *micro bubbles, macro bubbles, macro bubble departure, bubble necking, liquid jet, boiling heat transfer enhancement*

1. INTRODUCTION

It is well known that nucleate boiling is an extremely effective mode of heat transfer. Although over the years researchers have studied the boiling process theoretically and experimentally, there are no theories in the literature that precisely explain the underlying heat transfer mechanisms. However, an accepted theory is

NOMENCLATURE

D	micro bubble diameter	**Greek symbols**	
$\mathcal{D}$	macro bubble diameter	α	volume fraction of the graphite fiber in the composite material
d	graphite fiber diameter	Δ	height of the fiber tip plateau
p	pressure	Δp	pressure difference
R	second principal radius of curvature of the vapor–liquid interface	δ	average thickness of microlayer
		δ_m	maximum thickness of microlayer
r	first principal radius of curvature of the vapor–liquid interface	ρ	density
		σ	surface tension
		Subscripts	
S	distance between coalescence plane and fiber tip	b	bottom
		d	departure
V_m	volume of microlayer in a micro bubble unit	l	liquid
		T	top of bubble
W	vapor velocity	th	throat
		v	vapor

that bubble nucleation, growth, and departure control the heat and mass transport rate. The basic understanding of boiling phenomena on plain surfaces brought about concepts to modify the process through changing properties of the working fluid and/or the boiling surface to increase the boiling heat transfer coefficient. A new passive technique, called metal-graphite composite surfaces, was presented and studied by Yang et al. (1991). Since then a series of investigations have been performed to determine the enhancement effects of composite surfaces on boiling heat transfer and their mechanism (see, e.g., Zhang et al., 1992; Yang, 1995; Liang, 1997). The practical importance of the new enhancement technique applying to Multi-Chip Modules (MCM) was discussed by Vrable (2001). Chao et al. (2004) conducted experiments on nucleate pool boiling both in a highly wetting liquid, Freon-113, and a moderately wetting fluid, water, on Cu–Gr composite surfaces with different fiber volume fractions. The experimental results have shown that significant enhancement in pool boiling heat transfer performance in both highly wetting liquids and moderate wetting liquids occurs on Cu–Gr composite surfaces.

The enhancement mechanisms of boiling on the composite surfaces are believed to be related to: 1) the higher thermal conductivity of micro-graphite fibers, 2) a large number of embryo cavities of appropriate size, and 3) the poorly wetted

property of graphite fiber tips (Liang and Yang, 1998). In order to clarify the physics of the enhancement, it is important to have an understanding of the processes of bubble formation, growth and departure and their effects on the boiling heat transfer.

For common solid surfaces, numerous models have been developed to predict bubble detachment diameters in pool boiling and were reviewed by Zeng et al. (1993). Many experiments have shown that bubble detachment had been implemented by a necking process (see van Stralen et al., 1975; Nordmann and Mayinger, 1981; Mitrovic, 1997, 1998; Mori and Baines, 2001). Mitrovic (1997, 1998) analyzed the movement of three-phase-line (TPL) and the formation of bubble neck during bubble growth. He conjectured that evaporation at TPL tended to create a convex interface, leading to Laplace-pressure, which pushed the liquid radially outward to form the bubble neck. Kandlikar and Steinke (2002) suggested that an intense evaporation at the TPL exerted a vapor recoil force pushing the interface into the liquid and consequently, a convex vapor–liquid interface was formed and developed into the bubble neck. The bubble necking and brake-off processes were described by Mitrovic (1997) and Mori and Baines (2001), but the dynamic process has not been properly analyzed. Recently, Zhang et al. (2006) analyzed the detail dynamic process of the bubble growth on a cavity. The bubble necking and departure were mathematically described, and subsequently, a determination method of the bubble departure diameter was presented. It certainly is of interest to understand the bubble behavior on the composite surfaces and its effects on the boiling heat transfer. This paper analyzes the micro- and macro-bubble formation, growth on a metal–graphite composite surface, and the macro bubble departure dynamic processes from the surface. The mechanism of a liquid jet formation after the macro bubble departure has been revealed. The effects of the bubble departure on the boiling heat transfer are discussed.

2. FORMATION AND GROWTH OF MICRO BUBBLES

Different from common metal surfaces, metal–graphite composite surfaces each have their unique geometric and physical characteristics. The polished composite surfaces are smooth in macro scale but rough in micro scale. Yang (1995) investigated the surface structure of Cu–Gr composite surfaces through a scanning electronic microscope (SEM). Direct top-view photomicrographs of a Cu–Gr composite specimen with a volume fraction of 50% graphite-fiber and a fiber diameter of 8–10 μm clearly show that the graphite fibers are embedded in the copper matrix perfectly without any gap or void. The photomicrographs also show that the fiber tips are rather smooth while the copper matrix surface is filled with a large number of micro size low-lying trenches and intermingled narrow grooves. A slightly tilted top-view of the composite surface shows that the fiber tips bulge out of the copper matrix, surviving the polishing due to their pliability and tenacity, and form individual plateaus distributing evenly on the composite surfaces.

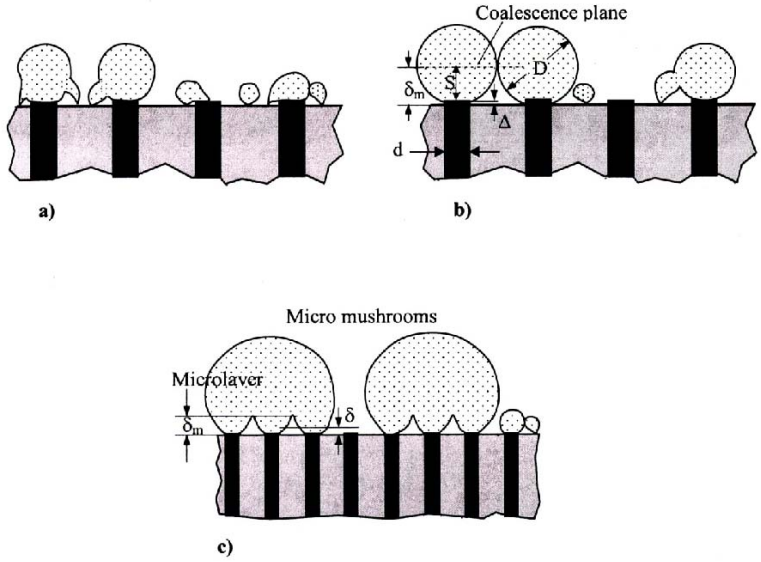

FIG. 1: Initiation and growth of micro bubbles: a) initiation and migration of micro bubbles; b) growing of micro bubbles firmly sitting on the fiber tips; c) growth of coalesced micro bubbles and formation of micro mushrooms

Contrary to intuition, the preliminary experimental observations have found that the micro bubbles originate from the valleys between the fiber tip plateaus instead of the fiber tips. It is obviously attributed to the fact that plenty of potential nucleate sites are created by the micro-sized trenches and intermingled narrow grooves on the copper matrix surface. On the other hand, although the fiber tips may have higher temperatures than the copper matrix surface, the relative smooth surface of the fiber tip plateaus hardly provide initial nucleate sites.

Once the growing micro bubbles touch the fiber tips, the micro bubbles tend to migrate to the tips from the copper matrix and firmly sit on the tips for the poor wetting characteristic of the graphite and a large surface tension at the TPL. As the micro bubbles sitting on the fiber tips grow, the newly emerging embryo bubbles on the copper matrix are swallowed by the micro bubbles at contact, as shown in Fig. 1a. Both the rapid evaporation due to the higher temperature of the graphite fiber tips and the swallowing of the emerging embryo micro bubbles speed up the growth of the micro bubbles on the fiber tips. The continually growing micro bubbles inevitably coalesce with each other, as shown in Fig. 1b. The coalesced micro bubbles rapidly grow into micro mushrooms with their own microlayers forming a liquid network connected with bulk liquid under the coalesced micro bubbles, as shown in Fig. 1c.

As analyzed by Zhang et al. (1992), the micro bubbles coalesce at their maximum cross section. By reference to Fig. 1b, the micro bubble diameter at coales-

cence, D, is related to the fiber diameter, d, and the volume fraction of the graphite fiber in the composite material, α which is equal to the area fraction of the fiber tips in the composite surface, by the following equation:

$$\pi d^2/4 = \alpha D^2 . \quad (1)$$

The height of the coalescence plane of the micro bubbles is regarded as the maximum thickness of the microlayer δ_m. It can be seen from Fig. 1b that $\delta_m = \Delta + S$, where Δ is the height of the fiber tip plateau, estimated at approximately 0.3 μm, S is the distance between the coalescence plane and fiber tip, equaling $\sqrt{(D/2)^2 - (d/2)^2} = d\sqrt{\pi/(4\alpha) - 1}/2$.

Therefore,

$$\delta_m = \frac{d}{2}\sqrt{\frac{\pi}{4\alpha} - 1} + \Delta. \quad (2)$$

Based on simple geometry, the volume of the microlayer in a micro bubble unit can be calculated by

$$V_m = D^2\delta_m - \frac{1}{6}\pi S\left[\frac{3}{4}D^2 + \frac{3}{4}d^2 + S^2\right] - \frac{\pi d^2}{4}\Delta. \quad (3)$$

Idealizing the liquid volume as a column of constant cross section, the average thickness of microlayer, δ, can be derived by $V_m/(D^2 - \pi d^2/4)$. As a result, the following expression can be obtained:

$$\delta = \left[\frac{1 - \pi/6 - \alpha/3}{2(1-\alpha)}\sqrt{\frac{\pi}{4\alpha} - 1}\right] d + \Delta. \quad (4)$$

Obviously, both the maximum and average thicknesses of the microlayer are determined by the volume fraction of graphite fiber in the composite α and the fiber diameter d. As mentioned above, d = 8–10 μm. Simple calculation results for the maximum and average thicknesses of the microlayer at d = 9 μm are listed in Table 1.

In boiling heat transfer, microlayers play an important role. Thermal energy provided by the composite surface is first conducted through the microlayers and then

TABLE 1: Microlayer thicknesses at different values of α

α	0.1	0.25	0.5	0.75
δ_m, μm	12.08	6.89	3.70	1.28
δ, μm	6.10	3.75	2.41	1.19

delivered into the micro mushrooms as latent heat by evaporation at the microlayer surface. Because the microlayers are connected directly with the bulk liquid through a liquid network, the liquid evaporating off the microlayers can be replenished immediately. It is the ample feed of liquid into the microlayers that enables the composite surfaces to have lower superheats at given boiling heat fluxes, i.e., enhancement of boiling heat transfer. This is only a sweeping statement; the direct actions of the enhancement are actually executed by the macro bubble departure.

3. FORMATION OF A MACRO BUBBLE

The continually growing micro mushrooms inevitably coalesce and merge with each other to form a larger micro vapor mass, which is a macro bubble embryo, as shown in Fig. 2. When the bubble embryo is formed from several micro mushrooms, a macrolayer is created under the macro bubble embryo, connecting with the microlayers and bulk liquid through a liquid network. As analyzed by Mitrovic (1997, 1998) and Kandlikar and Steinke (2002), at the beginning of the bubble formation, the TPL of the bubble moves outwards to form a convex vapor–liquid interface at the bubble bottom, and subsequently a bubble neck is created. The same process also occurs in the growth of a macro bubble embryo on the composite surfaces. As the macro bubble embryo grows, the TPL of the macrolayer moves towards the liquid under the combination of a high evaporation rate and a capillary-pressure difference. Zhang et al. (2006) analyzed this kind of TPL moving process in detail. In the case of a macro bubble embryo formed on the metal-graphite composite surfaces, the moving TPL would stop at the next circles consisting of the corresponding neighbor graphite fiber tips for the poor wettability of the graphite fiber. Consequently, convex vapor–liquid interfaces are created at the macro bubble embryo bottom at both the inner and the outer TPLs, as shown

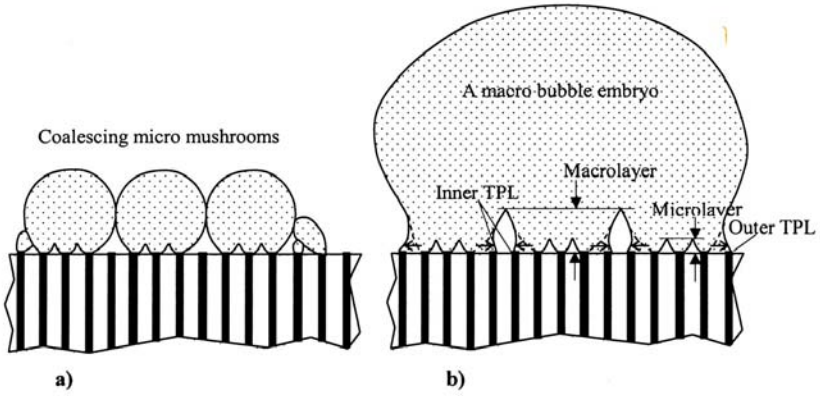

FIG. 2: Formation of a macro mushroom from coalesced micro mushrooms: a) coalescence of micro mushrooms; b) formation of a macro bubble embryo

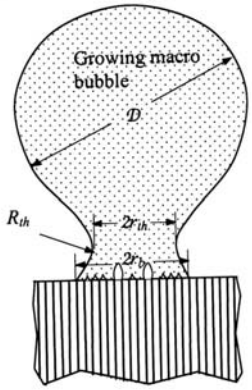

FIG. 3: Formation of a macro bubble

in Fig. 2b. The macro bubble embryo rapidly increases and finally forms a macro bubble with a neck throat, as shown in Fig. 3.

4. DEPARTURE OF A MACRO BUBBLE

The strong evaporation of liquid from the micro- and macrolayers is firmly supported by the ample liquid supply through the liquid network at the bubble bottom, and creates larger and larger negative pressures at the throat, i.e., $\Delta p_{th} = p_{v,th} - p_{l,th} < 0$, where $p_{v,th}$ and $p_{l,th}$ are the static pressures of vapor side and liquid side at the throat, respectively.

It should be noted that the static pressure difference varies along the bubble interface, as shown in Fig. 3. The static pressure difference at the top of a departing bubble, ΔP_T, can be expressed as $4\sigma/\mathcal{D}_d$, where σ is the surface tension, $\mathcal{D}_d$ is the bubble departure diameter, while the static pressure difference at the throat Δp_{th} is estimated by

$$\Delta p_{th} = \sigma/r_{th} - \sigma/R_{th} - \rho_v W_{th}^2/2 \tag{5}$$

where r_{th} and R_{th} are the first and second principal curvature radius of the vapor–liquid interface at throat, respectively, ρ_v is the density of vapor, W_{th} is the vapor velocity at throat. It should be pointed out that some researchers wrongly described the pressure difference at the throat for missing the last term in Eq. (5), which results in an unreasonable verdict: the pressure difference at the throat would always be positive and consequently no necking process would occur. It can be seen that the first two terms in Eq. (5) always give positive as soon as $R_{th} > r_{th}$, to say nothing of the small values of r_{th} with a larger R_{th}. Actually, it is the higher and higher velocity of vapor passing through the throat creates the

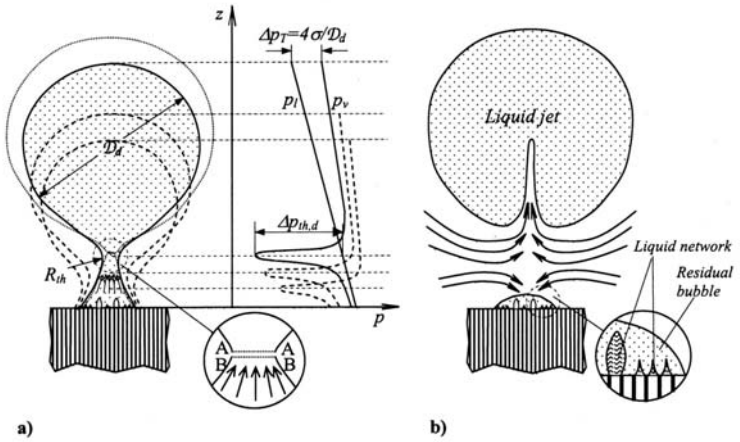

FIG. 4: Growth, necking, and departure of a macro bubble: a) necking process; b) liquid jet after the macro bubble departure

larger and larger negative pressure at the throat, as indicated mathematically by Eq. (5). It can also be concluded that a detaching bubble will never depart with zero neck diameter, i.e., $r_{th} \neq 0$, otherwise, $\Delta p_{th} \rightarrow \infty$. In other words, along with the detaching bubble growth, the throat diameter of the bubble quickly contracts to a finite value when the buoyancy exceeds the surface tension force at the throat and consequently the neck breaks off suddenly. At this time, the major portion of the bubble above the neck departs with a singular circle line A–A, as shown in Fig. 4a, where a considerable large pressure difference Δp_{th} occurs. This is the reason that a liquid jet occurs in the departure bubble. Of course, the corresponding singular line B–B is formed at the residual vapor portion sitting on the composite surface but the strong evaporation from the liquid network at the residual bubble bottom withstands the action of the sudden change of Δp_{th}, and at the same time rapidly fosters and develops a new bubble. Due to the bubble break-off at the throat suddenly occurs in a finite diameter of the neck, a huge momentum flow creates a liquid jet dashing into the bubble. It is the liquid jet that produces a violent wake of the departed bubble and induces a strong convection flow on the boiling surface to refresh the liquid network at the residual bubble, which supports the liquid supply for the new bubble growth, as depicted in Fig. 4b.

5. ENHANCEMENT OF BOILING HEAT TRANSFER

It is because of the unique structure of metal-graphite composite surfaces that the strong evaporation in macro bubbles is supported by the ample liquid supply through the liquid network connecting the macrolayers and microlayers to the bulk liquid. Consequently, a much higher heat flux can be reached, especially when the

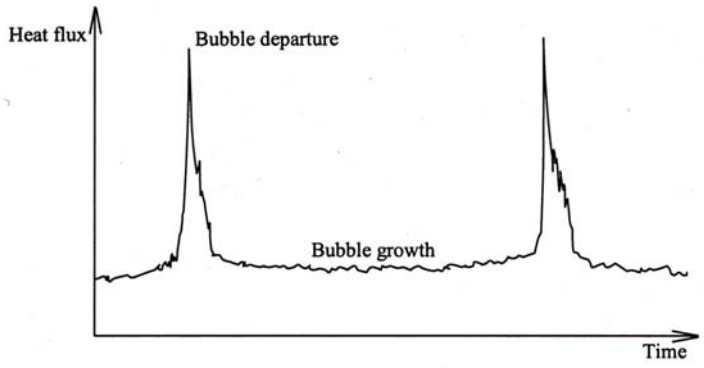

FIG. 5: Heat flux variation during a bubble life cycle

bubbles depart. As experimental demonstration by Chen and Chung (2002), a heat flux pulse takes place at the bubble departure while a lower heat flux period occurs in the bubble growth stage, as qualitatively shown in Fig. 5. The experiments using FC-72 on platinum surface made by Chen and Chung clearly show that the highest value of the heat flux pulse is about three times the heat flux in the bubble growth stage (90 W/cm^2 vs. 30 W/cm^2). Usually, higher temperatures of the micro- and macrolayers will increase the average heat flux for the larger conduction and higher evaporation rate in the micro- and macrolayers. Another efficient approach to increase heat flux is to increase the bubble departure frequency. It is easy to understand that higher frequency of bubble departure results in more heat flux pulses per unit time for the shorter bubble life cycle, and consequently, the average heat flux is increased. It is the metal–graphite composite surfaces that not only have higher temperature in micro- and macrolayers but also make higher frequency of the bubble departure, and therefore, average heat fluxes in both the bubble growth stage and the bubble departure period are increased. Based on the force balance at the neck of a departing bubble, Chao et al. (2004) have theoretically and experimentally demonstrated that higher vapor velocity produced by a larger local heat flux of boiling on the composite surface enables the bubbles to depart at smaller departure diameters, and consequently, results in an increased bubble departure frequency. This enhancement mechanism can successfully explain the experimental results of the enhanced boiling heat transfer both for F-113 and water (Yang et al., 1991; Chao et al., 2004).

6. CONCLUSIONS

In pool boiling on metal-graphite composite surfaces, micro bubbles originate first from the valleys between the fiber tip plateaus instead of the fiber tips on the graphite tips, and then migrate to the tips. The growing micro bubbles sitting on

the fiber tips coalesce and merge with each other to produce macro bubble embryos with a liquid network consisting of micro- and macro-layers. An important parameter, the microlayer thickness is analyzed and formulated.

It is the unique structure of metal-graphite composite surfaces that creates a liquid network connected to bulk liquid, from whom an ample supply of liquid firmly supports the strong evaporation at the surfaces of micro- and macrolayers and fosters and develops macro bubbles. During the formation process of a macro bubble, a convex-concave interface is created at the bubble bottom under the combination of a high evaporation rate and the capillary-pressure difference, and then develops to a neck with a decreasing throat diameter. It is the strong evaporation that produces increasing vapor velocities and creates a very high negative pressure at the bubble throat, which accelerates the reduction of the throat diameter and finally leads the macro bubble departure for the surface tension force failing to support the bubble against the buoyancy.

A liquid jet is created immediately after the departure of the macro bubble by a huge momentum flow due to the bubble throat break-off suddenly. The violent wake of the bubble created by the liquid jet induces a strong convection flow on the boiling surface to refresh the liquid network at the residual bubble bottom, which fosters the new bubble. It is the composite surfaces that not only have higher temperature in the micro- and macrolayers but also make higher frequency of the bubble departure, and consequently, increase the average heat fluxes both in the bubble growth stage and in the bubble departure period. In this way, the boiling heat transfer is enhanced.

REFERENCES

Chao, D. F., Zhang, N., and Yang, W. J., Nucleate pool boiling on copper-graphite composite surfaces and its enhancement mechanism, *J. Thermophys. Heat Transfer*, vol. 18, no. 2, pp. 236–242, 2004.

Chen, T. and Chung, J. N., Coalescence of bubbles in nucleate boiling on microheaters, *Int. J. Heat Mass Transfer*, vol. 45, no. 11, pp. 2329–2341, 2002.

Kandlikar, S. G. and Steinke, M. E., Contact angles and interface behavior during rapid evaporation of liquid on a heated surface, *Int. J. Heat Mass Transfer*, vol. 45, no. 18, pp. 3771–3780, 2002.

Liang, H. S., Nucleate Pool Boiling on Micro-Graphite-Fiber Composite Surfaces with Applications in Micro-Electronic Cooling, Ph.D, The University of Michigan, 1997.

Liang, H. S. and Yang, W.-J., Nucleate pool boiling heat transfer in a highly wetting liquid on micro-graphite-fiber composite surfaces, *Int. J. Heat Mass Transfe*r, vol. 41, no. 13, pp. 1993–2001, 1998.

Mitrovic, J., Formation of a liquid jet after detachment of a vapour bubble, *Int. J. Heat Mass Transfer*, vol. 40, no. 18, pp. 4309–4317, 1997.

Mitrovic, J., The flow and heat transfer in the wedge-shaped liquid film formed during the growth of a vapour bubble, *Int. J. Heat Mass Transfer*, vol. 41, no. 12, pp. 1771–1785, 1998.

Mori, B. K. and Baines, W. D., Bubble departure from cavities, *Int. J. Heat Mass Transfer*, vol. 44, no. 4, pp. 771–783, 2001.

Nordmann, D. and Mayinger, F., Temperatur, Druck und Wärmetransport in der umgebung kondensierender Blasen, VDI-Forschungsheft Nr. 605, 1981.

van Stralen, S. J. D., Cole, R., Sluyter, W. M., and Sohal, M. S., Bubble growth rates in nucleate boiling of water at subatmospheric pressures, *Int. J. Heat Mass Transfer*, vol. 18, no. 5, pp. 655–669, 1975.

Vrable, D. L., Composite material technology to enhance boiling heat transfer performance, *Int. J. Transport Phenomena*, vol. 3, no. 4, pp. 395–405, 2001.

Yang, G. W., Micro- and Macro-Phenomena in Nucleate Pool Boiling on Graphite–Copper Composite Materials, Ph.D, The University of Michigan, 1995.

Yang, W. J., Takizawa, H., and Varable, D., Augmented on copper–graphite composite surface, *Int. J. Heat Mass Transfer*, vol. 34, no. 11, pp. 2751–2758, 1991.

Zeng, L. Z., Klausner, J. F., and Mei, R., A unified model for the prediction of bubble detachment diameters in boiling systems–I. Pool boiling, *Int. J. Heat Mass Transfer*, vol. 36, no. 9, pp. 2261–2270, 1993.

Zhang, N., Chao, D. F., and Sankovic, J. M., Two basic modes of bubble growth and determination of departure diameters in pool boiling, AIAA Meeting Papers on Disc [CD-ROM], Section 142-TP-10, 983 Reno, NV, 2006.

Zhang, N., Yang, W. J., and Yang, G. W., Two-tier model for nucleate pool boiling on micro configured composite surfaces, *Int. Comm. Heat Mass Transfer*, vol. 19, no. 6, pp. 767–779, 1992.

Journal of Flow Visualization & Image Processing 17(4), 309–320 (2010)

FLOW VISUALIZATION USING HYDROGEN BUBBLE TECHNIQUE OF A FIN-AND-TUBE TYPE HEAT EXCHANGER WITH PUNCHED-OUT VORTEX GENERATORS

M. Mustafa Akbari, [*] ***Akira Murata, Sadanari Mochizuki, Kaoru Iwamoto, & Hiroshi Saito***

Department of Mechanical Systems Engineering, Tokyo University of Agriculture and Technology, Tokyo 184-8588, Japan

*Address all correspondence to M. Mustafa Akbari E-mail: Mustafa_tuat@yahoo.com

A study of the flow structure inside a fin-and-tube heat exchanger was performed by using hydrogen bubble visualization technique to examine the effects of different vortex generator geometries on the flow field, understand the formation of vortices and identify the punched-out hole effect on the flow behavior. Flow visualization results clarified flow structures and the effect of the punched holes for the studied vortex generator configurations. It is found that the vortices are created in the installed or punched forms. The strength of the vortices of installed vortex generators is more prominent compared to that of the punched vortex generators but the punched vortex generators showed smaller friction factors compared to the installed vortex generators.

KEY WORDS: *hydrogen bubble, vortex generators, secondary flow, heat exchanger, friction factor*

1. INTRODUCTION

Heat exchanger efficiency is the most important aspect of its economical success in air conditioning and refrigeration applications, and is often limited by the low airside heat transfer coefficient. The airside temperature distribution is intimately coupled to the velocity field, often taking the form of a boundary layer. This temperature distribution is a manifestation of the airside heat transfer resistance and it can be modified through flow manipulation. In design of a heat exchanger, laminar flow is often desired or necessary because of design constraints and therefore most compact heat exchangers operate with laminar developing flow. However, it may be possible in some cases to turbulate the flow and thereby increase the heat transfer but the secondary enhancement method caused by vortex generation is preferred over turbulation because laminar flow with streamwise vorticity have lower rates of entropy generation and therefore have higher performance.

1065-3090/10/$35.00

NOMENCLATURE

D	tube diameter, m
f	friction factor (= $2H/4L)(\Delta P/\rho^2 U^2$), [–]
H	fin pitch, m
L	flow length, base length of the vortex generator, m
r	distance from the center of the tube to the trailing edge of vortex generator, m
Re	Reynolds number (= $2HU/v$), [–]
S	distance between stagnation point of tube and tip of vortex generators, distance between tips of vortex generators, m
U	mean velocity, m/s
VG	vortex generator
x/H	location in fin span wise direction
y/H	location in stream wise direction
z/H	location in fin normal direction

Greek symbols

β	attack angle of the vortex generator, deg
ΔP	pressure drop, Pa
ν	kinematic viscosity, m^2/s
ρ	density, kg/m^3
θ	streamwise angle between the center of the tube and trailing edge of the vortex generator, deg

Subscripts

p	plain fin (fin-and-tube with no vortex generators)
I	pertain to "common flow up" configuration
II	pertain to "common flow down" configuration

Vortex generators enhance the airside heat transfer performance by generating longitudinal vortices or secondary flow, which produce three-dimensional swirling near-wall flow mixing with the mainstream and disturbing the thermal boundary layer. Vortex generators are enhancing the heat exchange by modifying the flow to a larger scale compared to other roughness elements such as dimples, and thus a heat exchanger incorporated with vortex generators often use larger fin pitches in the range of 3–5 mm which requires less material and therefore comprises lighter weight and is less vulnerable to frost accumulation on the fin surfaces. A typical fin-and-tube heat exchanger with punched vortex generators from the fins is shown in Fig. 1. Various vortex generators such as rectangular, delta-wing, delta winglet, and delta winglet pairs could be used to manipulate the flow by generating co- or counterrotating vortices but delta-winglet pair vortex generators are more effective to the heat transfer enhancement compared to the other types (Fiebig, 1998). Flow through a heat exchanger is complex, and there are many important length scales and geometric features without the complication of vortex generators. Flow around

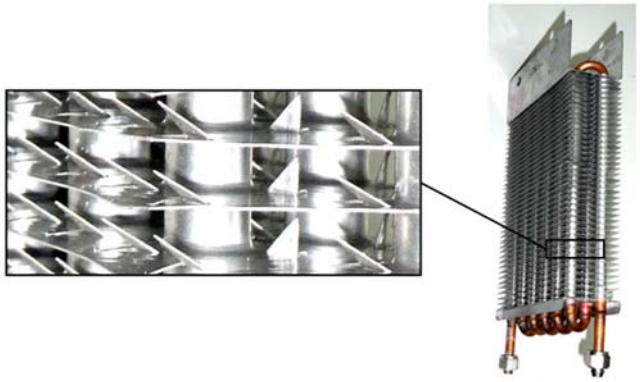

FIG. 1: A fin-and-tube heat exchanger with punched vortex generators

a tube and a tube with two different geometries of delta-winglet pair vortex generators in a channel simulating a passage between two fins of a fin-and-tube heat exchanger visualized using the dye-injection method are shown in Fig. 2. The flow structures in Fig. 2 depict longitudinal vortices and a wake flow region behind the tube.

Vortex generators can be applied in a heat exchanger by installation on the fins or punching out from the fins; but the latter case is often used due to simplicity in the manufacturing process and a smaller cost. Due to technical limitations encountered in the heat transfer coefficient measurements on the fin surface, effects of punched holes on the heat transfer measurements are usually disregarded. The presence of punched holes may affect the flow and the heat transfer. Several studies have been performed on the application of vortex generators on the heat trans-

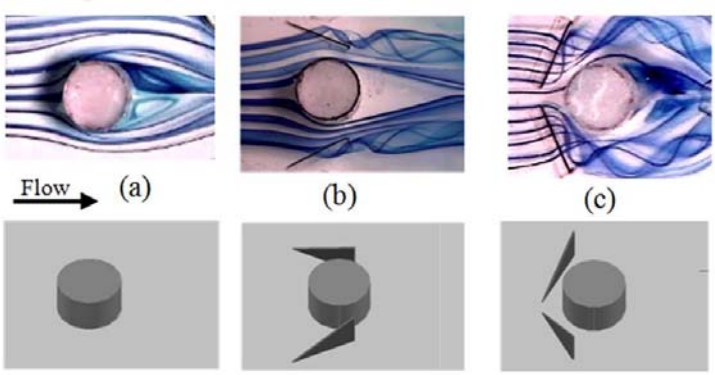

FIG. 2: Schematics and flow structure around a tube (a), and two vortex generator geometries (b) VG-I and (c) VG-II; visualized using the dye-injection method at Re = 500

fer enhancement of heat exchangers, (for instance, Febig, 1998; Mustafa et al., 2009; Biswas and Chatopadhyay, 1992), but the information on the effect of punched holes is lacking in the literature. A deeper understanding of the flow structure of a channel with multiple tube rows and vortex generators could identify the desirable features of secondary flows for heat exchanger geometries and point toward schemes for exploiting their full potential. This study employs a hydrogen bubble technique to visualize the complex flow structure within the fins with tubes and vortex generators and aims at understanding the flow behavior and effect of the holes on the vortices in order to reach a better comprehension of the convective heat transfer of a fin-and-tube heat exchanger.

2. EXPERIMENTAL METHOD AND SETUP

Hydrogen bubble visualization was carried out in a vertical closed-circuit water tunnel with a cross section of 200 mm $\times$ 70 mm. The apparatus for the hydrogen bubble technique is shown in Fig. 3. Water flow in the channel was maintained by a head difference between the water tank and the outlet of the channel. The flow was induced from the water tank through a valve and a flow meter into a settling chamber. The settling chamber was equipped with a system of flow straighteners and meshes to provide the test model with a very smooth laminar flow of uniform velocity profile. Desired flow rate was obtained by controlling the valve.

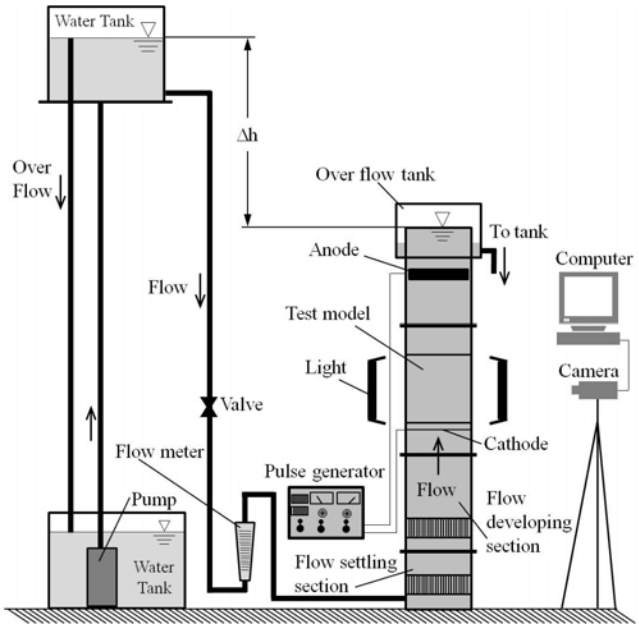

FIG. 3: Schematic of the experimental apparatus for hydrogen bubble flow visualization

Platinum-wire probes with a 50-μm diameter were used to generate time-lines of hydrogen bubbles. The platinum wires were placed upstream horizontally in the center plane of the test model (Fig. 4). A variable-voltage DC pulse generator (Sagawa MN-305) was used to create pulsed voltage for the probe wires. The pulse generator voltage was typically set to 150 V. The duration of pulse and the interval between two consecutive pulses were varied depending on the Reynolds number. A series of tests were performed with different pulse and intervals for each Reynolds number and vortex generator configurations. Then, the optimum values for the pulse duration and interval were decided to best describe the flow structures in the range of tested Reynolds numbers and vortex generator configurations. In this paper, the pulse setting for Re = 250 and Re = 500 was 100 ms for pulse duration and 200 ms for the interval between two pulses. To increase the quality and amount of hydrogen bubbles produced under a constant voltage, sodium sulfate (Na_2SO_4) 0.12 g/liter was added in the water in order to facilitate the electrolysis and thus reduce the necessary voltage. Two Neon lights (60 W each) were used to illuminate the flow field. The bubbles become visible tracers once they penetrate the illuminated zone and reflect the incident light. Visualized image of the flow field was obtained using a digital video camera. The flow Reynolds number was based on the two times of fin-pitch ($2H$ = 20 mm) and mean velocity ranged from 250 to 500.

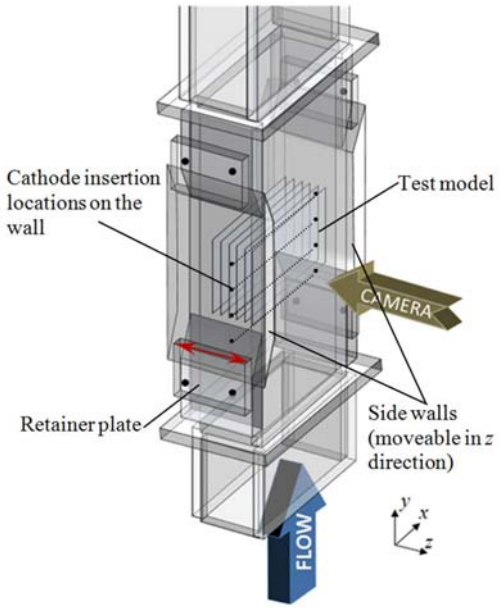

FIG. 4: Schematic of the test channel. Location of cathode probes in the region between two fins can be accurately adjusted by moving the walls on the fin normal direction and also by moving the test model in the vertical direction

2.1 Test Model and Vortex Generator Geometry

The test model is simulating a part of the gas side fin arrangement of a fin-and-tube heat exchanger. It is a two times enlarged model composed of eight successive fins each fitted with three staggered tube rows. The test model is fabricated from clear Plexiglas tubes with a 18-mm outer diameter and 0.3-mm transparent fins to permit flow visualization. Two test models with two different vortex generator configurations are made. Vortex generators are punched from the fins; but in the case of the installed vortex generators transparent sheets of 0.2-mm thick are placed behind the fins with punched vortex generators so that the effect of the punched holes is prevented. Schematic of the vortex generators is shown in Fig. 5. The vortex generators have a height-to-length aspect ratio of 0.5 with a height *H*, equal to the fin pitch. Two different vortex generator configurations ("common flow up" configuration and "common flow down" configuration) are employed which are called VG-I and VG-II hereafter, respectively.

Flow is visualized within the middle fins of the test model. Three hydrogen bubble-generating wire probes are used to visualize the flow structure, located in the *x-y* plane on the upstream of the first row (at y/H = 0), behind the first row (at y/H = 3.8), and behind the second row (at y/H = 7.6). Locations of the wires are also varied in the *z-y* plane or normal to the fin in order to visualize the flow structure near the fin surface.

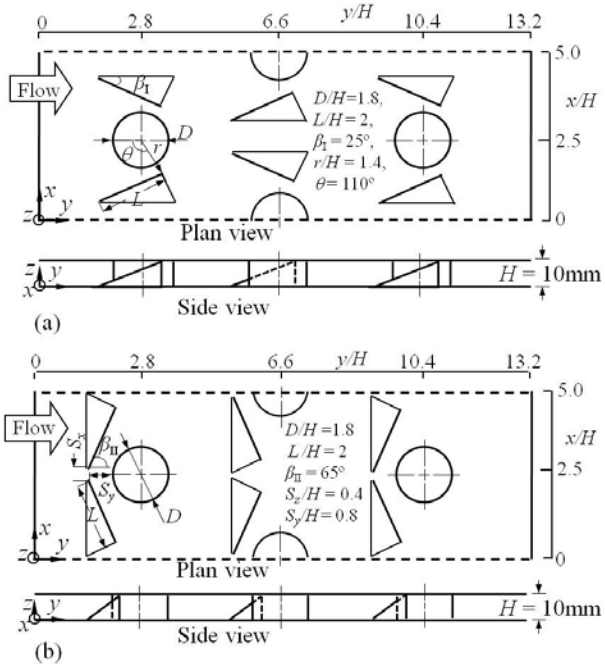

FIG. 5: Vortex generator configurations: a) VG-I and b) VG-II

3. RESULTS

Figure 6 shows flow structures of the two cases installed and punched vortex generators VG-I with the nondimensional distance of hydrogen bubble-generating wires from the fin surface z/H = 0.5 at Re = 250 and Re = 500. Variations of instantaneous velocity profiles caused by the vortex generators are clearly visible in the figures. The structures downstream of the tubes are showing low velocity profiles in the wake flow regions. As it is seen, VG-I induces the flow towards the tube walls and therefore the location of the flow separation point from the tube walls is moved downstream and the size of the wake flow regions is reduced.

An examination of Figs. 6a and 6b, at Re = 250, clearly reveals significant structural changes downstream of the punched and installed vortex generators VG-I. Velocity profiles downstream of the vortex generators show that the flow instability and mixing is higher in the installed VG-I while it is reduced in the case of the punched vortex generators. Spots "A" and "B" marked by arrows in Fig. 6 show the downwash (where the vortex induces the flow towards the wall or fin) and upwash regions (flow upwards the wall), respectively. The downwash and upwash structures, also called secondary flows, are interacting with the boundary

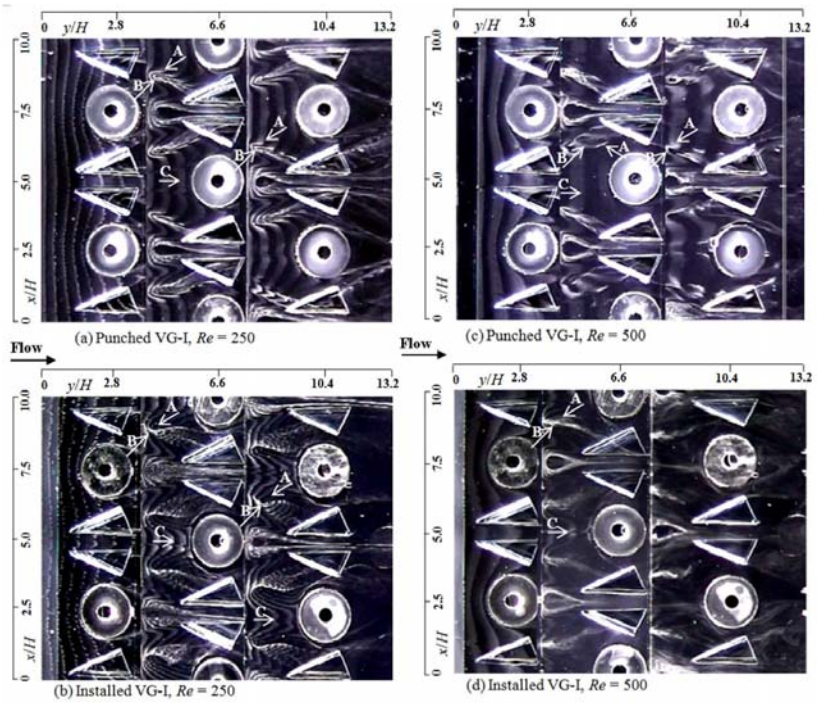

FIG. 6: Flow structures of punched vortex generators VG-I and installed vortex generators. 20 Hz hydrogen bubble-generating pulse frequency, Re = 250 and Re = 500. The distance of the wire probe from the fin is z/H = 0.5

layer near the wall and enhance heat transfer locally on the wall surface. Spot "C" shows a flat velocity profile in punched vortex generators while it has a parabolic shape in the installed vortex generators. It is seen that flow structures behind the first and second rows in VG-I are similar. With increasing the Reynolds number to Re = 500, a flow structure remains steady in the case of punched VG-I, see Fig. 6c, while vortices or upwash and downwash regions become more prominent but the velocity profile is still constant and one-dimensional in the spot "C". Figure 6d shows that with increasing the Reynolds number, the flow structure in the spots "A" and "B" becomes unsteady in the installed VG-I. It should be noted that flow through the punched holes is not visualized in Fig. 6.

Flow visualization of punched VG-I shows that the flow from the region close to the backside of the fin surface is induced through the punched holes as a consequence of a low-pressure zone in the wake of the vortex generators.

This phenomenon induced a laminar flow structure across the fins through the punched holes. Figure 7 shows the effect of the punched holes on the flow structure in VG-I and flow through the holes. The flow structure induced through the punched holes (indicated by the arrows) from the region on the backside of the fin is shown in Fig. 7a. In this case, the hydrogen bubble-generating wire is positioned at a distance of z/H = 0.85 on the backside of the fin and only the upstream wire is operated. Figure 7b shows only flow through the punched holes by painting the base fin in black color and positioning the wire beneath the fin (at z/H = 0.85). Schematic of the flow through the holes is shown in Fig. 7c.

Figure 8 shows flow structures of the two cases: installed and punched vortex generators VG-II with the nondimensional distance of hydrogen bubble-generating

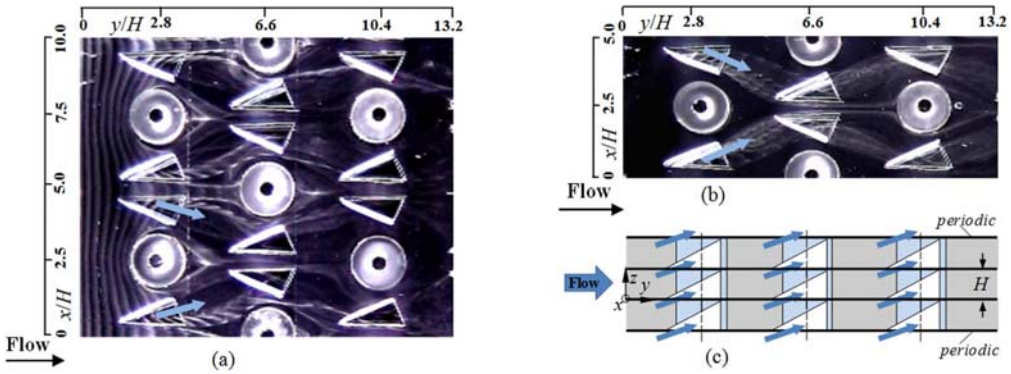

FIG. 7: Effect of punched holes on the flow structure and flow through the holes of VG-I: a) flow upstream of the first row is visualized, b) flow from the backside of the fin through the holes, c) schematic of the flow through the holes in VG-I. 20 Hz hydrogen bubble-generating pulse frequency, Re = 500. The distance of the wire probe from the fin is z/H = 0.85

wires from the fin surface at z/H = 0.5 at Re = 250 and Re = 500. Variations of instantaneous velocity profiles caused by vortex generators as well as vortex structures in downwash (spots "B") and upwash (spots "A") profiles are visible in Fig. 8. The structures downstream of the tubes are showing low velocity profiles in the tube wake flow regions. Spots "D" in Fig. 8 show that the longitudinal vortices are persisting and extending to the downstream rows. Downwash and upwash structures are created from spanwise and normal velocities which play a significant direct role in convective heat transfer. Since the downwash and upwash structures are occurring jointly, the heat transfer will be enhanced on the fin surface with vortex generators and on the fin surface opposing to the vortex generators. This behavior is reported in the heat transfer measurements of the present group of authors' (Mustafa et al., 2009). It is worth mentioning that by moving the hydrogen bubble-generating wire in the fin normal direction or near to the fin surface several vortex structures are visualized which are not shown in this paper. Flow structure and vortices are laminar downstream of the first row and gradually become unsteady in the downstream tube rows.

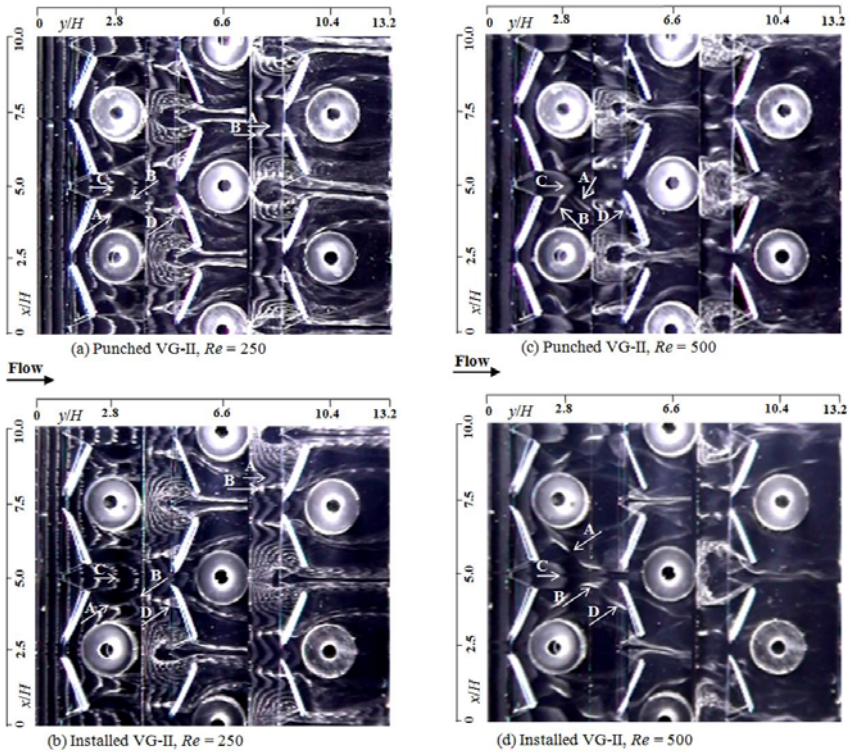

FIG. 8: Flow structures of punched vortex generators VG-II and installed vortex generators. 20 Hz hydrogen bubble-generating pulse frequency, Re = 250 and Re = 500. The distance of the wire probe from the fin is z/H = 0.5

Comparison of the velocity profiles of punched and installed vortex generators VG-II in Fig. 8 implies that the punched holes created by VG-II do not significantly change the flow structure and vortices are created in both cases. It is also observed that flow through the punched holes of VG-II is negligible and cannot affect the flow structure in the succeeding neighboring fins.

Increasing Reynolds number from Re = 250 to 500 induces more intense vortices as seen in Figs. 8c and 8d. The wake flow region behind the tubes becomes unsteady compared to the cases of Re = 250.

3.1 Friction Factor Measurements

Pressure drop measurements are performed in a horizontal wind tunnel with a cross section of 200 mm × 70 mm. The same test models used in the flow visualization experiments are placed in the wind tunnel in the upstream flow entrance. A laminar and developing flow condition is attained at the entrance of the test model. Static pressures across the test models are measured using pressure taps located on the walls of the wind tunnel. Pressures from the wall pressure taps are measured using a digital manometer (Yokogawa MT-210). Friction factors are determined from streamwise pressure gradient magnitudes. The Reynolds number is based on the mean flow and is two times of the fin pitch ($2H$ = 20 mm).

Figure 9 shows the friction factor f comparison of punched and installed vortex generators VG-I and VG-II versus the Reynolds number. As is seen, the friction factor decreases with an increase of the Reynolds number. Friction factors of VG-I

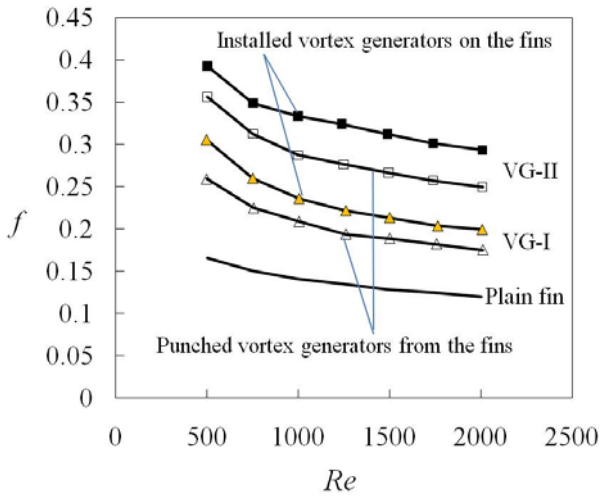

FIG. 9: Friction factor *f*, comparison of the punched vortex generators with the installed vortex generators for two vortex generator configurations VG-I and VG-II versus the Reynolds number

are lower by 29.24% and 27.29% at Re = 1000 compared to friction factors of VG-II in the installed and punched cases, respectively. Lower friction factors of VG-I mainly arise from its smaller form drag and reduction of the wake flow zone behind the tubes. Friction factors are reduced in the punched vortex generators by 11.54% in VG-I and 13.79% in VG-II compared to the installed vortex generators because the punched holes decrease the pressure difference between two sides of the vortex generators. Friction factors of the plain fin (fin-and-tube model with no vortex generators and punched holes) are shown as a reference for comparison in Fig. 9.

4. CONCLUSIONS

The flow field in a three-row fin-and-tube heat exchanger with two vortex generator configurations, namely VG-I and VG-II, taking in to account the pressure drop measurements and punched hole effects are investigated. Flow structure characteristics of two types of vortex generator configurations with punched and installed forms are elucidated and the following conclusions are attained:

1. It is revealed that using vortex generators in both punched or installed forms produces secondary flows and flow interaction with the fin surface which will enhance the heat transfer locally on the fin surface.
2. Depending on the geometry of the vortex generators the effect of the punched holes on the flow structure and on the vortices could be significant or insignificant. The flow structure of VG-I with punched holes shows a significant difference from the flow structure of the installed VG-I. Secondary flows or vortices in the installed VG-I are more intense, also accompanied with higher pressure drops compared to those of punched vortex generators but although the intensity of the secondary flow is partially decreased downstream of the vortex generators in punched VG-II, a laminar flow structure is induced across the fins through the punched holes which causes mixing of the fluid and thus disturbance to the boundary layer and gives a reduced pressure drop at the same time.

   On the contrary, effect of the punched holes on the flow structure and flow through the punched holes are not significant in VG-II.
3. Delta-winglet pair vortex generators can influence flow separation from the tube walls, flow structure, and size of the wake region behind the tubes. As is seen in the visualized flow structure of VG-I, the separation point from the tube walls was moved downstream, and the size of the wake region greatly is reduced which in turn reduces the form drag of the tubes and enhances heat transfer in the wake flow region behind the tube.
4. Pressure drop measurements showed that the vortex generators with punched holes produce smaller pressure drops compared to the installed vortex gener-

ators. Therefore, in terms of the pressure drop, punched vortex generators will give better performance.

REFERENCES

Biswas, G. and Chatopadhyay, H., Heat transfer in a channel with built-in wing-type vortex generators, *Int. J. Heat Mass Transfer*, vol. 35, pp. 803–814, 1992.

Fiebig, M., Vortice generators and heat transfer, *Trans. IChemE*, vol. 76, pp. 108–123, 1998.

Mustafa, M. A., Murata, A., Mochizuki, S., Saito, H., and Iwamoto, K. Effects of vortex generator arrangements on heat transfer enhancement over a two-row fin-and-tube type heat exchanger, *J. Enhanced Heat Transfer*, vol. 4, pp. 315–329, 2009.

Journal of Flow Visualization & Image Processing 17(4), 321–332 (2010)

NUMERICAL ANALYSIS AND FLOW VISUALIZATION OF SWIRL-TYPE MIXED CONVECTION IN A HORIZONTAL SQUARE DUCT

Koichi Ichimiya,[1] Koji Toriyama,[1] & Masakazu Kaneko[2]*

[1]*Department of Research Interdisciplinary Graduate School of Medical and Engineering, University of Yamanashi, Takeda-4, Kofu, Yamanashi 400-8511, Japan*

[2]*Mitsubishi Electric Corporation, Oshika-3, Suruga-ku, Shizuoka-shi, Shizuoka 422-8528, Japan*

[*]Address all correspondence to Koji Toriyama E-mail: toriyama@yamanashi.ac.jp

This paper describes the behavior of the swirl flow of mixed convection in a horizontal square duct (side length: L) with heated and cooled side walls. The flow behavior was visualized by the dye-injection method and numerical analysis. The working fluid was water. In the numerical analysis, the governing equations were solved using the SIMPLE procedure and QUICK scheme through the control volume. The Reynolds number Re at the inlet was 100 and the Richardson numbers Ri (= Gr/Re^2), where Gr is the Grashof number, ranged from 16 to 180. Results show that the swirl flow was activated with increase of Ri. The pitch length of the swirl flow, P, decreased with an increase of Ri, and the dimensionless pitch length, P/L, was expressed as a power function of Ri.

KEY WORDS: *swirl-type mixed convection, flow visualization, pitch length, numerical analysis, horizontal square duct*

1. INTRODUCTION

Mixed convection, comprising both forced and natural convection, is seen in small and low-velocity type heat exchangers, chemical vapor deposition, sophisticated devices and so on. The flow behavior in mixed convection is influenced by the thermal boundary conditions, the working fluids and the shape of the duct, and affects the heat transfer. Therefore, the characteristics of flow behavior in mixed convection should be examined in detail to improve the design of practical equipment. Asymmetric or one-sided heating conditions can be seen in practical equipment as thermal boundary conditions. Mixed convection in asymmetric heating has been studied numerically and experimentally by several authors. Chin et al. (1998) ex-

1065-3090/10/$35.00

NOMENCLATURE

C_p	specific heat capacity at constant pressure, J/(kg·K)	T_C	cooled wall temperature, ^{o}C, K
		T_0	inlet fluid temperature, ^{o}C, K
g	gravity, m/s^2	u, v, w	velocity components of X, Y, Z directions, m/s
Gr	Grashof number, $= g\beta L^2(T_H - T_C)/\nu^2$	u_0	average inlet fluid velocity, m/s
L	side length of the duct, m	U, V, W	dimensionless velocity components of X, Y, Z directions, $U = u/u_0$, $V = v/u_0$, $W = w/u_0$
p	pressure, Pa		
P	pitch length of the swirl flow, m		
Re	Reynolds number, $= u_0 L/\nu$	X, Y, Z	coordinates, m, mm
Ri	Richardson number, $= \mathrm{Gr}/\mathrm{Re}^2 = g\beta L(T_H - T_C)/u_0^2$	**Greek symbols**	
		β	coefficient of thermal expansion, K^{-1}
t	time, s	λ	thermal conductivity, J/(m·s·K)
T	temperature, ^{o}C, K	ν	kinetic viscosity, m^2/s
T_H	heated wall temperature, ^{o}C, K	ρ	density, kg/m^3

perimentally evaluated laminar and turbulent forced convections in a vertical rectangular duct. In the laminar regime, the local Nusselt number Nu was observed to be higher than that expected purely forced convection in both the developing region and the fully developed region. Cheng et al. (2000) examined the mixed convection in a vertical rectangular duct using a three-dimensional numerical analysis, and reported that the strength and the extension of the reverse flow were dependent on the buoyancy parameter Gr/Re, the cross-sectional aspect ratio, and Prandtl number Pr, and that the threshold value that caused reverse flow increased with the aspect ratio. Sakamoto et al. (1995) calculated the flow behavior for a horizontal square duct with heated and cooled side walls, and reported that the swirl flow was generated along the flow direction, and two recirculation flows were generated to the inside of the swirl flow in the case of a high Richardson number Ri at the cross section. Gau et al. (2000) carried out flow visualizations in a horizontal rectangular duct with uniform heat flux from a side wall, and reported that the flow behavior does not change even if the inlet Re varies at the same Ri. Kurosaki et al. (1987) calculated the flow for a horizontal rectangular duct with uniform heat flux from a side wall, and showed that Nu can be arranged by the modified Graetz number Gz. Toriyama and Ichimiya (2006) calculated flow for a horizontal square duct with heated and cooled side walls, and reported that the pitch length of the swirl flow decreased with increasing Ri. Additionally, the thermal performance with swirl flow was examined in detail. The swirl-type mixed convection in the present study is a mixed convection with swirl flow described as mentioned above. In par-

ticular, it was a flow phenomenon seen in ducts with heated and cooled side walls. However, these previous works did not perform a quantitative or detailed analysis of the behavior of a swirl flow on mixed convection.

In the present study, the behavior of a swirl flow in mixed convection in a horizontal square duct with heated and cooled side walls was investigated using flow visualization and three-dimensional numerical analysis. The pitch length of the swirl flow was examined in detail.

2. FLOW VISUALIZATION

Figure 1 shows a schematic diagram of the experimental apparatus for flow visualization. The working fluid was water. The apparatus was made of a transparent acrylic plate in order to clearly visualize the dye. The test section consisted of an adiabatic entrance section and a heat transfer section, both of which were 400 mm in length. The side length of the square duct was 20 mm. Two chambers were set up at the inlet and outlet of the test section, and the working fluid flowed into the square duct using the head difference between the inlet and outlet chambers. The fluid temperature in the reservoir tank was kept constant by means of a regulation system, and fluid was pumped up to the inlet chamber. This flow rate was regulated by a needle valve. The water that overflowed from the overflow pipe in the outlet chamber returned to the reservoir tank. The side walls of the heat transfer section were made of 10-mm-thick copper plate. To maintain the wall temperature, a duct for the constant temperature water flowing was set up along the copper

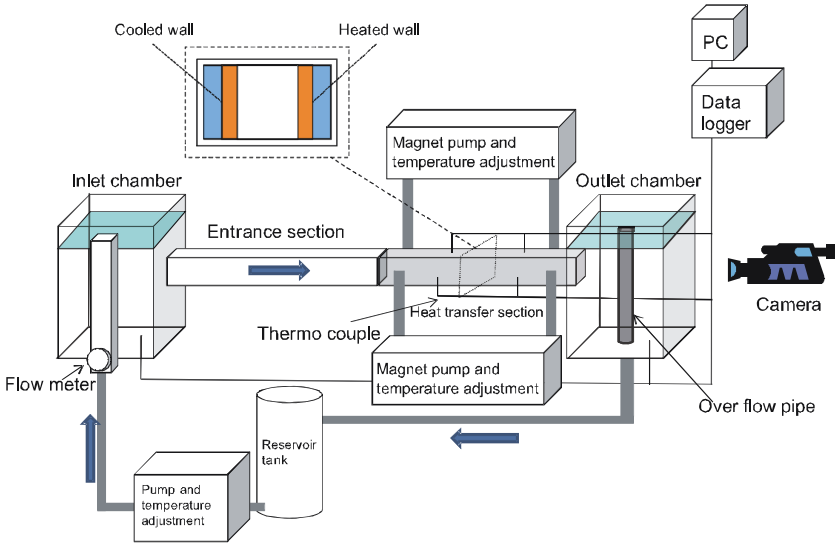

FIG. 1: Experimental apparatus

plate; its size was 20 mm × 20 mm at the cross section. The surrounding wall of the duct was made of 20-mm-thick acrylic plate. The side-wall temperatures were kept constant by flowing constant-temperature water along the copper plate. The wall temperatures were measured by K-type thermocouples placed in holes inside the copper walls. The upper and the bottom wall of the test section and the side walls of the adiabatic entrance section were made of 30-mm-thick and 50-mm-thick acrylic plates, respectively. By keeping the room and the inlet fluid temperatures the same, the upper and bottom walls of the heated section and the walls of entrance section were insulated thermally. The duct was made within an accuracy of 0.1 mm. The horizontal level of the duct was supported within 0.1^{o}.

Table 1 shows the experimental conditions. The Reynolds number Re (= $u_0 L/\nu$) at the inlet was 100 and the inlet fluid temperature was 20^{o}C, where u_0, L and ν were the average inlet velocity, the side length of the duct and the kinetic viscosity of the water at 20^{o}C, respectively. The Richardson number Ri was defined by the expression

$$\mathrm{Ri} = \frac{\mathrm{Gr}}{\mathrm{Re}^2} = \frac{gBL(T_H - T_C)}{u_0^2} \tag{1}$$

where g and β are the acceleration due to gravity and a coefficient for the thermal expansion of water at 20^{o}C, respectively. Temperature was controlled within 0.1^{o}C.

The flow behavior of mixed convection was visualized by a dye-injection method using three color dyes. The dyes were fluorescein (green), rhodamin-B (red), and mixed (orange), and their concentrations were about 10 ppm. The dyes were injected through three 1-mm-diameter pipes at the inlet of the duct. Their positions were horizontally 5 mm from the cooled side wall and vertically 5, 10, and 15 mm from the bottom wall. The result of the preliminary experiment shows that the flow behavior was visualized as a whole swirl flow when dyes were injected at this position. The experimental apparatus was installed in a dark room, and the flow behavior was visualized by illumination using a slit-type halogen lamp. The flow behaviors were photographed using a 4.13-megapixel digital camera from the downstream side.

X, *Y*, and *Z* coordinates of the flow visualization were along the flow direction, vertical axis, and horizontal axis, respectively. The origin was the bottom side of the heated wall at the starting point of the heat transfer section.

TABLE 1: Experimental conditions

T_H [^{o}C]	25	30	35
T_C [^{o}C]	15	10	5
Ri	16.25	32.30	48.44

3. NUMERICAL ANALYSIS

Figure 2 shows the Cartesian coordinate system used for this analysis. The *X*, *Y*, and *Z* axes were along the flow direction, vertical axis and horizontal axis, respectively. Their size and origin were the same as in the experiment of flow visualization. Gravity acted in the negative direction of the *Y*-axis. The governing equations in this analysis were as follows:

Continuity equation

$$\frac{\partial u_i}{\partial X_i} = 0 \tag{2}$$

Momentum equation

$$\frac{\partial u_j}{\partial t} + \frac{\partial \left(u_i u_j\right)}{\partial X_i} = -\frac{1}{\rho}\frac{\partial p}{\partial X_j} + \frac{\partial}{\partial X_i}\left(\nu \frac{\partial u_j}{\partial X_i}\right) + K_j, \tag{3}$$

where $K_1 = K_3 = 0$ and $K_2 = g\beta(T - T_0)$

Energy equation

$$\rho C_p \frac{\partial T}{\partial t} + \rho C_p \frac{\partial \left(u_i T\right)}{\partial X_i} = \frac{\partial}{\partial X_i}\left(\lambda \frac{\partial T}{\partial X_i}\right). \tag{4}$$

The Boussinesq approximation was applied to the buoyancy term in the momentum equation. These governing equations were discretized by the control volume method, and velocities, pressure and temperature distributions were obtained by the SIMPLE algorithm (Patankar, 1980). To minimize the numerical diffusion effect, the QUICK scheme (Leonard, 1980) was applied to convection terms of momentum and energy equations. The square duct was divided into 800(*X*) × 20(*Y*) ×

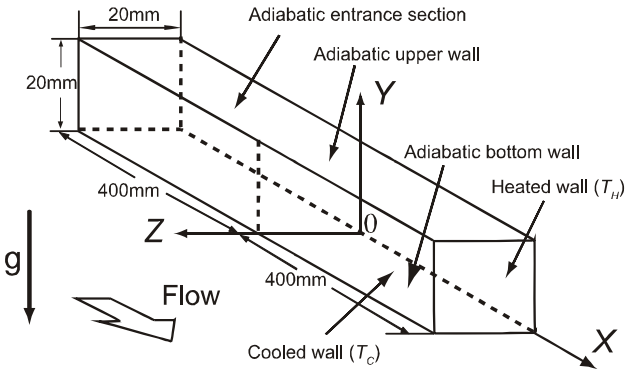

FIG. 2: Coordinate system

TABLE 2: Numerical conditions

T_H [^{o}C]	35	40	45	50	55
T_C [^{o}C]	25	20	15	10	5
Ri	36.44	72.89	109.44	145.77	182.22

20(Z) = 320,000 meshes using uniform staggered grids. Numerical analysis used the time marching method, with time steps of 0.01 s. Effects of the mesh spacing and the time step using this numerical code were previously examined by Kunugi et al. (1994), and there was no influence on the numerical results. The temperature dependence of kinematic viscosity and thermal conductivity of water was considered using a cubic interpolated equation of temperature.

Table 2 shows the numerical conditions. The inlet and initial velocities comprised a fully developed laminar profile (Shah and London, 1978) corresponding to Re = 100, which is same as the experimental condition. The inlet and initial fluid temperature was 30^{o}C. The temperatures of the heated and cooled side walls were given so that the absolute value of the temperature difference between inlet and heated or cooled side wall might become the same. The entrance section and the upper and the bottom walls of the heat transfer section were insulated thermally. At the exit, the velocity and temperature gradients along the axial direction were zero. The wall condition was assumed to be a non-slip condition. The state was approached to be steady after about 100 s. The mass between entrance and exit was balanced within 10^{-3}% and the heat balance between heating and cooling rate from the side walls and transport rate by the fluid was maintained within 0.06–1.53%. Hereafter, we discuss the steady-state solution.

4. EVALUATION METHOD OF SWIRL FLOW

The swirl flow was generated along the flow direction in the duct because the fluid was heated and cooled with the side walls. The averaged pitch of the swirl flow was used as one of the characteristics of the swirl flow. Figure 3 shows a flow model, and the blue line shows a streak line of a swirl flow. The pitch length of the swirl flow was calculated from such a three-dimensional flow model. In the flow visualization, several pictures were taken along the main flow direction from the exit of the duct. A streak line was produced by connecting the pictures at each point along the flow direction. In the numerical results, streak lines used a bird's eye view. To measure the pitch length of the swirl flow, four corners of the duct were noticed, and the lengths for one rotation of the swirl flow at each corner were measured. The subscript "i" of P_i in Fig. 3 means the order of the pitch from the starting point of the heat transfer. In the present study, the averaged pitch length of the swirl flow, P, was determined by

$$P = \frac{1}{n}\sum_{i=1}^{n} P_i \tag{5}$$

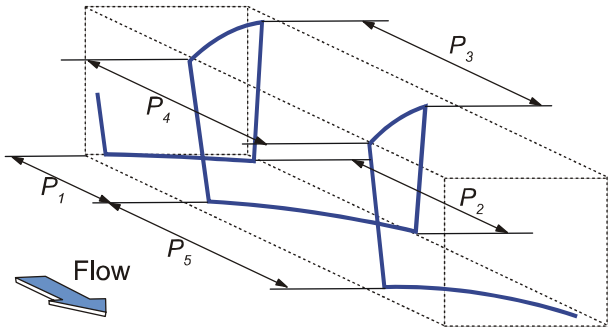

FIG. 3: Swirl model

5. RESULTS AND DISCUSSION

In the first step, flow visualization and three-dimensional streak lines at Ri = 16.15 are shown in Fig. 4. Figure 4a shows pictures of the flow visualization at a cross section from the downstream side, and Fig. 4b shows the streak lines of the swirl

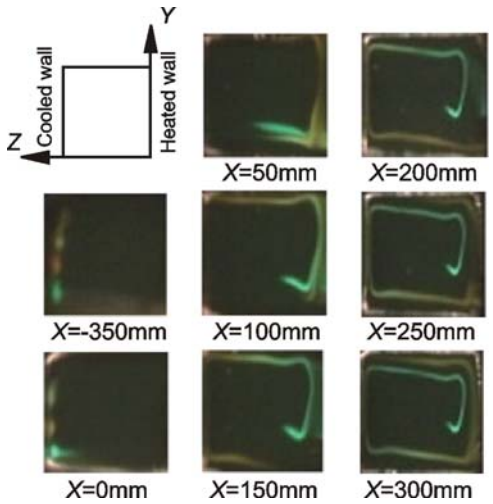

(a)

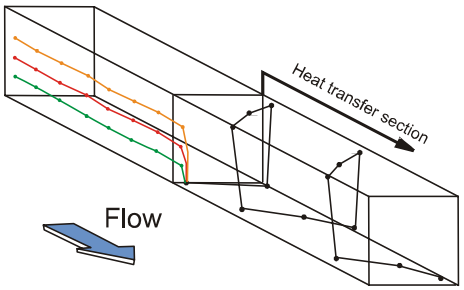

(b)

FIG. 4: Flow visualization by the dye-injection method and flow model (Ri = 16.15): (a) by dye-injection method, (b) streak line

flow made from these pictures. The left- and right-hand sides of the picture in Fig. 4a are the cooled and heated walls, respectively. In Fig. 4b, the streak line at the heat transfer section was one line because the dye positions were not clearly seen. In Fig. 4a, the flow rises up along the heated wall and falls down along the cooled wall. Therefore, the swirl is generated along the flow direction. Figure 4b represents the streak line of the swirl flow corresponding to Fig. 4a. As a result, the line rotates two times along the flow direction.

To discuss the effect of Ri, Fig. 5 shows the pictures at X = 50 and 100 mm and the three-dimensional streak line for various Ri values. Figure 5a shows pictures of flow visualization at a cross section from the downstream side, and Fig. 5b represents the streak lines of the swirl flow constructed from these pictures. In Fig. 5a, the distance at which the dye reaches the bottom wall differs for different Ri values. It depends on the temperature difference between the heated and cooled walls. In addition, this phenomenon affects the number of rotations of the streak line in Fig. 5b. That is, the pitch length of the swirl flow decreases with increasing Ri.

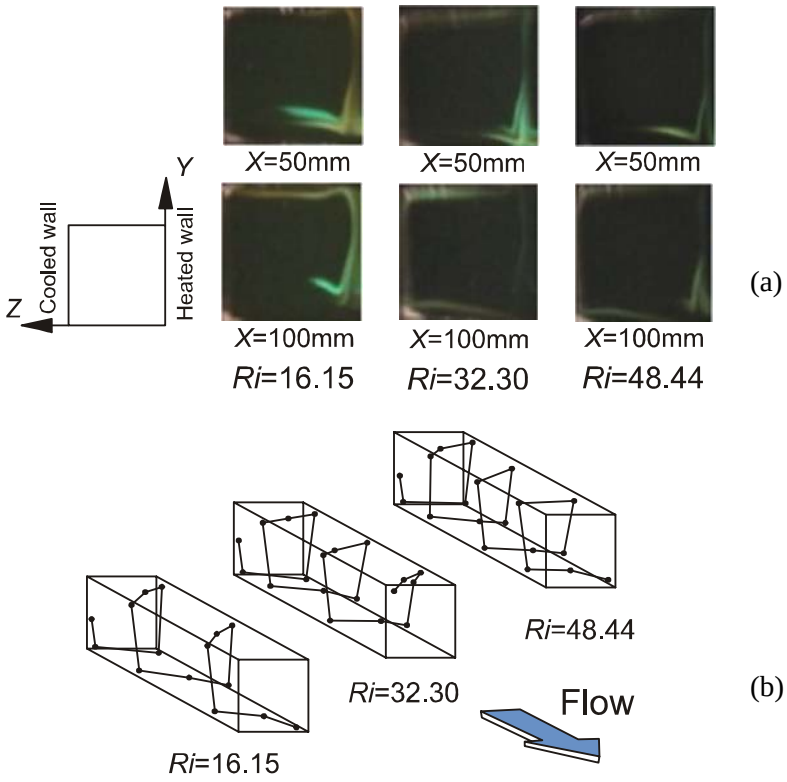

FIG. 5: Relationship between the flow pattern and Ri: (a) by the dye-injection method, (b) streak line

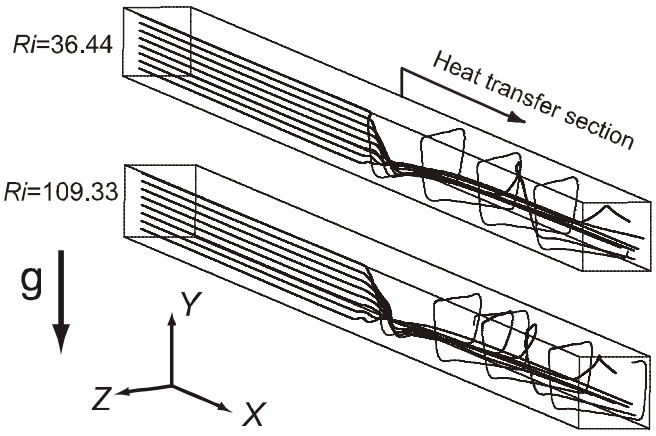

FIG. 6: Streak lines

Since the flow visualization of a swirl flow with very short pitch length was difficult, the flow behavior at high Ri was considered by numerical results. Figure 6 shows the three-dimensional streak lines for Ri = 36.44 and 109.33 by numerical analysis. The streak lines start from eight points at the entrance along the Y direction at Z = 15 mm. The lines go straight along the flow direction in the adiabatic entrance section and a swirl flow is generated along the flow direction in the heat transfer section. The line rotates three times at Ri = 36.44 and four times at Ri = 109.33. The number of rotations of the swirl flow increases with Ri. That is, the pitch length of the swirl flow decreases with increasing Ri. This is a tendency similar to the experimental result shown in Fig. 5. Moreover, the number of rotations at Ri = 36.44 is almost the mean value of the results of Ri = 32.30 and Ri = 48.44 in the experiment. It can be said this numerical analysis is appropriate for the evaluation of the pitch length of the swirl flow.

To examine the swirl flow at a cross section, Fig. 7 indicate the dimensionless velocities V and W along Y and Z directions at various positions, respectively. Dimensionless velocities V and W are defined by $V = v/u_0$ and $W = w/u_0$, where u_0 is the averaged inlet velocity. In Fig. 7a, the fluid falls down near the cooled wall and rises up near the heated wall. The absolute maximum value of V exists near the side wall. The absolute maximum value of V decreases and the absolute value of V at the center of the duct increases along the flow direction. For this reason, the fluid temperature at the center of the duct increases or decreases due to the effect of the swirl flow and thermal diffusivity of the fluid. At the more downstream side, the vertical velocity across the section is almost zero at the center of the duct. The dimensionless velocity W shows a similar tendency. In Fig. 7b, the dimensionless velocity near the wall is increased, and the dimensionless velocity at the center of the duct is decreased. Consequently, the swirl runs along close to the wall across the section.

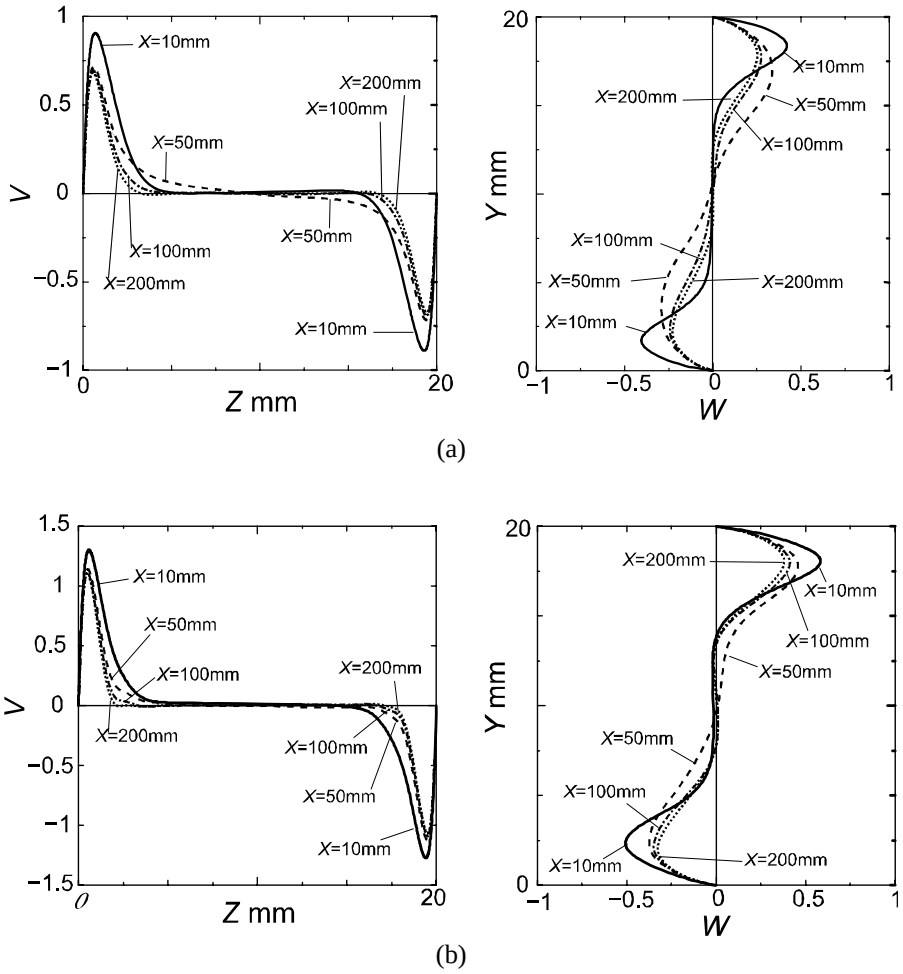

FIG. 7: Dimensionless velocities V and W at Y = 10 mm and Z = 10 mm, respectively; (a) Ri = 36.44; (b) Ri = 109.33

Figure 8 shows the local pitch length P_i at the position X for various Ri values. Experimental and numerical results are expressed by black symbols and white symbols, respectively. The local pitch length of the experimental and numerical analysis, P_i, is short near $X \approx 0$ because the driving force of the swirl flow is large due to the secondary flow in Fig. 7. On the other hand, P_i becomes short toward the down stream region because the swirl flow runs only close to the wall across section. As a result, P_i peaks at X = 50–100 mm.

Figure 9 shows the relationship between the dimensionless averaged pitch P/L and Ri in logarithmic scale. Experimental and numerical results are expressed by solid circles and white circles, respectively. The dimensionless pitch length decreases linearly with increasing Ri. It is expressed as a power function by Eq. (6)

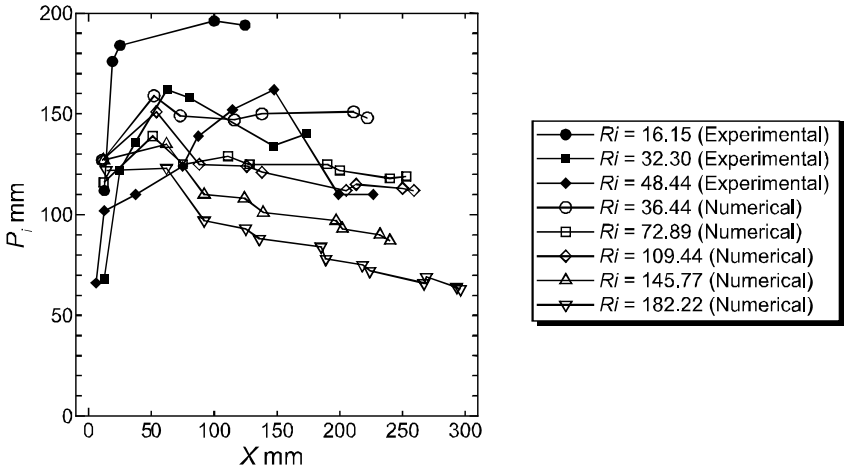

FIG. 8: Pitch length along the flow direction

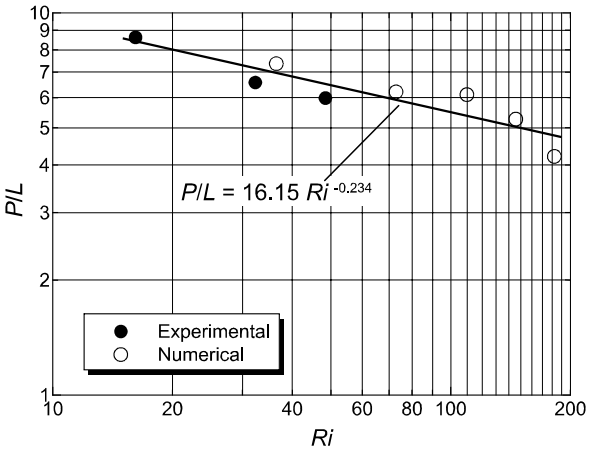

FIG. 9: Relationship between Ri and *P*/*L*

$$P/L = 16.15\, Ri^{-0.234} \tag{6}$$

The accuracy is within ±15% and the allowable range is 16 ≤ Ri ≤ 185.

6. CONCLUSIONS

The swirl flow characteristics of mixed convection in a horizontal square duct with heated and cooled side walls were evaluated by flow visualization and numerical analysis. The conclusions were as follows:

(1) Generally a swirl flow moves along the walls, and the values of the vertical and the horizontal velocities near the center of the duct at a cross section becomes almost zero in the downstream region.
(2) The pitch length of the swirl flow changes along the flow direction, and decreases after increasing once toward the downstream region.
(3) The average pitch of the swirl flow decreases with increasing Ri.
(4) The dimensionless averaged pitch P/L decreases with increasing Ri and is expressed as a power function of Ri. The accuracy of this equation is within ±15% in this analysis.

REFERENCES

Cheng, C. H., Wang, C. J., and Aung, W., Buoyancy-assisted flow reversal and convective heat transfer in entrance region of a vertical rectangular duct, *Int. J. Heat Fluid Flow*, vol. 21, pp. 403–411, 2000.

Chin, Y. D., Hollingsworth, K. D., and Witte, L. C., A study of convection in an asymmetrically heated duct using liquid crystal thermography, *ASME HTD*, vol. 357, no. 2, pp. 63–70, 1998.

Gau, C., Jeng, Y. C., and Lin, C. G., An experimental study on mixed convection in a horizontal rectangular channel heated from a side, *Trans. ASME, J. Heat Transfer*, vol. 122, pp. 701–707, 2000.

Kunugi, T., Ichimiya, K., and Sakamoto, Y., Numerical analysis of mixed convective heat transfer in a square channel with uniform wall temperature, *Trans. JSME B*, vol. 60, no. 572, pp. 1393–1400, 1994.

Kurosaki, Y. and Satoh, I., Laminar heat transfer in an asymmetrically heated rectangular duct, *Int. J. Heat Mass Transfer*, vol. 30, no. 6, pp. 1201–1208, 1987.

Leonard, B. P., *Computer Method in Fluid*, Plymouth: Pentech Press, pp. 159–195, 1980.

Patankar, S. V., *Numerical Heat Transfer and Fluid Flow*, New York: Hemisphere Publishing Corporation, pp. 11–150, 1980.

Sakamoto, Y., Kunugi, T., and Ichimiya, K., Three-dimensional numerical analysis of mixed convective heat transfer in a horizontal square channel with heated and cooled side walls, *Trans. JSME B*, vol. 61, no 586, pp. 2220–2234, 1995.

Shah, R. K. and London, A. L., *Laminar Flow Forced Convection in Ducts, Advances in Heat Transfer*, London: Academic Press, p. 197, 1978.

Toriyama, K. and Ichimiya, K., Effect of heated and cooled wall temperature on swirl-type mixed convection heat transfer in a horizontal square duct, *Trans. JSME B*, vol. 72, no. 714, pp. 397–403, 2006.

Journal of Flow Visualization & Image Processing 17(4), 333–346 (2010)

FLOW BEHAVIOR IN A PARALLEL-TUBE HEAT TRANSPORT DEVICE ANALYZED BY USING IMAGE PROCESSING

Thanh-Long Phan, [*] ***Akira Murata, Sadanari Mochizuki, Kaoru Iwamoto, & Hiroshi Saito***

Department of Mechanical Systems Engineering, Tokyo University of Agriculture and Technology, Koganei-shi, Tokyo 184-8588, JAPAN

[*]Address all correspondence to Thanh-Long PHAN E-mail: 50008833208@st.tuat.ac.jp

Fluid flow behavior and heat transport rate of Parallel-Tube Heat Transport Devices (PT-HTD) were experimentally investigated using water as a working fluid. In the present PT-HTD, evaporator and condenser chambers were connected through five parallel glass tubes of the same inner diameter. The PT-HTD was vertically set and the bottom evaporator and top condenser were heated and cooled, respectively. The entrainment limit of PT-HTD was observed that may mainly be affected by a small tube diameter. However, the heat-transport rate of PT-HTD is independent of the tube diameter. The unsteady flow behavior was always observed in PT-HTD. The number of tubes in which upward flow occurred increased when the heat-transport rate of PT-HTD increased.

KEY WORDS: *heat transport device, phase change, two-phase flow, boiling, flow visualization, image processing*

1. INTRODUCTION

Recently, heat flux generated by electronic components has been increasing with continuing decrease in their size. Heat transport devices are used to remove heat from those electronic components. Heat dissipation of the next-generation electronic components will certainly exceed capability of existing heat transport devices such as conventional heat pipes (Grover et al., 1964) or thermosyphons (also called gravity-assisted heat pipes) (Stauder and McDonald, 1986; Khodabanden and Palm, 2002; Lee and Mital, 1972). Therefore, there is a need for more compact and efficient heat transport devices.

Boiling and condensation are very important in heat transfer processes as they are generally associated with high heat-transfer rate. According to the increase in heat dissipation for electronic components, there has been an increased interest in electronic-device cooling using heat transfer with boiling and condensation.

NOMENCLATURE

c_p	specific heat, J/kg·K	ρ	density, kg/m^3
P	pressure, kPa		
$\dot{Q}$	heat-transport rate, W	**Subscripts**	
T	temperature, ^{o}C	w	water
V	velocity, m/s	in	inlet
$\dot{V}$	volumetric water flow rate, m^3/s	out	outlet
Greek symbols		ev	evaporator
ΔP	pressure difference, kPa	co	condenser

This paper presents the flow visualization and heat transfer results of a Parallel-Tube Heat Transport Device (PT-HTD) that utilizes heat transfer with boiling and condensation. It consists of parallel tubes with headers on both ends. The mechanism of the fluid flow in the PT-HTD is different from that of the conventional ones like thermosyphons and heat pipes. Unlike heat pipes, PT-HTD does not use a wick structure to enforce condensate liquid return to evaporator, PT-HTD uses conventional parallel tubes to enable reciprocating motion of liquid and vapor inside the device.

The performance of PT-HTD is affected by many parameters. Onishi et al. (2005) studied the effect of a number of parallel tubes on heat-transport rate of PT-HTD. They tested three PT-HTDs with 3, 6, and 12 parallel tubes. Their devices were constructed with copper capillary tubing for both headers and parallel tubes. Their results showed that the heat-transport rate did not increase linearly with an increase in the number of parallel tubes. In another research, Onishi et al. (2004) tested PT-HTDs, which had six parallel tubes and different tube diameters of 0.51, 1, and 2 mm. They found that the heat-transport rate of the 1- and 2-mm cases was almost the same. However, for PT-HTD with 0.51 mm, when the temperature difference of the evaporator and condenser reached a certain value the heat-transport rate became saturated. They claimed that an inner diameter had significant influence on heat-transport rate of PT-HTD when it is small. Cirtog et al. (2007) tested PT-HTDs with two different diameters (3.5 mm and 6.5 mm) to enforce unidirectional circulation of the working fluid. They argued that the high heat-transport rate was archived because of the establishment of one-way recirculation flow of working fluid. However, the reason for achievement of a high heat-transport rate in one-way recirculation flow of working fluid was not shown in their study. The flow behavior in PT-HTD is complex and it is affected by a number of parameters. The fluid flow inside PT-HTD is related closely to heat-transport rate. However, the real mechanism of fluid flow occurring inside PT-HTD is not well understood.

The objective of the present study is to examine the effect of tube diameters on the flow behavior and the heat-transport rate of PT-HTD. Three different tube diameters have been employed in this study.

2. EXPERIMENTAL SETUP AND PROCEDURE

The schematic of a PT-HTD is shown in Fig. 1 and the principal parameters of the device are listed in Table 1. The core of the device consisted of an evaporator and a condenser, which were connected by five parallel glass tubes. The device was vertically set with the condenser and the evaporator on top and bottom locations, respectively. The evaporator and condenser were rectangular brass chambers. The test core was designed to show the phenomenon inside the PT-HTD by using the transparent glass, which allowed the direct observation of fluid flow in tubes, bubble generation in the evaporator and condenser.

Two ceramic heaters (Sakaguchi MS-2, 25 mm × 50 mm) attached on the backside of the evaporator were used as the heat source. Electric power to the heater was supplied from a Variac (0–300 V) connected in series to a multimeter (Keithley 2000) measuring the current. The voltage across the heater was measured by another multimeter (Keithley 2010). The heat input was evaluated by measuring the voltage and current. A cooling path of water was installed on the backside of the condenser. The water flow rate was measured by using a rotameter. The tem-

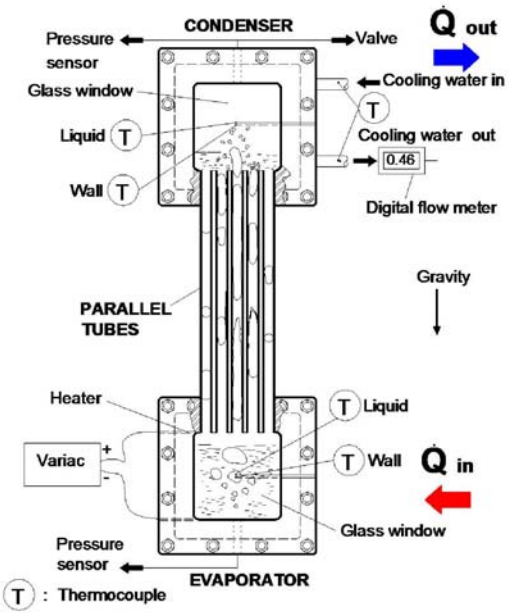

FIG. 1: Schematic of a parallel-tube heat transport device

TABLE 1: Specification of PT-HTD

Headers	Length.Width.Depth	$50 \times 50 \times 1$ mm^3
	Material	Brass
Parallel tubes	Length	200 mm
	Inner diameter	3.6, 2.6, 1.6 mm
	Material	Glass
Working fluid	Material	Pure water
	Filling ratio	50%

perature rise of cooling water was measured by two T-type thermocouples. Four sheath-type thermocouples (0.25 mm O.D.) were used for measuring the temperature of the liquid and the walls of the evaporator and condenser. The pressure in the evaporator and condenser was measured by two high-precision pressure sensors (Keyence PV-10S, ±100 kPa, resolution 0.1 kPa).

Purified water was used as the working fluid. After it was evacuated to 0.26 kPa, the test core was charged with water up to 50% of the inner volume. After charging water, the test core was evacuated again to pressure of 2 kPa, and then the measurements were started.

The experiments were conducted by changing stepwise heat input and then the operating parameters were recorded after the new steady state of system was attained. As soon as the wall temperature of the evaporator reached about 80^{o}C, that was close to a critical temperature of electronic components (CPU, 2009), the power supply to ceramic heaters was switched off.

The fluid flows in the evaporator, the condenser, and the parallel tubes were recorded simultaneously at the rate of 1000 frames per second using a high-speed camera (Photron, Fastcam-512 PCI) with support of a mirror system. The temperature and pressure data were fed to a data acquisition system and were analyzed by using LabVIEW software. The heat-transport rate, $\dot{Q}$, of PT-HTD was evaluated by water temperature and water flow rate.

$$\dot{Q} = \rho c_p \dot{V}(T_{w,out} - T_{w,in}) \tag{1}$$

where $T_{w,in}$, $T_{w,out}$, and $\dot{V}$ are the condenser inlet and outlet temperatures and the volume flow rate of the cooling water, respectively. The PT-HTDs of three different inner tube diameters, which were 1.6, 2.6, and 3.6 mm, were tested (all of 200-mm length).

Uncertainty analysis in the present study is based on the test uncertainty (ASME, 1998). The heat-transport rate of PT-HTD was calculated by measuring the volume flow rate and temperature difference of cooling water through the condenser. The cooling water volume flow rate was selected at 460 ml/min (±20 ml) during the experiment. The uncertainty of cooling water temperature measurement was less

than 1.5°C. The uncertainty of the heat-transport rate ($\dot{Q}$) was calculated to be 9.4% (with 95% confidence).

3. VELOCITY ESTIMATION USING IMAGE PROCESSING

In order to attempt a quantitative description of fluid flow inside parallel tubes, an image-processing program was used to estimate velocity of the liquid–vapor interface. The flow velocity estimation was based on the evaluation of liquid–vapor interface shift of two consecutive frames (see Fig. 2) which is expressed by the following equation:

$$V_{\text{bubble}} = \frac{\delta}{t_{\text{frame}}} \, . \tag{2}$$

The algorithm often used in particle image velocimetry is outlined in Fig. 3. Prior to the fast Fourier transformations (FFT) of the images, the background obtained as the averaged field of at least 100 frames was removed by evaluating the absolute difference between the analyzed frames and the background. After FFT, the complex conjugate of the second frame was obtained. By multiplication of the FFT of the first frame and the complex conjugate of the FFT of the second frame, the relative interface shift of the Fourier components was obtained. After inverse FFT of the result, a peak indicated the dominant two-dimensional interface shift between the two frames in the space domain. The exact position of the peak was identified from quadratic interpolation near the maximum in order to obtain subpixel accuracy. Alternatively, various morphological transforms were applied prior to the FFT in order to test the sensitivity of the method on the remaining noise after background removal. Although accuracy of the method was difficult to obtain, the results were found very reasonable, with little dependence on the selected

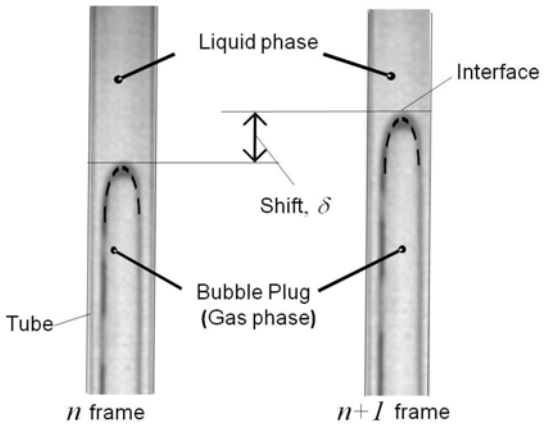

FIG. 2: Principal of computing velocity

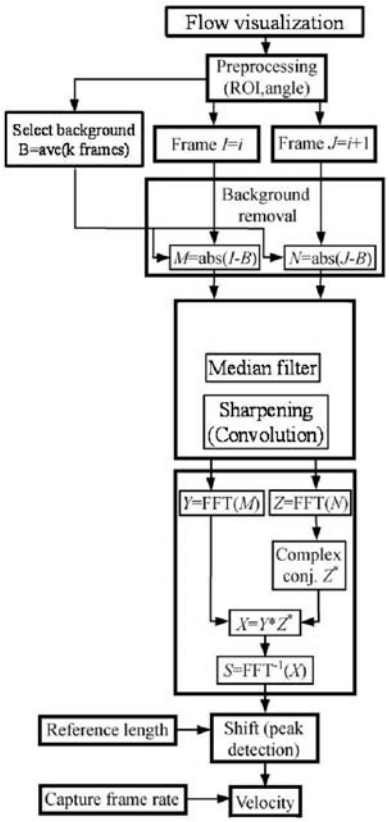

FIG. 3: Velocity measurement algorithm

region of interest and noise. For the present study, the image quality was 512 pixel × 512 pixel, and the length of the region of interest was selected at 120 mm, then the uncertainty of bubble velocity (V_{bubble}) was calculated to be 1% for all evaluations. However, problems could appear for a very high velocity for which the capture speed was not sufficient, and for the period in which no distinguishable features were present in the analyzed region. These problems will need to be solved in the next improvement.

4. RESULTS AND DISCUSSION

4.1 Heat-Transport Rate

As seen in Fig. 4, heat-transport rate increases almost linearly with an increase in temperature of the evaporator wall, T_{ev}. However, when T_{ev} reaches a certain value, the heat-transport rate of the 1.6-mm and 2.6-mm cases becomes saturated. Under those conditions, the working fluid started to accumulate in the condenser,

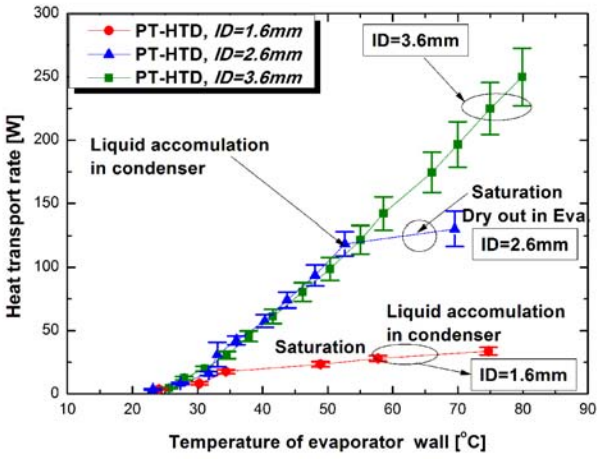

FIG. 4: Heat transport rate vs. temperature of the evaporator wall

this led to dry-out in the evaporator. These phenomena are somewhat similar to the entrainment limit (or the so-called flooding limit) of a two-phase closed thermosyphon (Faghri, 1995). Only a PT-HTD using a lager tube diameter (case of 3.6 mm) successfully operated in the present study. Therefore, the inner tube diameter may be a major factor for entrainment limit of PT-HTD.

In the two-phase closed thermosyphon, the entrainment limit was due to the vapor–liquid film countercurrent flow in the same tube (El-Genk and Saber, 1997; Noie, 2005), that was not observed in PT-HTD because it has multiple parallel tubes. The reason for the entrainment operation limit occurrence in PT-HTD (1.6-mm, 2.6-mm cases) can be explained by the confinement characteristics of a small tube. It also should be noted that the common tube diameter used in a two-phase closed thermosyphon (Lee and Mital, 1972; El-Genk and Saber, 1997; Noie, 2005) was much larger than that in the present study.

In Fig. 4, one can see that the PT-HTD shows a narrower operation range for a smaller inner diameter. It is interesting that the heat-transport rates of three different diameter cases were almost identical till the dry-out point. The similarity of heat-transport rates of PT-HTDs may be explained by the fact that the total heat-transport rate of PT-HTD was dominated by latent heat of vaporization, which is mostly independent of the core geometry.

4.2 Fluid Flow Behavior

Figure 5 shows two-phase flow patterns in parallel tubes after the moment of boiling onset that enables the fluid flow oscillation in parallel tubes. It is easy to observe confined bubbles and a slim liquid film of the vapor plug in parallel tubes of the 1.6- and 2.6-mm cases (shown in Fig. 5a,b). Moreover, the interface between the liquid and vapor plug is well formed in a semi-circular inner tube. This

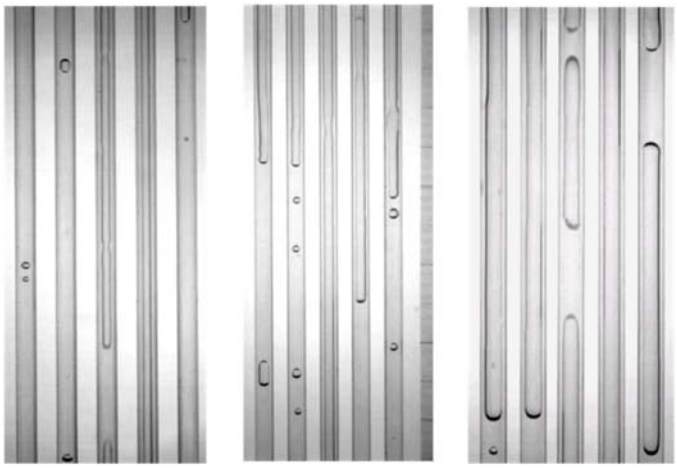

FIG. 5: Flow patterns observed in 1.6-mm, 2.6-mm, and 3.6-mm tube diameter at boiling onset

shows that the surface tension was dominated (Chen et al., 2006) that may restrict the liquid return to the evaporator, and eventual burnout phenomena in evaporator occurred. In contrast to the flow patterns of 1.6-mm and 2.6-mm tube diameter, no confined bubbles and the chaotic interface between liquid and vapor were observed in the 3.6-mm tube diameter case.

The flow visualization results (movies) of PT-HTD showed that the phenomena are complex. The motion of the vapor and liquid upward/downward flow in PT-HTD is based on generation, expansion of vapor which depend on the evaporator temperature, the unsteady flow behavior was always observed in PT-HTD. Table 2 is a summary of the fluid flow behavior in PT-HTD (3.6-mm I.D. case). Figure 6 shows a representative movie frame of the flow behavior in PT-HTD (3.6-mm I.D. case) at different heat transport rates of 25 W, 115 W, and 250 W. At a low heat transport rate, when the temperature of the evaporator wall is sufficient for boiling onset (see Fig. 6a), most of the working liquid is stored in the evaporator. There

TABLE 2: Summary of fluid flow behavior in the 3.6-mm I.D. case

$\dot{Q}$ (W)	25 W	61 W	115 W	250 W
Number of tubes with upward flow	1 tubes Intermittent slug flow	2 tubes Slug flow	3 tubes Slug-churn	4 tubes Annular flow
Number of tubes with downward flow	4 tubes Oscilating slug flow	3 tubes Slug flow	2 tubes Bubbly flow	1 tubes Liquid flow

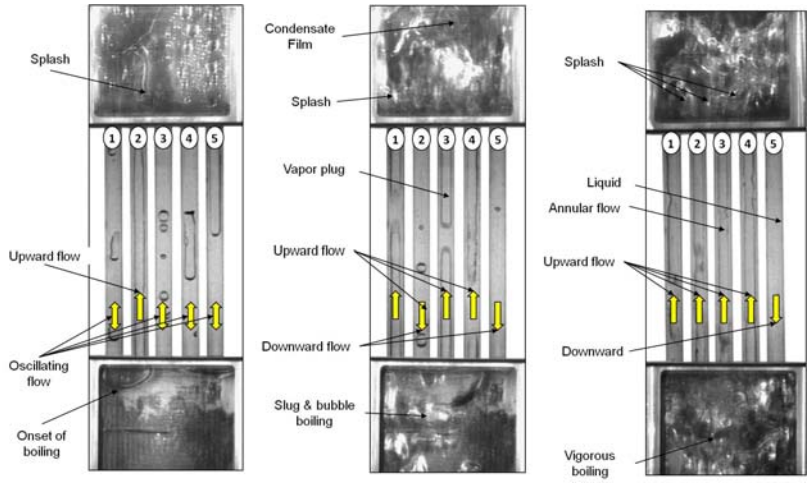

(a) (b) (c)

FIG. 6: Capture of the flow behavior at various heat transport rates of the 3.6-mm case

is a tube which shows an upward vapor–liquid slug flow. The fluid in other tubes has a low frequency of oscillations (the movie in Fig. 6a).

With an increase of the heat transport rate, the slug and nucleate boiling regime is observed in the evaporator (Fig. 6b). There are two or three tubes in which upward churn flow occurs. The condensate returns in bubbly flow through the remaining tubes (the movie in Fig. 6b).

As the heat transport rate is further increased, the film boiling regime is observed in the evaporator (Fig. 6c). The upward flow is changed into an annular flow in four tubes, while the only one tube carries stable downward flow in the liquid phase (see Fig. 6c).

Flow visualization results showed that there were two types of circulation flow in PT-HTD. One is an intermittent upward vapor flow in a tube with random oscillating flow in other tubes for a low heat-transport rate. The other is a recirculating flow with upward flows in two or up to four tubes and stable downward condensate flows in other tubes.

4.3 Pressure Behavior

Figure 7 shows the variation of an average pressure in the evaporator and condenser with temperature of the evaporator wall. The saturation pressure curve is also indicated in the figure. It is confirmed that the general trend of both Pev and P_{co} agreed fairly well with the corresponding saturation curve. One can observe that the measured evaporator pressure is always higher than the condenser pressure. However, the pressure in both evaporator and condenser is always fluctuating in a certain range.

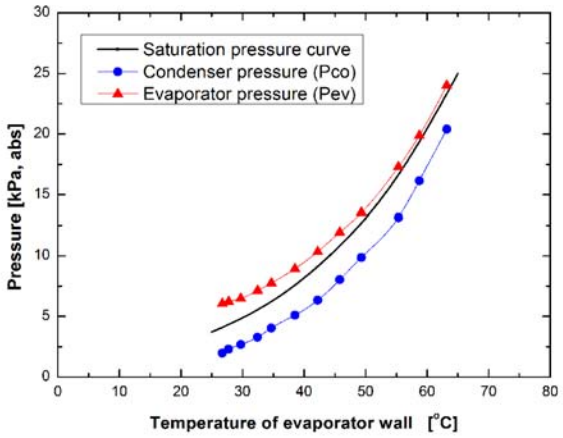

FIG. 7: Variation of average pressure in the evaporator and condenser with temperature of the evaporator wall

Figures 8 and 9 show typical variation of evaporator and condenser pressures and the pressure difference in 100 s at the steady state of a low heat transport rate ($\dot{Q}$ = 25 W) and a high heat transport rate ($\dot{Q}$ = 250 W). As seen in the figures, both P_{co} and P_{ev} oscillate and the pressure difference (ΔP) also oscillates. The above observations, the existence of fluctuation of the pressure difference between the evaporator and condenser is a reason to allow for working fluid recirculation inside the PT-HTD.

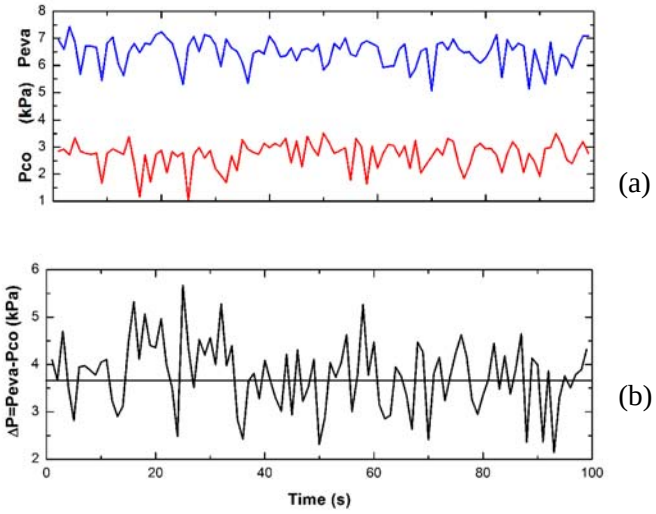

FIG. 8: Variation of evaporator and condenser pressure (a) and their difference (b) for $\dot{Q}$ = 25 W

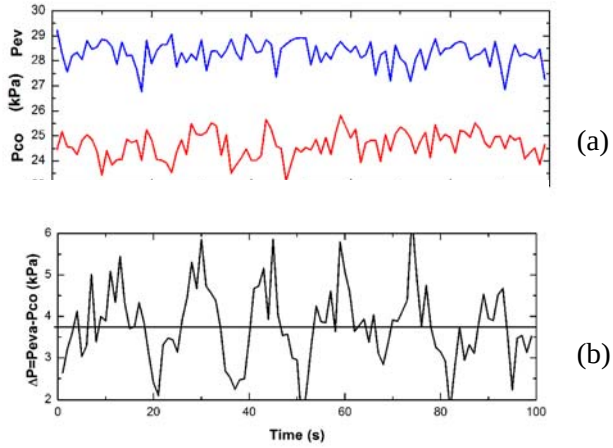

FIG. 9: Variation of evaporator and condenser pressure (a) and their difference (b) for $\dot{Q}$ = 250 W

4.4 Quantitative Description of Fluid Flow inside Parallel Tubes

The two-phase flow velocity in the middle of parallel tubes (Fig. 5) was calculated by using an image-processing program. Figure 10 depicts temporal variation of liquid–vapor interface velocity for tubes simultaneously at a heat-transport rate of 25 W. A negative velocity corresponds to downward flow and a positive velocity corresponds to upward flow. As seen in Fig. 10, upward flow occurs one time in tube 4, the abrupt velocity in tube 4 represents the moment when the liquid–vapor interface reaches the condenser then no interface trace was found. The fluctuating flow occurs in other tubes. For example, upward and downward flows can be seen in tube 5. On the other hand, at a higher heat-transport rate (see Fig. 11, $\dot{Q}$ = 115 W), there are three tubes (tubes 1, 3, and 4) in which upward flow occurs. Tubes 2 and 5 carry returning liquid to the evaporator. In Fig. 12 ($\dot{Q}$ = 250 W), there are four tubes in which upward flow occurs at a higher velocity. Only tube 5 carries returning single-phase liquid at a higher velocity compared with those of downward flow velocity at $\dot{Q}$ = 115 W (see Fig. 11).

The most distinct change of velocity from a low heat-transport rate (see Fig. 10) to a high heat-transport rate (see Fig. 12) is the frequent appearance of upward flow. Much more liquid–vapor interfaces were observed at a high heat-transport rate (Fig. 12, = 250 W) compared with those at a low heat-transport rate (Fig. 10, = 25 W). This corresponds to more frequent and more intense of vapor generation upward at a high heat-transport rate at a low heat transport rate. In addition, the liquid condensate flows downward at higher velocity, which indicates the establishment of the steady circulatory motion. This establishment of steady recirculation is probably one of the conditions for superior operation of PT-HTD in higher heat transport mode.

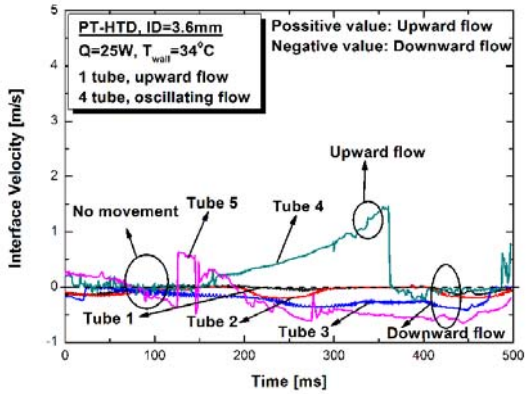

FIG. 10: Temporal variation of vapor–liquid interface velocity for $\dot{Q}$ = 25 W, 3.6-mm I.D

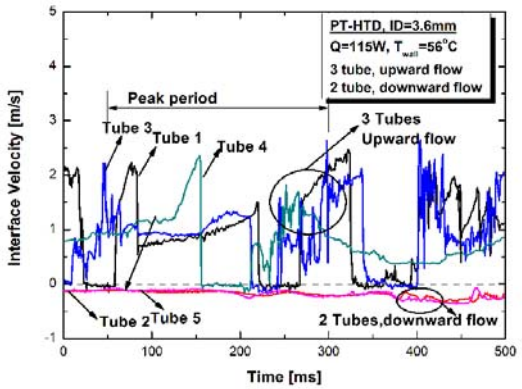

FIG. 11: Temporal variation of vapor–liquid interface velocity for $\dot{Q}$ = 115 W, 3.6-mm I.D

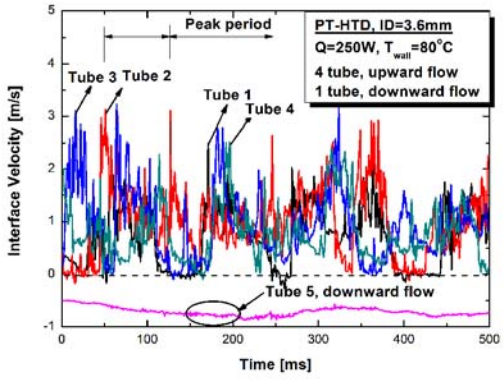

FIG. 12: Temporal variation of vapor–liquid interface velocity for $\dot{Q}$ = 250 W, 3.6-mm I.D

5. CONCLUSIONS

Flow behavior and heat-transport rate of a Parallel-Tube Heat Transport Device were studied, and the following conclusions were drawn:

1) The unsteady flow behavior was always observed in PT-HTD. Two types of circulation flow in PT-HTD were observed. For a low heat-transport rate, the flow behavior is characterized by intermittent flow and random oscillation. For a high heat-transport rate, the flow behavior is characterized by upward flow and stable downward flow.
2) The entrainment limit of PT-HTD was found to depend on the inner tube diameter of parallel tubes, that is because of the confinement characteristics of a small tube diameter. The effect of the tube diameter on the heat-transport rate was nearly negligible in the present tube diameter range (I.D. = 1.6–3.6 mm).
3) The fluctuation of pressure existed in the evaporator and condenser which is considered to be a reason to allow the recirculation of working fluid inside the PT-HTD.
4) The number of tubes in which upward flow occurred increased when the heat-transport rate of PT-HTD increased. The tendency to establish more steady recirculating flow in higher heat transport mode was confirmed.

ACKNOWLEDGMENTS

The authors wish to express their gratitude to Mr. T. Yamamoto of Tokyo University of A & T for his assistance in developing the image-processing program. In addition, the authors would like to thank to Dr. A. P. Cirtog for her contribution to the work on this paper.

REFERENCES

ASME 19.1-1998, Test Uncertainty, 1998.

Chen, L., Tian, Y. S., and Karayiannis, T. G., The effect of tube diameter on vertical two-phase flow, *Int. J. Heat Mass Transfer*, vol. 49, pp. 4220–4230, 2006.

Cirtog, A. P., Mochizuki, S., Murata, A., and Ionel, I., Heat transport device with phase change using two parallel tubes, *Thermal Sci. Eng.*, vol. 15, no. 4 (short note), pp. 241–244, 2007.

CPU Maximum temperature, Retrieved December 15, 2009 from: http://www.pantherproducts.co.uk /Articles /CPU/CPU%20Temperatures.shtml

El-Genk, M. S. and Saber, H., Flooding limit in closed two-phase flow thermosyphons, *Int. J. Heat Mass Transfer*, vol. 40, no. 9, pp. 2147–2164, 1997.

Faghri, A., *Heat Pipe Science and Technology*, New York: Taylor and Francis, pp. 341-440, 1995.

Grover, G. M., Cotter, T. P., and Erickson, G. F., Structures of very high thermal conductance, *J. Appl. Physics*, vol. 35, pp. 1990–1991, 1964.

Khodabandeh, R. and Palm, B., Influence of system pressure on the boiling heat transfer coefficient in a closed two-phase thermosyphon loop, *Int. J. Thermal Sci.*, vol. 41, pp. 619–624, 2002.

Lee, Y. and Mital, U., A two-phase closed thermosyphon, *Int. J. Heat Mass Transfer*, vol. 15, no. 9, pp. 1695–1707, 1972.

Noie, S. H., Heat transfer characteristics of a two-phase closed thermosyphon, *Appl. Thermal Eng*., vol. 25, no. 4, pp. 495–506, 2005.

Onishi, T., Kanatsugu, T., Mochizuki, S., and Murata, A., Flow phenomena in parallel tube heat-transport device with phase change, *Proc. 5th Pacific Symp. on Flow Visualization and Image Processing*, PSFVIP-5-243, 2005.

Onishi,T., Mochizuki, S., and Murata, A., Heat transport device consisting of capillary tubes with boiling driven heat transfer mechanism inside, *Proc. 1st Int. Symp. on Micro & Nano Technology (ISMNT-1)*, C-04, 2004.

Stauder, F. A. and McDonald, T. W., Study of a two-phase thermosyphon-loop heat exchanger, *ASHRAE Trans*., vol. 92, no. 2A, pp. 486–496, 1986.

Journal of Flow Visualization & Image Processing 17(4), 347–358 (2010)

SIMULATION AND VISUALIZATION OF FLOCK PARTICLES ON A GLOVE SURFACE IN A TWO-PHASE FLOW

Piyawut Kaewrit & Chawalit Kittichaikarn[*]

Department of Mechanical Engineering, Faculty of Engineering, Kasetsart University, 50 Phaholyotin Rd., Jatujak, Bangkok 10900, Thailand

[*]Address all correspondence to Chawalit Kittichaikarn E-mail: fengclk@ku.ac.th

The flocking process is an important process in latex glove industry and has complicated the two-phase flow phenomenon. At present, waste from this process is about 35%. This paper presents a numerical study of flock particle flow inside the flock cabinet using commercial software of Computational Fluid Dynamics (CFD). Thirteen flocking process models were simulated. Flow inside a flock cabinet was modeled in the three-dimensional domain. The standard k–ε model with standard wall functions was solved for the continuous phase while the discrete phase was modeled based on the Lagrange approach and stochastic tracking with Discrete Random Walk (DRW). Volume fraction of flock was set to be less than 10% and the effect of particle interaction on the particle trajectory was neglected. The drag and gravity forces were accounted in the equation of motion for particles. The experiment was performed to validate the simulation results. In the experiment, a flock cabinet was built from 8-mm-thick, 1074.5-mm-wide, and 833.5-mm-long Perspex sheet with a height of 1180 mm. The inlet hydraulic diameter was 0.5081 m. The uniform flock with an equivalence diameter of 50 μm was injected into the cabinet at the rate of 0.01 kg/s. Velocity, pressure, trajectory, and accretion of flock particles were measured. From the results obtained, it was found that the experimental results agreed well with those from simulation. The implement of a numerical method found that the damper position and angle adjustment can therefore be used to improve the efficiency of the flocking process. Installing the damper at –40^o and placing it at bottom positions have increased flock particle accretion on the glove surface by 15%. Besides, it can reduce flock waste up to 29% of the present process.

KEY WORDS: *flock, flocking process, latex glove, CFD, multiphase flow, accretion*

1. INTRODUCTION

Flocking process is one of the most important processes in latex industry. This process is used to add the wearing comfort and perspiration absorption to the surface of the glove. During this process, flock, which is monofilament fiber — usually nylon, rayon or cotton, is injected directly to the latex gloves to coat with adhesive within the flock cabinet. It has been known that the amount of monofilament fiber on the surface of the glove depends on the flow characteristics inside the flock cabinet that affects the distribution of the flock. Since the flow in the

1065-3090/10/$35.00

NOMENCLATURE

b_1, b_2, b_3, b_4	coefficients	V_i	velocity component, m/s
C_D	drag coefficient	V_{avg}	average inlet velocity, m/s
C_μ, $C_{1\varepsilon}$, $C_{2\varepsilon}$	constants	x_i	coordinate in x, y, or z direction
d_P	particle diameter, m	**Greek symbols**	
d	drag force coefficient, 1/s	α_p	solid volume fraction in a gas–solid two-phase flow
g_i	gravity component, m/s^2	δ	air relative density
G_k	generation of turbulence kinetic energy	δ_{ij}	Kronecker delta
m_P	particle mass, kg		turbulent kinetic energy
P	static pressure, Pa	ε	dissipation rate
Re	Reynolds number	K	turbulent kinetic energy, m^2/s^2
t	time, s	μ	molecular viscosity, m^2/s
$\bar{u}_i$	mean air velocity components, m/s	μ_t	turbulent viscosity, m^2/s
u_i	instantaneous air velocity components, m/s	ρ_a	density of air, kg/m^3
u_i'	fluctuating air velocity components, m/s	ρ_p	density of particle, kg/m^3
u_{Pi}	particle velocity component, m/s	σ_k, σ_ε	turbulent Prandtl numbers
		ϕ	particle shape factor

flock cabinet is multiphase, it can be considered as dilute dispersed two-phase flow. According to Sommerfel (2000), for the dilute dispersed two-phase flow, the volume fraction was less than 0.001 and inter-particle spacing was less than 10. The dilute dispersed two-phase flow was used to study the flow phenomenon such as the study of corrosion in the main stop valve of a steam turbine (Mazur et al., 2004), the study of electrostatic powder coating process (Shah et al., 2005), and the study of the particle–wall adhesion in a horizontal flow by Heinl and Bohnet (2005). This paper presents numerical and experimental analysis of flow inside the complex flock cabinet. A dilute dispersed gas–solid two-phase flow model was adopted. Air was considered as a continuous phase and flock was considered as a dispersed phase. The Lagrange approach and stochastic tracking with Discrete Random Walk (DRW) were used for the discrete phase. First, the computational fluid dynamics software was validated with the experimental results (S20T model). Then it was used to study thirteen flocking process models which have different damper angles and positions. The best flocking process model was validated again with those obtained by the experimental method.

2. EXPERIMENTAL DETAILS

The experimental facility was shown in Fig. 1. The purpose-built flocking cabinet was made from a 8-mm-thick Perspex sheet and three glove patterns were installed inside. Dampers were placed along inner sides of the cabinet to control flow direction. These dampers can be adjusted to vary damper angles and positions. The inlet hydraulic diameter of the cabinet was 0.5081 m. An axial fan was used to deliver air to the cabinet with an average velocity of 4.5 m/s (Re = 150,000). This air speed was adjusted by using a variable speed control unit. A pneumatic flock feeder injected 0.01 kg/s of flock particles to a cabinet. A standard CCD camera was placed perpendicular to the cabinet to capture the flock trajectory image with a light source from two fluorescents. Velocity and pressure distributions at various points (A–H) were measured by an anemometer and a micromanometer, respectively, for the case S20T where the damper was placed at the top of the cabinet and at a damper angle of 20^{o}. The measured data were used to validate the results obtained from the CFD program.

3. COMPUTATIONAL DETAILS

Figure 2 shows the computational domain of flow inside the flock cabinet. This cabinet consists of a flow inlet, a flow return, and two exhausts. Sixteen gloves arranged in two rows on a glove pattern were fed to the cabinet and were positioned exactly at the center of the flow inlet. Only half of the cabinet was simu-

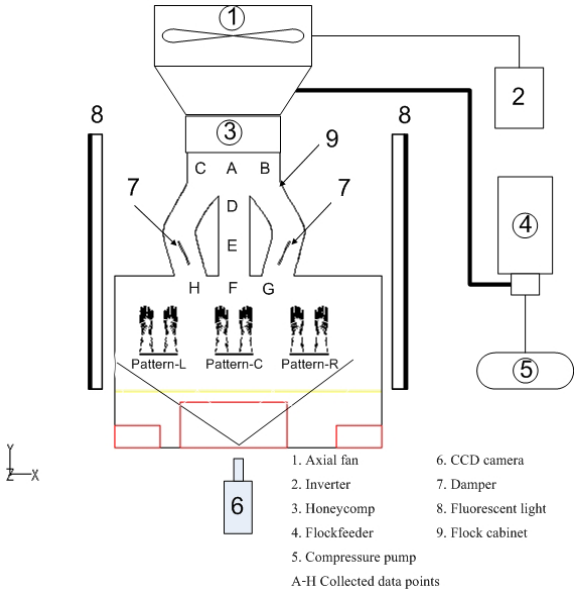

FIG. 1: Flock cabinet experimental setup

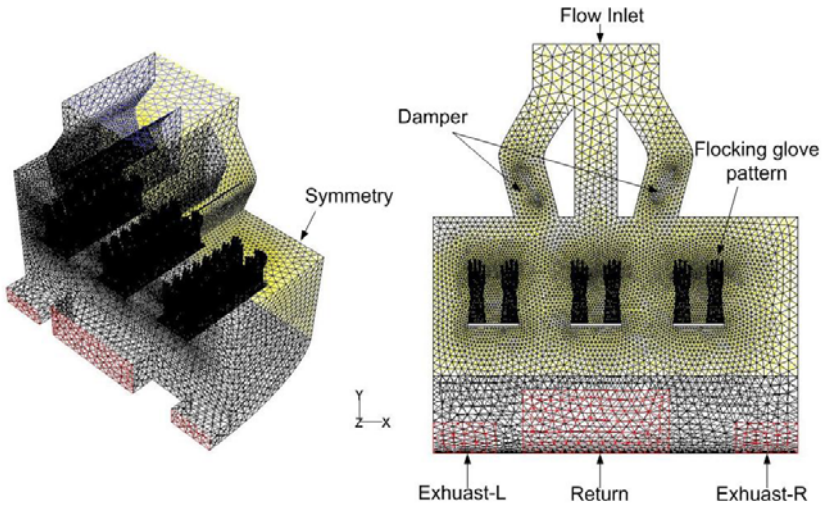

FIG. 2: Flow inside the flock cabinet domain

lated due to its symmetry to reduce the computational system requirement. The 50-μm flock sizes were released from the flow inlet at the flow rate of 0.005 kg/s and the flow Reynolds number was kept constant for each case at 150,000.

The flow inside the flock cabinet was simulated as a steady-state three-dimensional turbulent dilute gas–solid two-phase flow. Air was considered as the continuous phase and flock was the dispersed phase. Simulations were carried out using the commercial software. The domain was discretized in unstructured tetrahedral elements. The governing equations were solved using the second-order upwind scheme. SIMPLE algorithm was used for pressure–velocity coupling. The Navier–Stokes equation with the standard k–ε turbulent model was used to solve the continuous phase. Air was considered as incompressible, steady, and turbulent. The particle volume fraction was set to be less than 0.001%. The discrete phase was simulated using the Lagrangian method in addition to solving the transport equations for the continuous phase. The particle–particle interactions were neglected. The trajectories of the flock particles were predicted by integrating the force balance on the particles that was written in a Lagrangian reference frame. Details of the governing equations and solid-phase modeling for the gas phase and solid phase are given in Eqs. (1)–(12). The boundary conditions are listed in Table 1.

The governing equations used in the simulation are:

Mass conservation equation

$$\frac{\partial \overline{u_{ai}}}{\partial x_i} = 0 \tag{1}$$

TABLE 1: Boundary conditions used in this study

Boundary	Continuous phase	Discrete phase
Flow inlet	Velocity inlet with UDF	Velocity inlet with UDF 0.005 kg/s of flock injection
Return and 2 exhausts	Outlet pressure 0 Pa	Outlet pressure 0 Pa and set escape for the zone
Symmetry plane	Symmetry	Symmetry
Glove pattern	Wall	Wall and set trap for the zone
Other	Wall	Wall and set reflect for the zone

Momentum conservation equations

$$\frac{\partial}{\partial x_j}\left(\rho_a \overline{u_{ai}u_{aj}}\right) = -\frac{\partial p}{\partial x_i} + \frac{\partial}{\partial x_j}\left[\mu\left(\frac{\partial \overline{u_{ai}}}{\partial x_j} + \frac{\partial \overline{u_{aj}}}{\partial x_i}\right)\right]$$

$$+\frac{\partial}{\partial x_j}(-\rho_a \overline{u'_{ai}u'_{aj}}) + \rho_a g_i \tag{2}$$

$$+\rho_a F_D(u_{pi} - u_{ai})$$

k–ε turbulence model

$$\rho_a \bar{u}_{ai}\frac{\partial k}{\partial x_i} = \frac{\partial}{\partial x_i}\left[\left(\mu + \frac{\mu_t}{\sigma_k}\right)\frac{\partial k}{\partial x_i}\right] + G_k - \rho_a \varepsilon, \tag{3}$$

$$\rho_a \bar{u}_{ai}\frac{\partial \varepsilon}{\partial x_i} = \frac{\partial}{\partial x_i}\left[\left(\mu + \frac{\mu_t}{\sigma_\varepsilon}\right)\frac{\partial \varepsilon}{\partial x_i}\right] + C_{1\varepsilon}\frac{\varepsilon}{k}G_k, \tag{4}$$

$$-C_{2\varepsilon}\rho_a \frac{\varepsilon^2}{k}$$

Boussinesq hypothesis

$$-\rho_a \overline{u'_{ai}u'_{aj}} = \mu_t\left(\frac{\partial \bar{u}_{ai}}{\partial x_j} - \frac{\partial \bar{u}_{aj}}{\partial x_i}\right) - \frac{2}{3}(\rho_a k)\delta_{ij} \tag{5}$$

Turbulence viscosity

$$\mu_t = \rho_a C_\mu \frac{k^2}{\varepsilon} \tag{6}$$

Generation turbulent kinetic energy

$$G_k = -\rho_a \overline{u'_{ai} u'_{aj}} \frac{\partial u_{aj}}{\partial x_i} \tag{7}$$

Turbulent constants

$$C_\mu = 0.09, \quad C_{1\varepsilon} = 1.44, \quad C_{2\varepsilon} = 1.92$$

Turbulent Prandtl numbers

$$\sigma_k = 1, \quad \sigma_\varepsilon = 1.3$$

Trajectory prediction equations:

Force balance on the particle

$$\frac{\partial u_{pi}}{\partial t} = F_D (u_{ai} - u_{pi}) + g_i(\rho_p - \rho_a)/\rho_a \tag{8}$$

Particle velocity

$$\frac{\partial x_i}{\partial t} = u_{pi} \tag{9}$$

Other relations are:

Drag force due to interaction between the solid and gas phases

$$F_D = \frac{18\mu}{\rho_p d_p^2} \frac{C_D \mathrm{Re}}{24} \tag{10}$$

Reynolds number

$$\mathrm{Re} = \frac{\rho_a d_p |u_{pi} - u_{ai}|}{\mu} \tag{11}$$

Drag coefficient

$$C_D = \frac{24}{\mathrm{Re}} (1 + b_1 \mathrm{Re}^{b_2}) + \frac{b_3 \mathrm{Re}}{b_4 + \mathrm{Re}}, \tag{12}$$

where

$$b_1 = \exp\left(2.3288 - 6.4581\phi + 2.4486\phi^2\right),$$

$$b_2 = 0.0964 + 0.5565\phi, \qquad b_3 = \exp\left(4.905 - 13.8944\phi - 18.4222\phi^2 - 10.2599\phi^3\right),$$

$$b_4 = \exp\left(1.4681 + 12.2584\phi - 20.7322\phi^2 + 15.8855\phi^3\right).$$

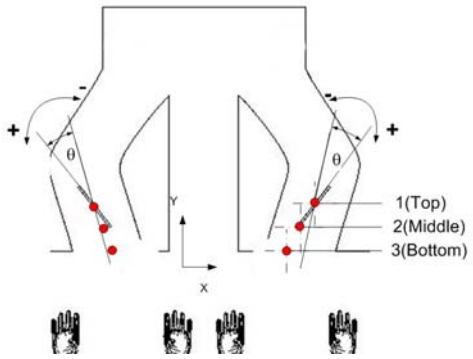

FIG. 3: Angle and position of damper installation

Thirteen flocking process models were studied. Angle and position of the damper were adjusted in the direction as shown in Fig. 3.

4. RESULTS AND DISCUSSION

4.1 Velocity, Pressure and Particle Trajectory of Flow inside the Cabinet

Figures 4 and 5 show numerical and experimental comparison of Y-velocity and static pressure of flow inside the cabinet. It was found from these figures that the numerical method used in this study has a well predicable Y-velocity and static pressure of air flow (continuous phase) in the cabinet. It was also found from the results that the flow is mostly uniform. The flock particle (discrete phase) trajectory was shown in Fig. 6. It can be seen from the results obtained that the air stream in the central channel of the cabinet deviate the flow paths of the left and right air steams. This results in low accretion of flock on the glove surface. The results were similar to those obtained from flow visualization of the flock trajectory in the experiment as shown in Fig. 6b

4.2 Flock Accretion on a Glove Surface

The attachment of flock on the surface was revealed as flock accretion (unit is in $kg/m^2 \cdot s$). Figures 7 and 8 show the accretion of flock on top and side views of the glove surface obtained from simulation and experiment. With the aid of the image processing program, it was found from these figures that the flock accretions on the top view projection area of the glove surface were about 49% and 35% obtained from simulation and experiment, respectively. On the side view projection area of the glove surface, the flock accretions were about 17% and 20% obtained from simulation and experiment respectively. Low accretion of flock on the side of the glove surface was due to the effect of a strong flow in the central channel as mentioned previously.

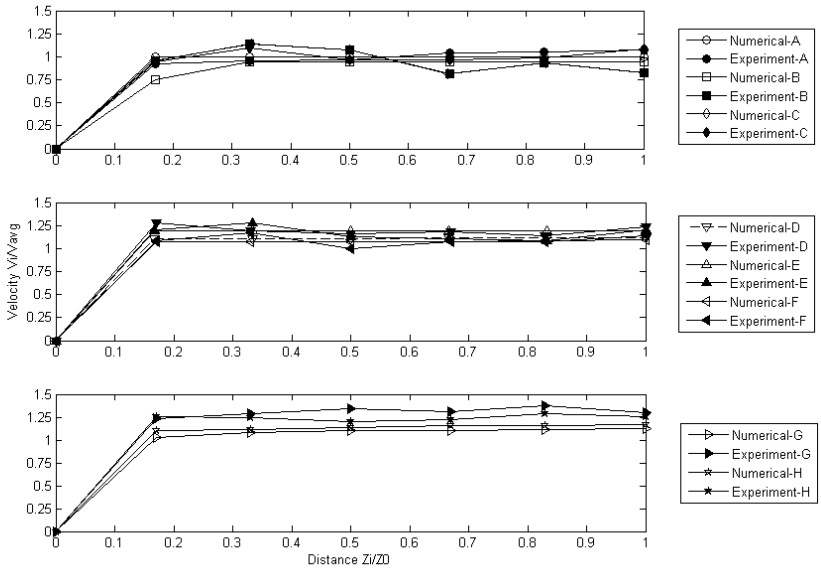

FIG. 4: Numerical and experimental Y-velocity of the S20T model

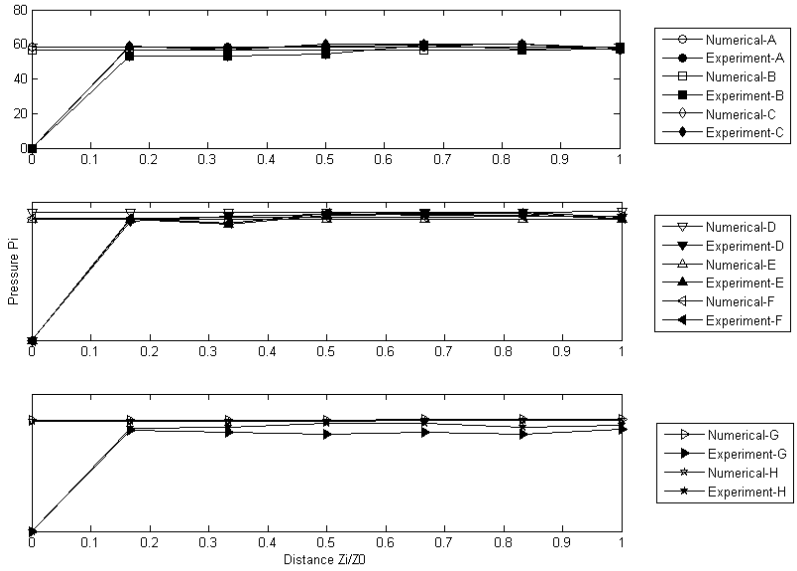

FIG. 5: Numerical and experimental pressure of the S20T model

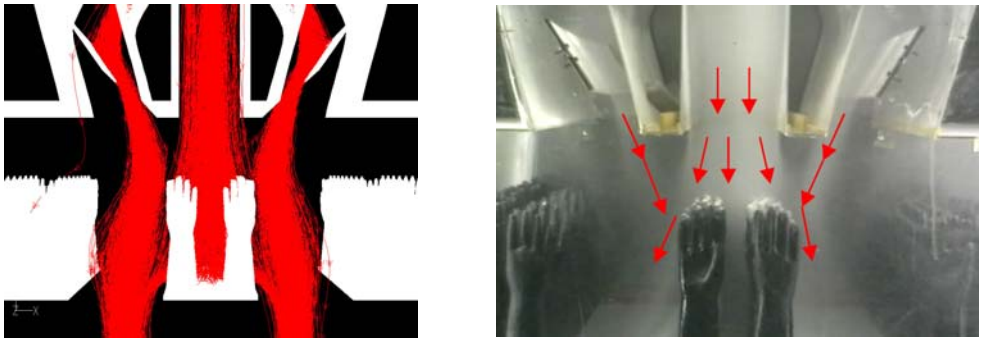

(a) (b)

FIG. 6: Numerical and experimental flock trajectory on the front-view flock cabinet of the S20T model: (a) numerical results and (b) exerimental results

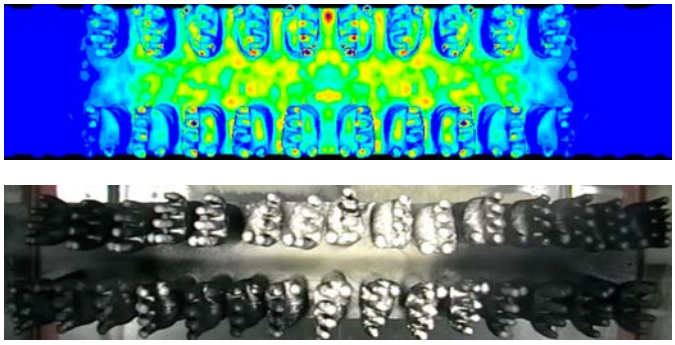

(a)

(b)

FIG. 7: Numerical and experimental flock accretion on the top-view glove surface of the S20T model: (a) numerical results and (b) exerimental results

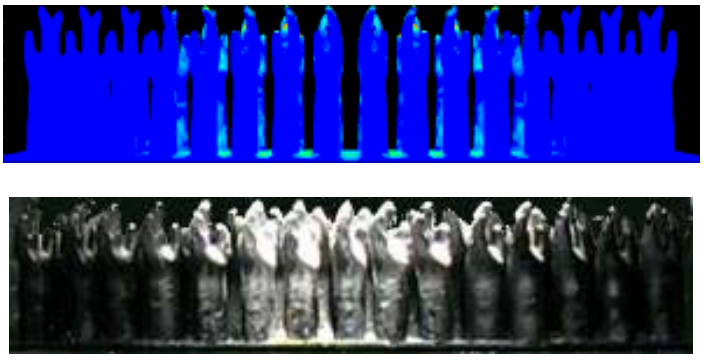

(a)

(b)

FIG. 8: Numerical and experimental flock accretion on the side-view glove surface of the S20T model: (a) numerical results and (b) exerimental results

4.3 Improvement in the Flocking Process

From a numerical result shown in Table 2 and the experimental results of the SM40B model shown in Figs. 9–12 it was found that the flock accretion was affected by the damper angle and position. Therefore, changing the damper angle to direct the flock particle to the Pattern-L and Pattern-R of the gloves can reduce the effect of the central channel flow stream. This adjustment enhanced the flock accretion, especially for the SM40B model, to 15% and reduced flock waste at about 29% compared to the present flock cabinet setting model (S20T).

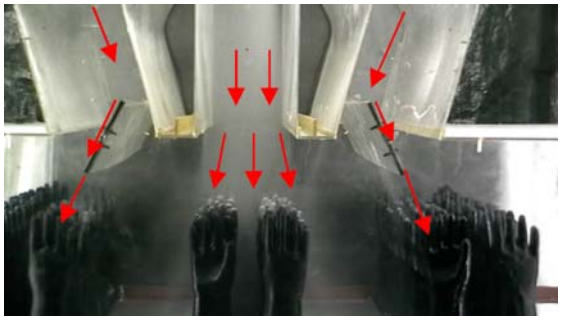

FIG. 9: Experimental flock trajectory on the front-view flock cabinet of the SM40B model

TABLE 2: Numerical flock accretion on the glove surface

Flock cabinet model	Accretion (×E-03 kg/s)			Flock (×E-03 kg/s)	
	Pattern-L	Pattern-C	Pattern-R	Waste	Reuse
SM40B	1.46	3.25	1.09	2.01	2.19
SM30B	1.14	2.71	0.913	1.59	3.65
SM20B	0.513	2.39	0.401	1.96	4.74
SM20	0.058	2.69	0.062	2.64	4.14
S30T	0.028	2.94	0.044	2.39	4.59
S30M	0.0567	3.02	0.0593	2.27	4.59
S30B	0.1121	3.15	0.17	2.18	4.38
S20T	0.026	2.75	0.0407	2.06	5.12
S20M	0.103	2.27	0.117	1.56	4.19
S20B	0.266	2.86	0.273	2.20	4.40
S10T	0.072	2.50	0.0733	2.29	5.06
S10M	0.251	2.54	0.233	2.15	4.83
S10B	0.542	2.42	0.455	0.841	5.74

Note: The flock cabinet model can describe with XX YY Z: X — system; X — sign of damper angle (M — negative and no letter — positive), YY — damper angle, Z — damper installed position.

FIG. 10: Experimental flock accretion on the Pattern-C glove surface of the SM40B model (a) top-view and (b) side-view

FIG. 11: Experimental flock accretion on the Pattern-L glove surface of the SM40B model: (a) top-view and (b) side-view

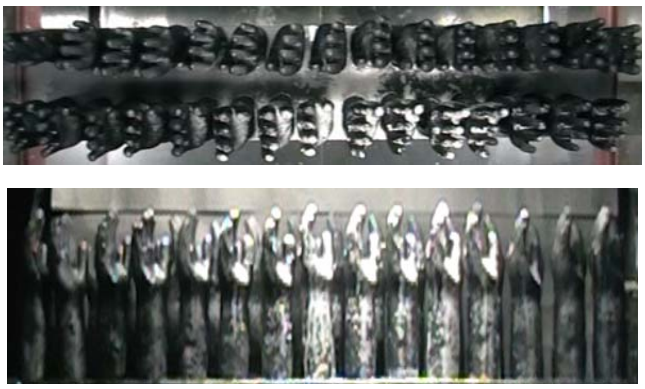

FIG. 12: Experimental flock accretion on the Pattern-R glove surface of the SM40B model: (a) top-view and (b) side-view

5. CONCLUSIONS

In this study, the computational method was used to predict the phenomenon of a two-phase flow inside the flock cabinet with an error less than 15%. It was also found that the damper angle is a key factor that affects the flock accretion on the glove surface. Among the thirteen flock cabinet models, the SM40B model has a highest flock accretion on the glove surface (Pattern-L = 1.46E-03 kg/s, Pattern-R = 1.09E-03 kg/s, and Pattern-C = 3.25E-03 kg/s). Besides, it reduced flock waste up to 29% of the present process.

ACKNOWLEDGMENTS

This research work is financially supported by the Thailand Research Fund-Master Research Glants (TRF-MAG). The authors would like to thank Mr. Rittinarong Juntarasook for the very helpful discussion throughout the research work.

REFERENCES

Heinl, E. and Bohnet, M., Calculation of particle-wall adhesion in horizontal gas-solids flow using CFD, *Powder Technol.*, vol. 159, pp. 95–104, 2005.

Mazur, Z., Campos-Amezcua, R., Urquiza-Beltran, G., and Garcia-Gutierrez, A., Numerical 3D simulation of the erosion due to solid particle impact in the main stop valve of a steam turbine, *Appl. Thermal Eng.*, vol. 24, pp. 1877–1891, 2004.

Shah, U., Zhu, J., Zhang, C., and Nother Senior, J. H., Numerical investigation of coarse powder and air flow in an electrostatic powder coating process, *Powder Technol.*, vol. 164, pp. 22–32, 2006.

Sommerfeld, M., Theoretical and Experimental Modelling of Particulate Flows, Lecture Series 2000-06, von Karman Institute for Fluid Dynamics, Germany, 2000.

Journal of Flow Visualization & Image Processing 17(4), 359–369 (2010)

ELEMENTAL STRUCTURE OF SPLASH GENERATED BY A PLUNGING SOLID BODY

Yoshihiro Kubota[1*] & Osamu Mochizuki[2]

[1]*Graduate School of Engineering, Toyo University, 2100 Kujirai, Kawagoe, Saitama 350-8585, Japan*

[2]*Faculty of Science and Engineering, Toyo University, 2100 Kujirai, Kawagoe, Saitama 350-8585, Japan*

[*]Address all correspondence to Yoshihiro Kubota
E-mail: dn0800032@toyonet.toyo.ac.jp

The objective of this study is to understand effects of the shape of a plunging body on splash. The splash was formed in the following steps: the primary (film type), secondary (mushroom type), and tertiary (rebound type) splashes. The primary splash as a first step influences the following process. Thus, we changed experience of the primary splash by changing the body shape to investigate its effects on formation of the splash. A hemisphere was common in the head of the bodies but tails had the following three shapes: a hemisphere, cone, and cylinder. We selected these shapes in order to make them have different connecting longitudinal lines at the joint between the hemisphere head and tail. Thus, the line affected the development of the primary splash as a film flow (primary splash) along the wall. The film flow covered the hemisphere head at first and moved to different ways related to the tail shape of the tested body. The detachment or adherence of the film flow affected the formation of the secondary splash. We observed a mushroom type splash in the case of the sphere (hemisphere head connecting a hemisphere tail), mushroom on an air-dome (bubble on the water surface) in the cases of the bodies with cylinder and cone tails. We discussed these different secondary splashes related to the primary splash in this paper.

KEY WORDS: *water splash, solid body, flow visualization, film flow, high-speed movie*

1. INTRODUCTION

We investigated the primary and secondary splashes in the developing process of the whole splash caused by impingement of a body on the water surface. The primary splash is generated by impingement of the head of the body at first, which is a thin film flow along the wall of the body. Small droplets were observed at the tip of the film. This is a similar phenomenon to a milk crown due to a milk-droplet falling into milk. The number of the droplets is equal to that of the fingers. The number of the droplets can be predicted according to the Weber number.

Yoon et al. (2007) investigated finger-like structures appearing at the circumferential edge of water film flow that is spreading in the radial direction after a droplet impacting on a solid surface. Vander Wal et al. (2006) reported the splash formation by a droplet impact on a dry or rough or wet solid surface. They also considered the characteristics of a droplet. Cossali et al. (1997) reported the impact of a single droplet on a thin liquid film. They studied the influence of the film thickness and liquid viscosity on the splash. The splash formation was also studied by Worthington (1882). Worthington (1882) investigated a milk crown by making a milk droplet or solid body collide on milk. They showed splash patterns, but the details were not shown. Duez et al. (2007) studied relationships between water splash and its sound. Since the sound is related to oscillation of entrained bubbles, the splash formation is important to study for its sound generation.

In spite of familiar phenomenon in our real life, details of splash have not been known yet because many parameters govern formation of the splash. We showed three types of splash patterns by impact velocity of a body (Kubota and Mochizuki, 2009): (I) spire-type splash, (II) mushroom-type splash, and (III) crown-type splash. The splashes of types (II) and (III) are related to the film flow as the primary splash. The objective of this study is to investigate the effect of the primary splash as a film flow along the wall of the body on formation of the secondary splash. We observed splash-formation processes by using a high-speed CMOS camera during the body plunging into water. A thin film flow (primary splash) with droplets was formed when the head of the body plunged to the water surface. A mushroom-type splash (secondary splash) was formed when the film flow closed behind the body entering into water. Since the body shape influences the appearance of these splashes, we investigated formation processes of splash by three different solid bodies. A hemisphere was common in the head of the bodies but tails were of the following three shapes: a hemisphere, cone, and cylinder. We selected these shapes in order to make them have different connecting longitudinal lines at the joint between the hemisphere head and tail. Thus, the line affected the development of the primary splash as a film flow along the wall. The film flow (primary splash) covered the hemisphere head at first and moved to different ways related to the tail shape of the tested body. The detachment or adherence of the film flow affected the formation of the secondary splash. Thus, the shape of the tail affected the formation of the secondary splash. We observed a mushroom-type splash in the case of the sphere (hemisphere head connecting hemisphere tail), mushroom on an air-dome (bubble on the water surface) in the cases of the bodies with cylinder and cone tails. We discussed the formation mechanism of these different shapes of the secondary splash according to high-speed movies in this paper.

2. EXPERIMENTAL SETUP

We observed splash generated by a body plunging into water using a high-speed CMOS camera (Vision Research Inc., Phantom v7.1). A water tank with a size of

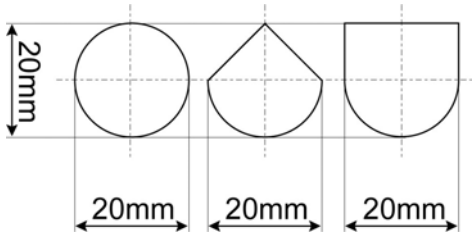

FIG. 1: Sketch in the side view of bodies plunging into water

$300 \times 300 \times 400$ mm^3 was used, and tap water was filled up to 340 mm. Experimental results were free from contaminant of tap water (Kubota and Mochizuki, 2009). Consecutive images of splash formation were taken from the side of the water tank. The frame rate of the camera was set at 4000 frames per second. This means that the precision timing of each frame is 0.25 ms. A halogen lamp of 500 W was used for volume illuminating the splash.

Plunging bodies were made of acrylic resin. The diameter, D (= $2r$), of the projection area of the bodies is 20 mm, and height (length in the moving direction) is also 20 mm as shown in Fig. 1. We tested three different shapes. The head of the bodies is a hemisphere, but the tail is different for each: a) hemisphere as a sphere-tail body, b) cone as a cone-tail body, and c) circular cylinder as a cylinder-tail body. To maintain surface conditions before each trial, we cleaned the surface of the bodies carefully for stains such as oil. Changing the initial height, h, which is measured from the water surface to the bottom of the body, varied the impact velocity, V_i, of the body at the water surface. The initial height h was varied from $5D$ to $50D$ so that the range of V_i was from 1.2 to 4.4 m/s. V_i was calculated by $V_i = (2gh)^{0.5}$ from the energy conservation law. The air drag was neglected in this calculation because h is small. A launcher system held the body via suction at the initial height just before release. The bodies fall without rotation or horizontal displacement so that impacting events are repeatable.

3. EXPERIMENTAL RESULTS

Figure 2 shows a tree diagram of elemental structures seen in the sequential event of splash formation due to body impingment. The primary splash is originated from the reaction of the body head impingement. Thus, this appears first as a thin film flow along the head. Its shape and behavior are similar to a milk crown or a droplet spreading on a flat plate. Tiny droplets were separated from an edge of the thin film. A number of the droplets coincides with that of fingers of a thin film flow. The droplets fly initially in the tangential direction at its detached position. It is easy to imagine that an impinging velocity, a shape, and wall conditions of the body influence the primary splash. The secondary splash is a result of impingement of the primary splash. Therefore, if the primary splash does not close behind the

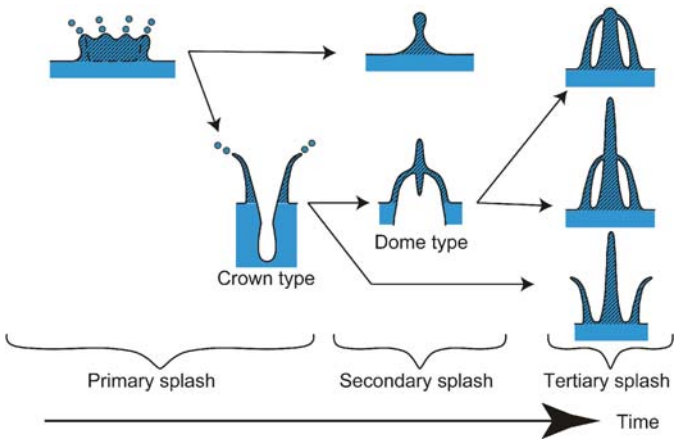

FIG. 2: Tree diagram of elemental structures seen in the process of splash formation

body, it never appears. We have observed the mushroom-like splash as the secondary splash in the case of the sphere body (Kubota and Mochizuki, 2009). The thin film flow as the primary splash along the wall of the sphere closed at the rear top, so that the secondary splash was formed. If the thin film flow closes at a position far from the rear part of the body, it forms a dome of water film, that is, a large bubble on the water surface. The secondary splash appears at the top of the dome. Thus, the tail shape affects not only motion of the primary splash but also the secondary splash. We are interested to know how the tail shape of the body affects formation of the secondary splash.

Two important nondimensional parameters related to splash formation are the Reynolds number Re and the Weber number We. The former is defined as $\mathrm{Re} = V_i D/\nu$, where ν is the kinematic viscosity of water at 25°C in this experiment, and the latter is given by $\mathrm{We} = \rho V_i^2 D/\sigma$, where ρ is the density and σ is the surface tension of water at 25°C. The dimensionless time T is defined as $T = tV_i/D$, where t is the actual time measured from the beginning of impingement. Therefore, $T = 0$ means the time when the head of the body touches the water surface. Even if V_i is different, $T = 1$ indicates the same dimensionless time interval when the body moves a distance equal to the distance D.

3.1 Primary Splash

The primary splash of the plunging body with different shapes of the tail is shown in Fig. 3. The experimental conditions of these results are $V_i = 4.4$ m/s, $\mathrm{We} = 5.4 \times 10^3$, and $\mathrm{Re} = 1.0 \times 10^5$. The photo shows the figure of the primary splash taken at $T = 0.5$ when half of the body was immersed in water. Since the head is the same as a sphere even if the tail is different, the effect of the head on growth of the primary splash is the same until the film flow reached $D/2$. However, the velocity of the film flow along the head is slightly faster than the speed of the

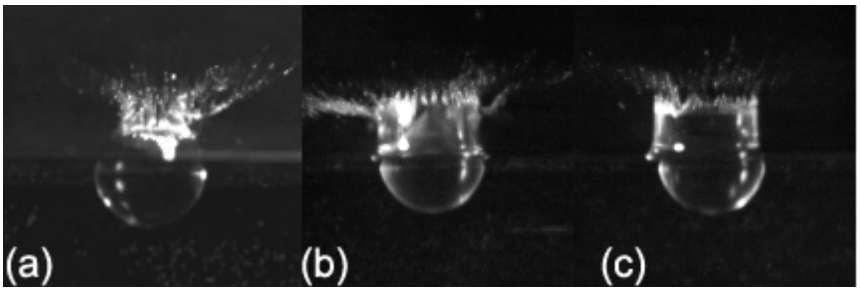

FIG. 3: Primary splash at $T = 0.5$ in the case of $V_i = 4.4$ m/s: (a) sphere, (b) cone tail, and (c) cylinder tail

body. Therefore, the primary splash, namely, film flow, is already affected by the tail at the time. In the case of the sphere seen in Fig. 3a, the film flow rises along the tail. In the case of the cone-tail bodies seen in Fig. 3b, the film flow goes upward. Since the longitudinal line of the tail inclines toward the center, the film flow separates from the tail. Therefore, the film flow forms a pipe like a tumbler. This is different from other cases. In the case of the cylinder-tail body seen in Fig. 3c, the film flow rises along the tail.

Tiny droplets are also characteristics of the primary splash. Yoshida (1997) reported the Weber number on split of a droplet in two in airflow. He showed the critical We_c giving the condition of split. Applying the critical We number to the finger of the primary splash, We_c in our experiment is $We_c = 11.5D_d^{-0.209} = 2.6 \times 10^1$. Here, D_d is the thickness of the film flow. The finger is a familiar phenomenon appearing at the tip of the expanding puddle of a droplet colliding with a solid surface. We can see the fingers at the tip of the film flow as seen in Fig. 3. The Weber number for the film flow is $We_s = 1.2 \times 10^2$ in the cone-tail body and $We_s = 1.6 \times 10^2$ in the cylinder-tail body based on the thickness and speed of the film flow. Since these values exceed We_c, fingers appear properly.

Many tiny droplets separated from the top of the film flow spread out in the radial direction in the all three cases. This means that the droplets separate when the film flow moves along the head. The relation between positions of separation of the initial droplet from the film flow and impact velocity, V_i, is shown in Fig. 4. The position is represented by the distance along the wall measured from the front top of the sphere as seen in an illustration in Fig. 4. Circle symbols are the results in the case of the sphere, triangle ones stand for the cone-tail, and square ones for the cylinder-tail bodies. The distance at which separation occurs becomes smaller when the impact velocity increases. Since velocity of the film flow increases with increasing V_i (Kubota and Mochizuki, 2009), the Weber number of droplet-separation based on the velocity and length of the film flow exceeds the critical Weber number at a shorter length of the film flow. Therefore, the angle of the initial separation position of the droplets becomes small when V_i becomes faster. Since

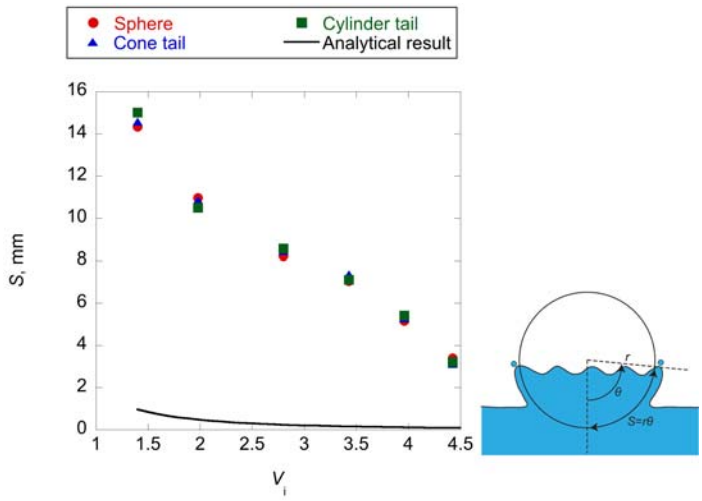

FIG. 4: Relation between the droplet generated position and impacr velocity. Solid line shows the value from the critical Weber number We_c

the distance is smaller than $\pi r/2 \sim 15.7$ mm in this study, the droplets are generated when the film flow moves on the head in the three cases. Thus, separation of the droplets is independent of the tail in this experiment. The head is hemisphere so that the centrifugal force becomes larger when V_i becomes faster. The centrifugal force will promote separation earlier too when the velocity of the film flow increases. Therefore, the head shape affects the primary splash directly.

3.2 Secondary Splash

The film flow closing at the rear end of the body causes the secondary splash. The secondary splash observed at $T = 2.0$ is shown in Fig. 5. The impact velocity, Re, and We are the same in three cases, respectively. The tail influences motion of the film flow passing through the connection between the head and tail. The film flow moves along the wall in the cases of the sphere. It moves along the wall until it reaches the end of the wall in the cylinder-tail body. On the other hand, it separates from the wall at singularity position of connection between the head and tail in the case of the cone-tail body. These different experiences affect later motion of the film flow. Those different manners of impingement of the film flow behind the body cause the difference of the secondary splash as described later.

The other interesting feature seen in Fig. 5 is an air cavity behind the submerging body. This was observed in the cases of the cone- and cylinder-tail bodies, whereas not in the case of a sphere. Reaction due to its detaching from the body causes the tertiary splash as shown in Fig. 2. The tertiary splash becomes higher when the air cavity is deeper if there is no dome. As seen in Fig. 5a, the air cavity does not appear if the film flow covers the body before the body submerges

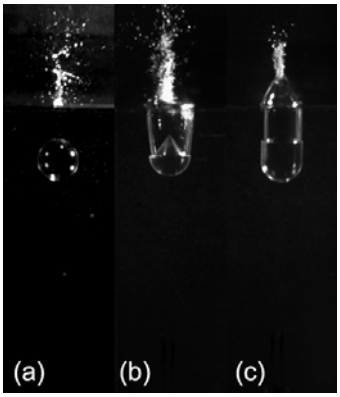

FIG. 5: Secondary splash at $T = 2$ in the case of $V_i = 4.4$ m/s: (a) sphere, (b) cone tail, and (c) cylinder tail

into water. Therefore, the relation between the film flow and tail of the body is important for the appearance of the air cavity. Change in direction of the front of the film flow is shown in Fig. 6. Definition of symbols is the same as that used in Fig. 4. The angle was measured from a vertical axis. Thus, when the film flow moves along the head, the angles show minus until $T < 0.3$. In contrast to this, the film flow turns toward the centerline of the body, namely its direction is inward. The one of the force acting inward is the surface tension to contract the surface area of a pipe of the film flow. The other one is the pressure difference between inside and outside (atmospheric pressure) the pipe. The inside pressure may be lower than the atmospheric pressure because it is low in the wake of a body. Thus,

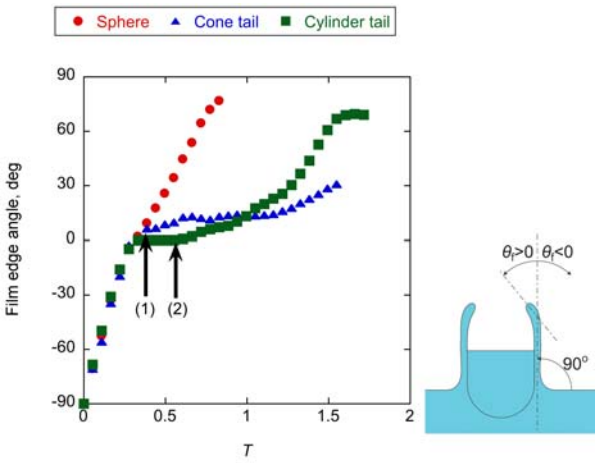

FIG. 6: Change in the derection of film flow in the case of $V_i = 4.4$ m/s. Timing of film separation is shown (1) by a cone tail and (2) by a cylinder tail models

the film flow turns inward by means of both the forces at when it separates from the connecting line in the case of the cone-tail body and from the rear edge of cylinder in the case of the cylinder-tail body. From the comparison of the angle at when the film flow separates close time, the angle increases as the same tendency in the short intervals just after the separation. This is because the initial direction and velocity of the film flow, and curvature of a separation line at separation are the same.

Since the influence of the surface tension on shrinkage of the pipe is the same for both cases, the difference of the change between the cases of cone- and cylinder-tail bodies is a cause of the pressure difference. As the time rate of the change in angle in the case of the cylinder-tail is larger than that in the case of the cone-tail body, the pressure in the wake of the cylinder-tail body may be lower than that of the cone-tail body.

The last point of the data in Fig. 5 shows the one at when the film flow closes behind the body.

The closing time in the case of the sphere is the earliest. Since the film flow moves along the sphere, the traveling distance is the shortest compared with other cases. Moreover, the velocity of the film flow along the sphere becomes slow when it moves along the tail, and yet it is faster than that of the other cases. The film flow on the sphere closes on the tail before the sphere sinks completely. Therefore, there is no air cavity in the case of the sphere. On the other hand, the closing time in the case of the cylinder-tail body is the latest because of the longest traveling distance.

The secondary splash generated by the cylinder-tail body at T = 1.9 and 4.0 is shown in Fig. 7. We can see jets branched upward and downward at the impinging position of the film flow as seen in Fig. 7a. The upward jet is called the secondary splash in this paper. The downward jet appears when the film flow forms a dome. Thus, it does not appear in the case of the sphere because of no formation

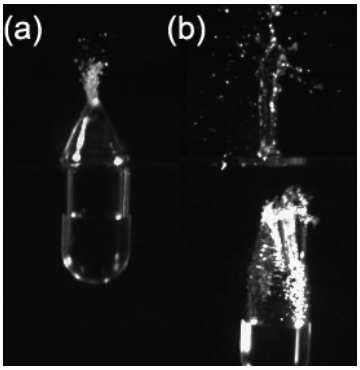

FIG. 7: Collision of film flow and downward jet a trigger of ripples on air-cavity in the case of cylinder-tail body impingment at V_i = 4.4 m/s

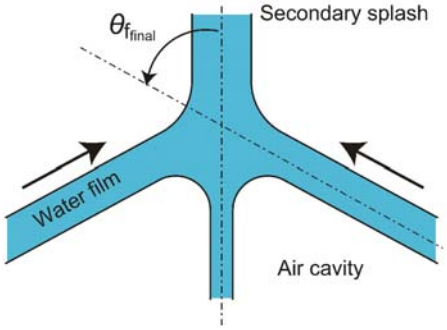

FIG. 8: Schematic diagram of collision of film flow

of the dome. Ripples on the surface of the air cavity are recognized when the downward jet hit the surface as seen in Fig. 7b. A sketch of impingement of the film flow is shown in Fig. 8. The separated film flow collides at an angle shown in Fig. 6. A collision angle of the film is presented by θ_f. According to the momentum theory, the flow rate can be estimated as $Q_u/Q_f = (1 + \cos \theta_f)/2$ and $Q_d/Q_f = (1 - \cos \theta_f)/2$, where Q_u is the flow rate of the upward jet, Q_d the downward jet, and Q_f is a total flow rate of the film flow. Flow rate in our experiment is $Q_u/Qf = 0.67$, $Q_d/Q_f = 0.33$ for a cylinder tail and $Q_u/Q_f = 0.93$, $Q_d/Q_f = 0.07$ for a cone tail. This estimation indicates that the flow rate of the secondary splash in the case of the cone-tail body is larger than that of the cylinder-tail body. Thus, the height of the secondary splash of the cone-tail body is higher than that of the cylinder-tail body. The collision angle of the film flow determines the height of the secondary splash. As mentioned previously, the collision angle depends on the wake of the body. Therefore, the connection line between the head and tail affect the secondary splash.

To confirm the fact, we tested an experiment on the splash formation for a smoothly connected body like as a teardrop. The result is shown in Fig. 9. The ge-

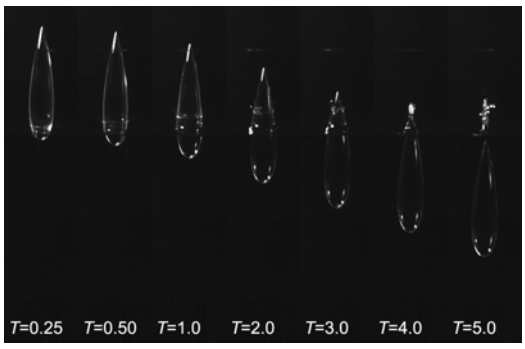

FIG. 9: Sequence of splashes by the teardrop body in the case of V_i = 4.4 m/s

ometry of the body is 20 mm in width and 95 mm in height, and the projection geometries are a circle in the top view and NACA0021 in the side view. Impact velocity, We number, and Re number are the same as those shown in Figs. 3, 5, and 7. The film flow as the primary splash was observed in the whole time in the plunging process of the body as seen in Fig. 9. Tiny droplets were produced from the tip of film during the film flow rising along the wall. The interesting thing is that height of the film flow seems not to be changed after $T = 2$. Potential energy and kinematic energy of the film flow may be balanced at the height. Finally, the film flow never separates in this case, and closes at the rear end of the body at $T = 4.0$. The dome and air cavity did not appear. The collision angle and flow rate of the film flow are small so that the secondary splash is small. It indicates that the splash can be controlled by the body shape.

4. CONCLUDING REMARKS

We observed the process of splash generation by an impact of a solid body on the water surface. Several types of splashes arise according to impact conditions related to impact velocity, behavior of film flow, and shape and surface conditions of the body. We focused on how a tail shape affects splash formation in this paper. We tested bodies of a hemisphere as head with three types of the tail shape: a hemisphere, cone-tail, and cylinder-tail bodies. Two elemental structures of splash were investigated: the primary splash and the secondary splash. We found that these are deeply associated with adhesive characteristics of the film flow on the wall of the body and with impingement of the separated film flows. The film flow as the primary splash produces tiny droplets from its front, which is related to the finger phenomena. Thus, the Weber number is the indicator for estimating droplets formation. The secondary splash is caused by the film flow collision behind the body. The body geometry affects adhesion and detachment of the film flow. The film flow detached at a position where the curvature changed suddenly, that is, a singular point. The detachment causes a delay of the film flow collision, and an air cavity formation. Ripples observed on the air cavity surface are caused by the downward jet produced by the inclined collision of the film flow. Streamlined body like as a teardrop shape does not form the air cavity, and the secondary splash is small.

REFERENCES

Cossali, G. E., Coghe, A., and Marengo, M., The impact of a single drop on a wetted solid surface, *Exp. Fluid*, vol. 22, pp. 463–472, 1997.

Duez, C. Y., Clanet, C., and Bocquet, L., Making a splash with water repellency, *Nature Phys*., vol. 3, pp. 180–183, 2007.

Kubota, Y. and Mochizuki, O., Splash formation by a spherical body plunging into water, *J. Visualization*, vol. 12, no. 4, pp. 339–345, 2009.

Vander Wal, R. L., Berger, G. M., and Mozes, S. D., The combined influence of a rough surface and thin fluid film upon the splashing threshold and splash dynamics of a droplet impacting onto them, *Exp. Fluid*, vol. 40, pp. 23–32, 2006.

Worthington, A. M., On impact with a liquid surface, *Proc. Roy. Soc. London*, vol. 34, pp. 217–230, 1882–1883.

Yoon, S. S., Jepsen, R. A., Nissen, M. R., and O'Hern, T. J., Experimental investigation on splashing and nonlinear fingerlike instability of large water drops, *J. Fluids Struct*., vol. 23, pp. 101–115, 2007.

Yoshida, T., Critical breakup of a liquid droplet due to airstreams, *Trans. JSME B*, vol. 63, pp. 3580–3587, 1997.

TABLE OF CONTENTS

JOURNAL OF FLOW VISUALIZATION & IMAGE PROCESSING

VOLUME 17

ISSUE 1

ISSUE 2

ISSUE 3

ISSUE 4

JOURNAL OF FLOW VISUALIZATION & IMAGE PROCESSING

VOLUME 17

JOURNAL OF FLOW VISUALIZATION & IMAGE PROCESSING

VOLUME 17